Dipl.-Ing. Christoph Birkl, BSc

# Post-mortem Assessment of Iron in Multiple Sclerosis Brain using Magnetic Resonance Imaging

## DOCTORAL THESIS

to achieve the university degree of

Doktor der technischen Wissenschaften

submitted to

## Graz University of Technology

Supervisor

Univ.-Prof. Dipl.-Ing. Dr.techn. Rudolf Stollberger

Institute of Medical Engineering
Graz University of Technology

Faculty of Computer Science and Biomedical Engineering

Graz, December 2015

## AFFIDAVIT

I declare that I have authored this thesis independently, that I have not used other than the declared sources/resources, and that I have explicitly indicated all material which has been quoted either literally or by content from the sources used. The text document uploaded to TUGRAZonline is identical to the present doctoral thesis.

_____          _____
            Date                                         Signature

This thesis was conducted at the

Institute of Medical Engineering
Graz University of Technology

under the supervision of
**Univ.-Prof. Dipl.-Ing. Dr.techn. Rudolf Stollberger**

in co-operation with the

Department of Neurology
Medical University of Graz

unter the co-supervision of
**Assoz.Prof. Univ.-Doz. Dipl.-Ing. Dr.techn. Stefan Ropele**

Assessor:
**Prof. Dr.rer.nat.med.habil. Jürgen R. Reichenbach**
Medical Physics Group
Department of Diagnostic and Interventional Radiology
University Hospital Jena, Germany

# Abstract

Iron plays an important role in the metabolism of the human brain. There is evidence that the iron metabolism is disturbed, and abnormal iron accumulation can occur in neurological diseases such as multiple sclerosis (MS). Magnetic resonance imaging (MRI) is a suitable tool to assess iron inside biological tissue. State of the art MRI techniques to quantify iron are restricted to gray matter, due to the confounding influence of diamagnetic contributions caused by myelin. Thus, there is need for a suitable technique to quantify iron independent of myelin. In this thesis, a novel MRI technique for iron mapping, independent of diamagnetic contributions, is presented. This technique is based on the temperature dependency of the paramagnetic susceptibility, described by Curie's law. Temperature dependent MRI was applied on post-mortem MS brain tissue. The captured iron maps based on the temperature coefficient of $R_2^*$ were in agreement with histopathological results and literature. In post-mortem MRI, temperature, tissue fixation and autolysis processes are affecting MRI image contrast and quantitative relaxation parameters. A detailed examination of the post-mortem effects in MRI was part of the thesis. This work showed for the first time quantitative iron maps of white and gray matter structures. In conclusion, this technique showed the suitability of temperature dependent MRI to reveal novel insights into the iron distribution in MS brain tissue.

# Key Words

magnetic susceptibility, iron, multiple sclerosis, temperature dependent MRI, post-mortem MRI, formalin fixation

# Kurzfassung

Eisen ist ein wichtiges Element im Stoffwechsel des menschlichen Gehirns. Es gibt Hinweise dass bei neurodegenerativen Erkrankungen wie beispielsweise Multipler Sklerose (MS) der Eisenhaushalt im Gehirn gestört ist und abnormale Eisenablagerungen auftreten können. Die Magnetresonanztomographie, kurz MRT, ist die wichtigste Bildgebende Technik um Eisenablagerungen im Gehirn zu quantifizieren. Die derzeit eingesetzten MRT basierenden Methoden zur Eisenquantifizierung sind nur in Gehirnregionen mit sehr geringem Myelingehalt, wie in der tiefen grauen Substanz, valide einsetzbar. Aussagen zum Eisenstoffwechsel in weißer Substanz konnten bis dato nur durch histopathologische Untersuchungen getroffen werden. In dieser Arbeit wird eine neu entwickelte Methode präsentiert welche mittels temperaturabhängiger Messung von Relaxationszeiten die Berechnung eines Temperaturkoeffizienten ermöglicht. Dieser Temperaturkoeffizient wird als Eisenmarker eingesetzt. Diese Methode basiert auf der Temperaturabhängigkeit der paramagnetischen Suszeptibilität, welche durch das Curie Gesetz beschrieben wird. Die diamagnetische Suszeptibilität, welche stark von Myelin beinflusst wird, ist von der Temperatur unabhängig und kann somit von der paramagnetischen Suszeptibilität, welche stark vom Eisen beeinflusst wird, unterschieden werden. Somit ist es erstmalig möglich, mittels MRT, Eisen unabhängig von Myelin in der weißen Substanz valide zu quatifizieren. Die hier präsentierten Daten wurden anhand verschiedener postmortalen MRT Aufnahmen gewonnen. Bei postmortalen MRT Untersuchungen spielen Faktoren wie Temperatur, Fixierung und Autolyse eine wichtige Rolle und beeinflussen den Bildkontrast, sowie quantitative MR Parameter. Der Einfluss dieser Faktoren in der postmortalen MRT wurde im Zuge dieser Arbeit untersucht. Durch diese Arbeit ist es nun möglich, genauere Aussagen zum Eisengehalt in weißer Substanz zu treffen und diese mit den verschiedenen Krankheitsaspekten bei MS zu verknüpfen.

# Schlüsselwörter

Magnetische Suszeptibilität, Eisen, Multiple Sklerose, Temperatur abhängige MRT, postmortale MRT, Formalin Fixierung

# Acknowledgement

and the great discussions during our meetings. A great thank you to Nikolaus Krebs for his discussion and support in all the post-mortem MRI experiments. Thank you to Prof. Klaus Schmierer and Daniele Carassiti of the Blizard Institute (Neuroscience) at the Queen Mary University of London for providing the MS tissue samples and performing the immunohistochemistry.

A special thank to all my colleges at the Institute of Medical Engineering. Thank you for all the great discussions and the great social events organized at the Institute.

I want to thank all my friends and address special thanks to Markus, Patrick and Daniel for their support and all the great coffee breaks discussing various kinds of things. Thank you to my friends from home, specially Dominik and Tim, for staying in contact over long distance and all the great skiing days back home. Thank you Rebecca for your help and taking your time for proofreading.

A big thank you to all the great people I met at the scientific conferences and who became friends during the last years.

I want to express my sincere gratitude to Prof. Franz Leberl for his motivation and advices during my studies. Thank you Franz for arousing my interest in science and motivating me for a PhD.

Last but not least I want to express my heartily gratitude to my beloved parents, Edeltraud and Andreas, my sister Katharina and my girlfriend Anna for their faith and support to study in Graz.

Thank you to all the important people in my live which are not mentioned here in person. It is a great honour to have so many great people in my live.

# Contents

# 1

# Introduction and Motivation

*"Non recuso laborem."*
*– Anonymus*

## 1.1 Introduction

The brain is the most complex organ of the human body, but therefore only fragmentary understood. For a very long time, the only way to "look inside" the human body was by performing an autopsy. In 1895 Wilhelm Conrad Röntgen discovered "a new kind of radiation" called x-rays or Röntgenstrahlen [1]. In 1901 Röntgen received the first Nobel Prize in Physics for his discovery of x-rays. For the first time it was possible to acquire images from inside the human body. Röntgen's discovery introduced medical imaging as a new and fast growing discipline in science. The first important improvement of the simple x-ray projection technique was the development of computed tomography (CT) scanning by Sir Godfrey Newbold Hounsfield [2] and Allan McLeod Cormack in 1971 [3, 4] (Nobel Prize in Physiology or Medicine 1979). CT scanning is a highly dynamic technique to acquire slice images based on multiple x-ray projections at different angles. The mathematical theory for CT image reconstruction was described by Johann Radon in 1917 [5].

After the discovery of nuclear magnetic resonance (NMR) by Felix Bloch [6] and Edward Mills Purcell [7] in the 1940's (Nobel Prize in Physics 1952) it took until the 1970's that Paul Christian Lauterbur [8,9] and Sir Peter Mansfield [10,11] convert this into Magnetic Resonance Imaging (MRI) (Nobel Prize in Physiology or Medicine 2003). Nowadays, there exists a wide spectrum of medical imaging techniques. The most promising image acquisition of the human brain, in remarkable detail, is MRI. But we are interested in more than the pure structure of the brain. In nature, there is no structure without function and no function without structure.

The complexity of the human brain and its capability to process an enormous amount of information is reflected in a network of more than 100 billion interacting neuronal cells. Further complexity of brain metabolism needs to be considered in the presence of a neurological disease. The investigation of the origin and course of neurological diseases is a challenging field in neuroscience. Thus, there is need for quantitative, image-based markers for diagnosis and monitoring the progression of neurological diseases.

Iron plays an important role in the human brain. To maintain a normal brain function, iron is involved in many different processes, such as oxygen transport, myelin production and mitochondrial respiration [12]. A disturbed iron metabolism has been linked with several neurological disorders like Alzheimer's disease (AD), Parkinsons's disease (PD) or multiple sclerosis (MS) [13]. MS is an inflammatory disease of the central nervous system (CNS) and the most common neurological disorder in young adults [14]. Focal demyelination of the white matter (WM) is causing axonal damage, resulting in a decreased signal conduction [15]. Furthermore, a decreased iron content is found in the center of the demyelinated WM lesions [16], in contrast to an increased iron content in the edge of WM lesions [16] and the basal ganglia [17]. There is strong evidence that the disturbed iron metabolism is linked with MS and its progression [18]. As this observation has been made in other neurodegenerative diseases as well, there is an increasing interest to non-invasively map the distribution of iron in tissue.

MRI is an attractive tool to assess regional iron concentrations based on the paramagnetic effect of iron inside a magnetic field. Quantitative MR parameters promise to serve as biomarkers for iron in the human brain [19]. There are several MRI techniques available to assess the iron content in human brain tissue based on relaxation time mapping [20–22], phase imaging [23,24], magnetic field correlation [25,26], direct saturation

imaging [27] and quantitative susceptibility mapping (QSM) [28–30]. These techniques can be used to reliable assess the iron content in neurodegenerative diseases, such as MS [31].

As the number of novel MRI techniques for iron assessment increases, the validation of these techniques is of increasing importance. Here, post-mortem MRI has shown a high potential to validate novel MRI iron mapping techniques [22, 28]. Furthermore, findings of post-mortem MRI studies of brain tissue increase the understanding of underlying structure and microarchitecture and its influence on biophysical contrast mechanisms.

Evidence suggests that iron accumulation is most prominent in deep gray matter (DGM) structures and can be reliably estimated using MRI [17]. Reliable quantification of iron is possible with varying sensitivity based on the chosen MRI technique, but restricted to gray matter (GM) structures. Common iron mapping techniques fail in the assessment of iron in WM, based on the strong counteracting contribution of the myelin [32].

Especially in normal appearing white matter (NAWM) and WM lesions of MS, disease related iron accumulation is not fully understood. Thus, there is need for a suitable MRI technique to quantify iron, independent of any diamagnetic contribution.

## 1.2 Objectives of the Thesis

The lack of a reliable MR method for iron mapping in all brain structures, especially in white matter, was the motivation for developing a novel MR based method to quantify iron using the temperature dependency of the magnetic susceptibility, described by Curie's law [33].

Therefore the main objectives of this project are:

- the development of a novel MRI-based technique to assess iron,
  - independent of any diamagnetic contribution, e.g. caused by myelin,
  - suitable for all brain regions;

- the application of the developed technique on formalin fixed post-mortem brain tissue of:
  - MS patients,
  - healthy controls;

- the comparison between MR-iron maps and histopathological staining.

The assessment of iron in post-mortem MRI depends on meeting the following special objectives:

- understanding the influence of the temperature in a post-mortem MRI experiment on the contrast and quantitative MR parameters;

- quantificating the influence of formalin fixation of brain tissue on MR relaxation times.

## 1.3 Structure of the Thesis

**Chapter 2** summarizes the state of the art in research of multiple sclerosis and iron in the healthy and diseased human brain from a medical and biological perspectives.
The fundamental physical basics of the magnetic susceptibility and the influence of iron on the magnetic susceptibility is discussed. The most important methods for detecting iron using MRI are discussed.

**Chapter 3** presents a study of the temperature dependency of the relaxation times $T_1$, $T_2$, $T_2^*$ and the magnetization transfer ratio (MTR) measured in unfixed human brain tissue.

**Chapter 4** focuses on the newly developed method to assess iron based on the temperature dependency of the paramagnetic susceptibility, described by "Curie's law". According to that only the paramagnetic part of the susceptibility changes with temperature while the diamagnetic part remains unaffected. Using temperature dependent relaxation time mapping, the iron content was estimated in different brain regions and validated using mass spectrometry and magnetometry.

**Chapter 5** studies the influence of formaldehyde fixation and temperature on MR relaxation times. The changes of the relaxation times were linked to the change in water content and molecular structure after fixation to evaluate the origin of the relaxation time decrease after formaldehyde fixation.

**Chapter 6** applies the newly developed method to assess iron based on the temperature

dependency of the magnetic susceptibility on formalin fixed tissue of multiple sclerosis brains. A validation was provided with subsequent immunohistopathology using ferritin light chain staining. The regional variations observed in histopathology were correlated with quantitative MR parameters. This work showed that the new proposed method is a valid and promising approach for iron mapping in all tissue structures, without a bias from diamagnetic contributions.

# 2

# Theory and State of the Art

*"Es gibt nichts Praktischeres als*
*eine gute Theorie."*
*– Gustav Robert Kirchhoff (1824-1887)*

## 2.1 Iron in the Human Brain

Iron is a fundamental part of many different processes in the human brain, such as oxygen transport, myelin production, DNA synthesis, mitochondrial respiration, neurotransmitter synthesis and neurotransmitter metabolism [12, 34–36]. A balanced iron metabolism is important to maintain normal brain function [13]. Iron enters the brain via the blood-brain-barrier or the CSF-brain barrier via the choroid plexus [37, 38]. The main iron components in the human brain are: (i) iron bound haemoglobin in the blood, (ii) iron bound ferritin for storage, (iii) to a lesser part iron bound in magnetite ($Fe_3O_4$) and maghemit ($\gamma - Fe_2O_3$) and (iv) iron bound to transferrin [39].

The ability of iron to switch the state from ferrous iron $Fe^{2+}$ to ferric iron $Fe^{3+}$, and vice versa, through electron exchange is important to maintain the balance between iron intake and iron storage. During iron intake, ferrous iron is oxidized by hydrogen peroxide

to ferric iron leading to a hydroxyl radical and a hydroxyde (equation 2.1). Upon storage, ferric iron is reduced to ferrous iron by hydrogen peroxide releasing hydroperoxyl radical and a proton as shown in equation 2.2.

$$\text{Fe}^{2+} + \text{H}_2\text{O}_2 \longrightarrow \text{Fe}^{3+} + \text{HO} \bullet + \text{OH}^- \tag{2.1}$$

$$\text{Fe}^{3+} + \text{H}_2\text{O}_2 \longrightarrow \text{Fe}^{2+} + \text{HOO} \bullet + \text{H}^+ \tag{2.2}$$
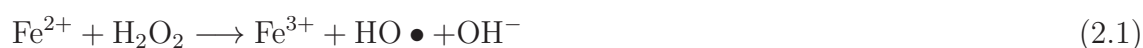
This redox process were first described by Fenton in 1894 [40] and produces free radicals promoting cytotoxic mechanisms as shown in figure 2.1 [18]. Free hydroxyl radicals oxidize lipids of membranes, denature proteins, damage DNA, lead to cell dysfunction and cell death and increase the concentration of intracellular free calcium [18]. Due to a disturbed iron homeostasis, the oxidative stress level is increased. The initiation of different cytotoxic meachanisms, lead to the damage of brain structure and function. To
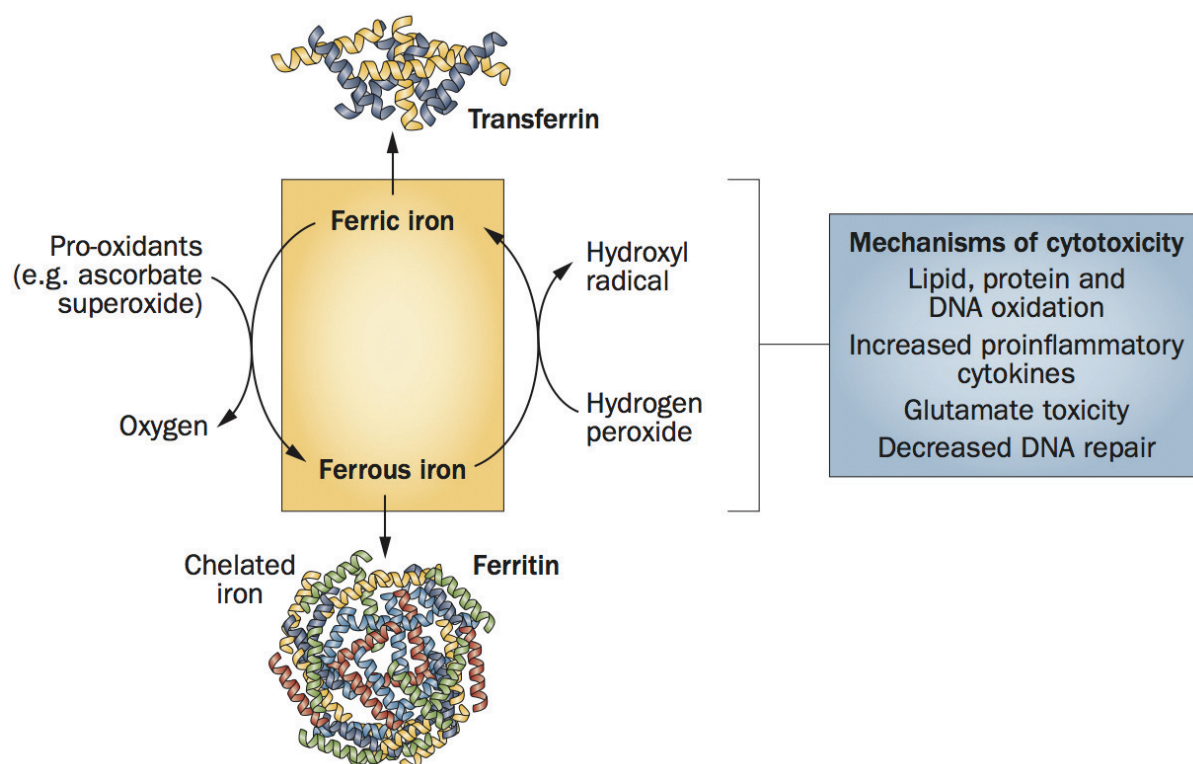


*Figure 2.1: Reaction of ferric iron to ferrous iron and vice versa. The release of hydroxyl radicals lead to cytotoxic reactions. Taken from [18].*

protect the brain from cytotoxic reactions and damage, iron is chelated through proteins in an complex called ferritin [41]. Ferritin is a protein consisiting of a mixture of 24 subunits of heavy chain (H-chain) and light chain (L-chain) ferritin proteins. The empty protein shell, called apoferritin, has a outer diameter of 12-14 nm and a hollow sphere with a inner diameter of 5-7 nm as shown in figure 2.2. Inside the shell, iron is stored as hydrated iron oxide ($5Fe_2O_3 \cdot 9H_2O$) called ferrihydrite [39, 42]. The ferritin protein cage is very stable and resists temperatures >80 ℃ at pH 7 in a solution. Damaged ferritin is called hemosiderin which is defined as insoluble cellular iron [41]. Beside iron bound



$$Fe(2^+) + O_2 + H_2O == Fe(3^+) + H_2O_2$$
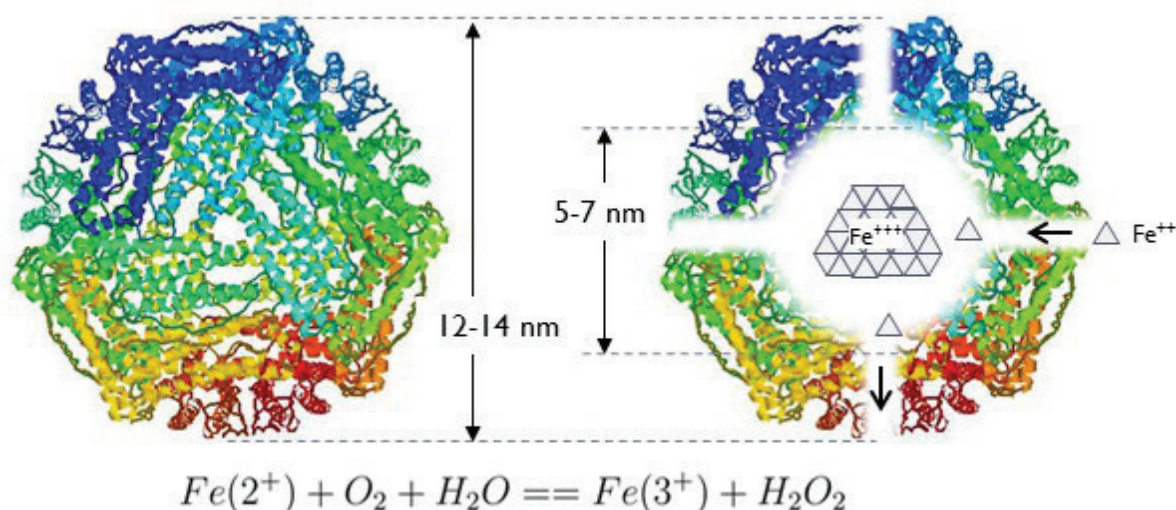
Figure 2.2: *The structure of ferritin protein shell. The shell is consisting of 24 subunits of heavy (H) and light (L) chain ferritin. The reaction of $Fe^2+$ with $O_2$ and $H_2O$ to a safe ferryhydrite core.*

in a non-reactive form to ferritin, small amounts of iron bound to low-molecular-weight compounds is found in several cellular compartements such as the nucleus, cytosol, lysosomes and mitochondria. This represents the labile iron pool reactive for oxygen species producing hydroxyl radical and leading to tissue damage [43–45].

For the detection of non-haemin iron in tissue slices, primarily histochemical methods are utilized. The most common staining methods are pearl's staining, turnbull blue staining or DAB enhanced turnbull blue staining [46, 47]. Additionally to turnbull blue staining, Hallgren and Sourander determined the iron concentration in homogenized tissue samples colorimetrically with a spectrophotometer [48]. A more specific method compared to standard histopathology are immunohistochemical methods based on antibody reactions.

Specific antibodys bind weakly to receptors of the ferritin protein.

In the healthy brain iron is primarily accumulated in oligodendrocytes, microglia and macrophages [49]. The normal metabolism in the aging brain include the accumulation of iron in different brain regions. Hallgren and Sourander showed already in 1958 that iron increases until the forth decade of live in different deep gray matter structures with different rates until a plateau is reached. The highest iron concentrations were found in globus pallidus, caudate nucleus, putamen, dentate, substantia nigra and red nucleus [50]. In figure 2.3 the increase of iron concentration in the globus pallidus is shown.

  A disturbed iron metabolism, causes abnormal iron accumulation in different brain re-
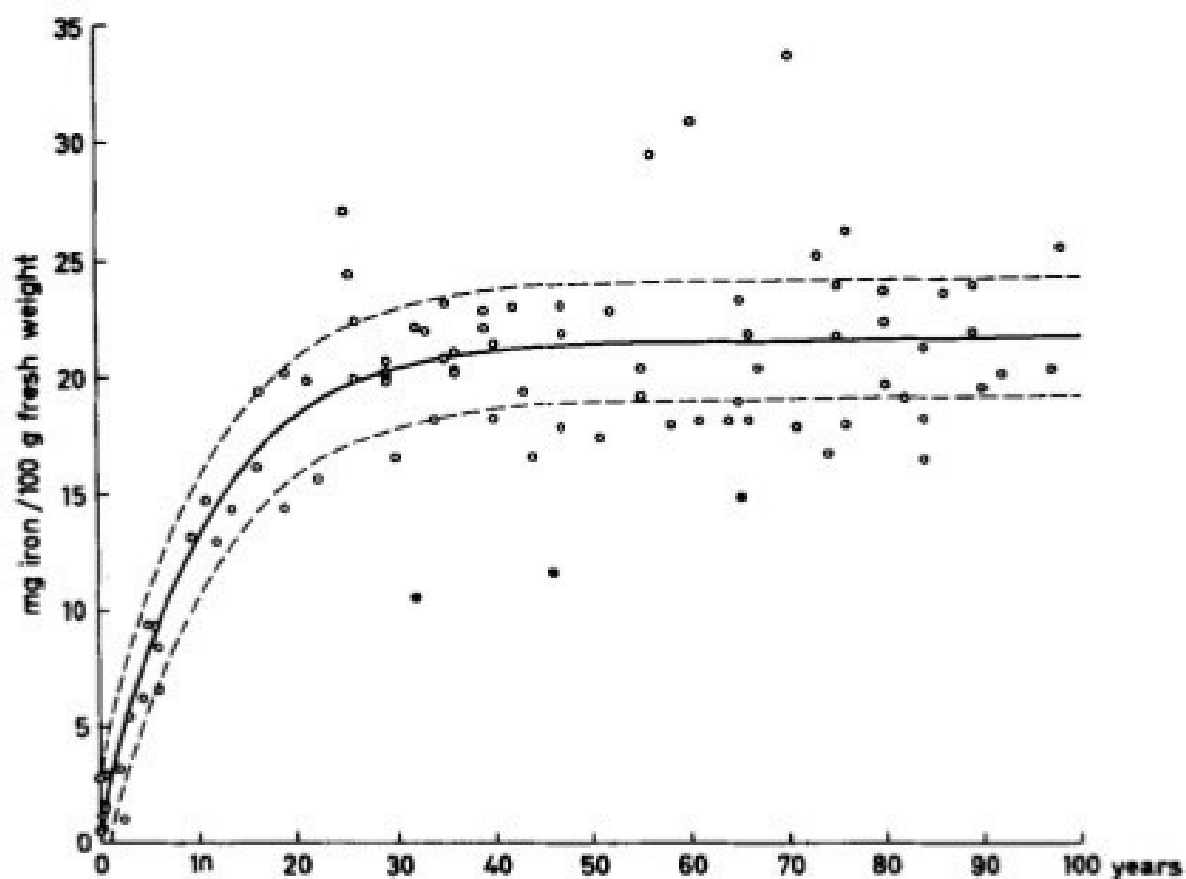


*Figure 2.3: Non haemin iron concentration in the globus pallidus at different age. Taken from [48].*

gions and contributes to an increased release of reactive oxygen species. These reactive oxygen species cause oxidative stress and cell death leading to neurodegeneration. Iron accumulation beyond the healthy range is observed in several neurodegenerative diseases

including Alzheimer's disease, Parkinson's disease and multiple sclerosis [13]. Until now, it is still unclear if iron accumulation is the primary effect triggering the disease or a secondary effect caused by the disease.

As iron is an important part of the myelin production, iron metabolism in multiple sclerosis is of great importance and directly linked with the disease.

## 2.2 Multiple Sclerosis

This chapter summarizes several review articles dealing with multiple sclerosis to give an overview of the most important facts of this disease [14, 15, 51]. Multiple sclerosis (MS) is the most frequent disorder of the CNS with more than 2.5 million affected individuals around the world. MS is the most common neurological disease in young adults with a prevalence of one in 400 [14]. Pathologically, MS is an inflammatory disease of the CNS leading to acute focal demyelinated lesions, diffuse neurodegeneration and axonal loss in gray and white matter [52]. The disease is categorized into (i) primary progressive MS (PPMS), (ii) relapsing-remitting MS (RRMS) and (iii) secondary progressive MS (SPMS). In the PPMS course, there is an continuous progression of the disease starting from the onset [53]. In RRMS, relapses occur approximately 1-2 times per year with different strengths and different intervalls between the relapses. The relapses are linked to the formation of new focal lesions where most of them become permanent sclerotic plaques. Persisting disease duration implicates increased axonal loss, as well as decrease of the brain volume, in the cause of time. After several years, the relapse remitting course is followed by the secondary progressive phase. A typical course and the corresponding pathogenesis of RRMS followed by SPMS is shown in figure 2.4. Inflammatory and neurodegenerative processes are connected and overlapping with ongoing disease duration.

Oligodendrocytes are glial cells of the CNS and responsible for myelin production. Myelin consists of lipids separated through different layers [54, 55]. The myelin sheaths are wrapped around axons, as an insulating membrane and responsible for fast signal transduction. This so called saltatory conduction is based on the propagation of action potentials between the nodes of Ranvier. The nodes of Ranvier are the unmyelinated spots between the myelinated parts of the axon [54, 55]. If the myelination of the axon is damaged, the signal conduction is dramatically delayed.

Neurodegeneration, caused by myelin loss, results in axonal damage and is typical in an early stage of active focal lesions. Axonal damage in active focal lesions begin early with
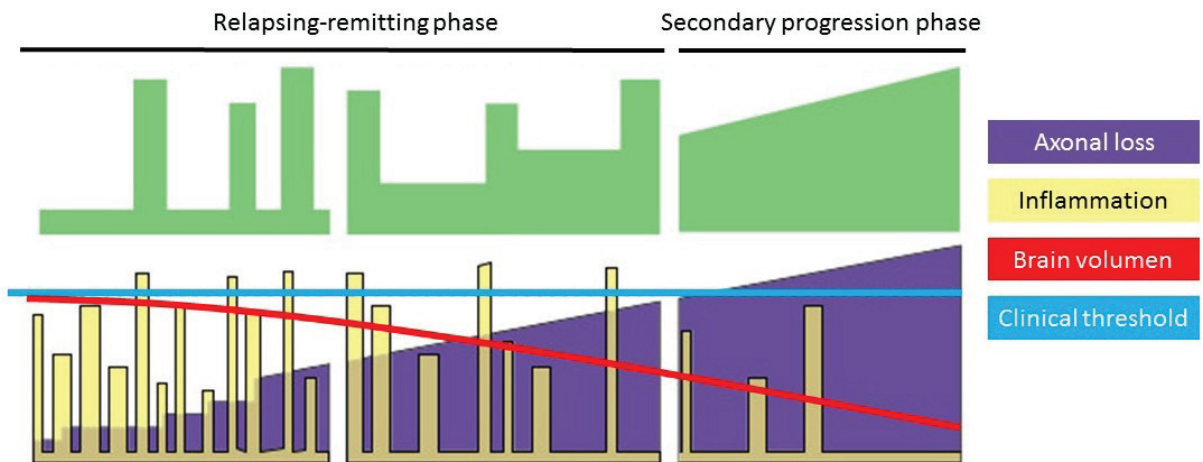
*Figure 2.4: The course and pathogenesis of a typical relapsing-remitting and later on secondary progressive MS. The change of brain volume, axonal losses and inflammation are plotted compared to disease state. Adapted from [14].*

the formation of new lesions and increases with disease duration. This progressive neurodegeneration is irreversible. In the case of partial remyelination in inactive lesions, the underlying axonal density is still decreased.

The axonal demyelination lead to a varity of different clinical symptoms. Common symptoms are weakness or diminished dexterity in the limbs, sensory disturbance, monocular visual loss, double vision, gait instability and ataxia. In later stages of disease it comes to bladder dysfunction, fatigue and heat sensitivity. Further hemifacial weakness, pain, vertigo and brief tonic spasms could occur. These symptoms are not exclusively MS specific. Characteristic symptoms for MS are Lhermitte's symptom, an electrical sensation running down the spine or limbs during neck flexion and Uhthoff phenomenon, where worsening of symptoms appear when the body temperature is rising [14, 15, 51]. The demyelination is also reflected in a prolonged latency of visual, auditory and somatosensory envoked potentials. Further, cognitive dysfunctions with memory loss, impaired attention, delayed information processing, problem solving difficulties, difficulties in shifting between cognitive tasks are prominent in MS [56–60].

Inflammation arising from accumulating active T lymphocytes initiate the cascade of events resulting in demyelination. Inflammatory mediators lead to an impaired blood brain barrier. Consequently nitric oxide damages axons and block the conduction. Reactive astrocytes release cytokines and growth promoting factors as part of the inflammatory

process leading to possible remyelination in some cases. On the other hand, gliosis can occur, blocking the remyelination. WM pathologies are characteristic for MS and reflected in the diagnostic criterias of MS [61].

In many cases clinical evidences are sufficient for the diagnosis of MS or non-MS and additional examinations are not needed [15]. If clinical evidence is not sufficient, additional biomedical analysis of blood or CSF [62, 63] or MRI support a definite diagnosis. Criteria for the diagnosis of MS based on clinical, biomedical and imaging data are visualized in figure 2.5.

In the process of diagnosing MS, MRI plays an important part. More than 95% of the MS patients show WM abnormalities in $T_2$ weigted images. The focal lesions are represented as areas with higher signal intensity on $T_2$ weighted images. Active lesions are caused by an impaired blood brain barrier and distinguished from other lesions using gadolinium enhanced MRI. MRI has proven as suitable tool to monitor the progression of MS through calculating brain atrophy at different disease stages [64] or monitor $T_1$ contrast changes in lesions [65] or changes in WM tracts using diffusion tensor imaging [66].

For a long time, MS was primary associated as disease of the WM, but more and more evidence suggest an involvement of gray matter structures. Cortical gray matter lesions seem to influence the cause of the disease and contribute to motory, sensory and cognitive dysfunctions [67, 68]. Demyelination occurs not only in WM, but also to a certain degree in cortical or deep gray matter. Gray matter atrophy is observed in pathological studies and linked with abnormal iron levels in deep gray matter structures [69].

### 2.2.1 Iron in Multiple Sclerosis

As in many neurodegenerative diseases, a disturbed iron metabolism is associated with MS. In MS, increased iron levels are found in deep gray matter structures such as globus pallidus, caudate, putamen, thalamus and substantia nigra [17, 23, 70–72]. The increased iron levels are linked to gray matter atrophy, diffuse neurodegeneration on a pathological level and with disease progression and disability on a clinical level. Abnormal iron levels and neurodegeneration was found in all types of MS [18, 69]. The iron levels of deep gray matter structures where significantly higher than in the the iron levels in the cortex and normal appearing white matter (NAWM) of MS patients. Lower iron levels were found in deep gray matter structures of patients with a clinically isolated syndrome (CIS) compared to RRMS and SPMS patients [17, 71]. No increase of iron in deep gray matter
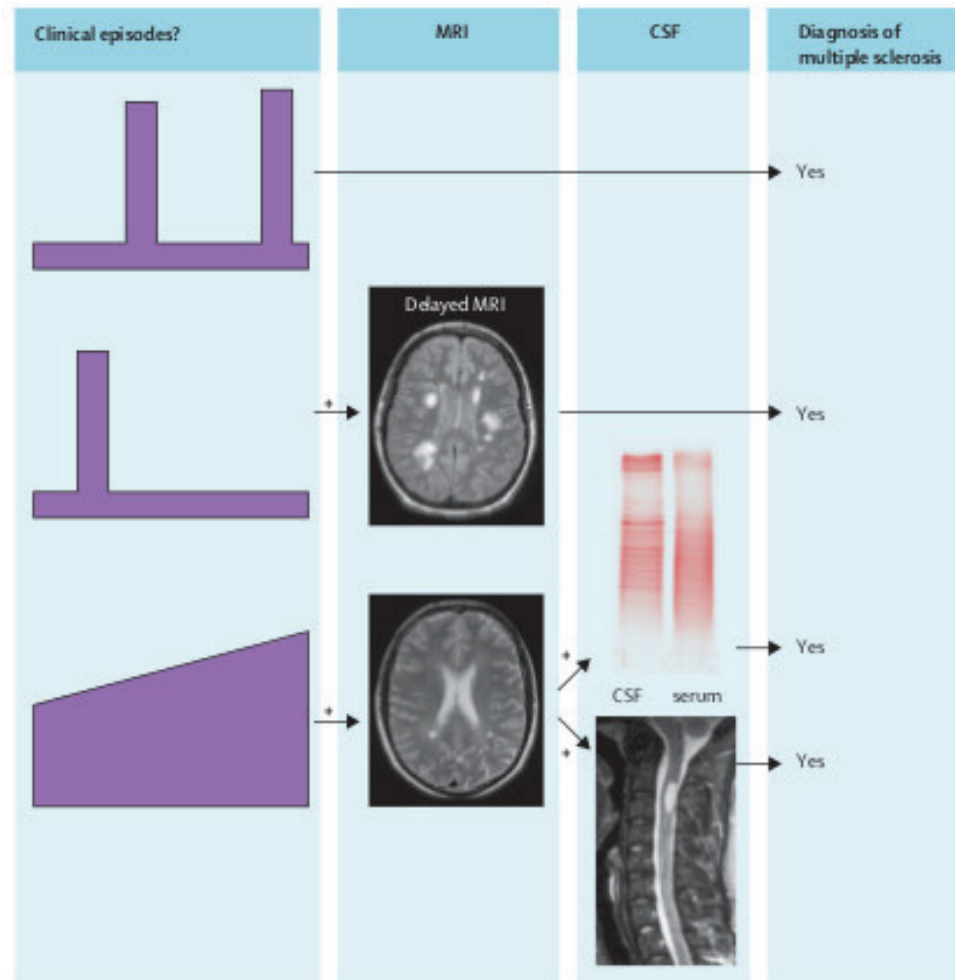
Figure 2.5: Criteria for the diagnosis of multiple sclerosis, adapted from the McDonald criteria. Taken from [15]

structures of MS patients was observed compared to the age dependent increase of iron in healthy controls [48].

Iron increases in the deep gray matter structures during ageing in healthy controls [50]. In MS no such increase with age was observed.

In focal demyelinated lesions, increased iron levels are observed at the rim around the lesion core. In the lesion core demyelination and decreased iron was observed in a histopathological study [16]. Late active lesions show high iron content compared to chronic and remyelinated lesions where low iron content was observed [16, 73]. In some studies, iron was found around blood vessels such as small veins inside WM lesion cores [46, 74].

In NAWM, iron levels are found to be decreased compared to control patients. This decrease of iron in NAWM is correlated with the disease duration. Beside low iron levels, a loss of oligodendrocytes and reduced hephaestin, a membrane protein responsible for transmembrane iron transport, was observed [16]. This decrease of iron is suggested to play a protective role against inflammation mediated demyelinisation and oxidative stress.

In MS, it is suggested that several different mechanism contribute to the disturbed iron metabolism leading to abnormal iron accumulation or iron loss in different brain structures [18, 75, 76]. In the healthy brain, iron regulatory proteins, are responsible for a balanced intake, storage and release of iron. Dysregulation of iron transport, iron storage and other regulatory molecules might be responsible for abnormal iron accumulation. Transferrin is responsible for iron transport in the blood and into cells. Iron is transported across the blood-brain-barrier via transferrin receptors of brain endothelial cells. A dysfunction or break down of the blood-brain-barrier lead to an unregulated intake of iron from the blood to the extracellular space. Lysis of erythrocytes, degeneration of haemoglobin and microhaemorrhages are considered as possible sources of increased iron deposition.

An overload of reactive ferrous iron ($Fe^{2+}$) can increase the amount of reactive oxygen species, such as hydroxyl radicals, via the Fenton reaction. In MS there is evidence of widespread mitochontrial damage based on increased oxidative stress. Iron-dependent enzymes are found in oligodendrocytes and responsible for normal oxidative metabolism. An overload of reactive iron is toxic to neurons and oligodendrocyes and contribute to the demyelination process. The most intense demyelination was observed in the center of focal WM plaques. Beside demyelination in WM, an iron dependent demyelination of gray matter was observed among all MS types [69]. Variance of demyelination was observed with the highest values in the caudate and hypothalamus. Demyelinated lesions in the deep gray matter were observed in all types of MS, most frequent in the caudate and hypothalamus. There are two different strategies to protect the brain from iron mediated damage: (i) chelation of free iron to a safe and non reactive form and (ii) reducing free radicals through antioxidants.

Chelators are substances, which bind the free circulating iron and prevent redox reactions and therefore the production of free radicals. Studies with experimental autoimmune encephalomyelitis (EAE), which mimics the inflammatory and demyelinating processes of MS, showed possible benefits of a chelator based therapy against iron abnormal accumulation. If already free radicals are present, antioxidants can be used to prevent tissue
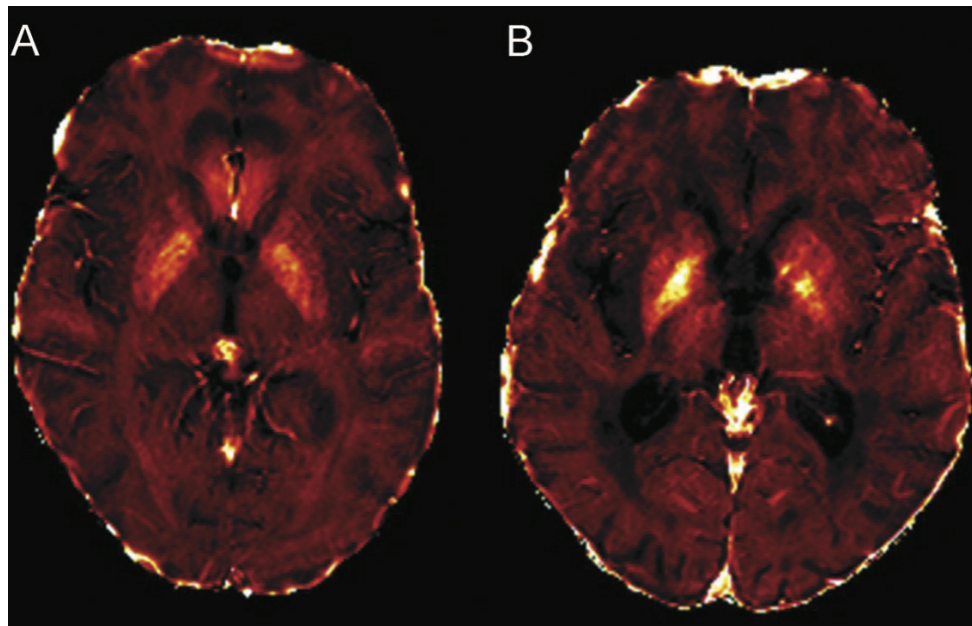
*Figure 2.6: $R_2^*$ map of a patient with CIS (A) and a patient with MS (B). Increased $R_2^*$ values in the globus pallidus and putamen were observed in MS compared to CIS, indicating an increas in iron concentration. Taken from [71].*

damage. Several vitamins (A,C,E), coencyme Q10, green tea extract, nitric oxide or Ginko biloba were successfully applied as antioxidants in EAE studies. In WM plaques a decreased level of antioxidants and higher levels of oxidative stress markers were observed [77, 78].

Therapies to protect iron mediated damage worked well in animal studies but still now suitable results from human studies are available. Therefore the benefit in MS therapy is still an open question.

## 2.3 Magnetism of Matter

Magnetism of matter and the origin of magnetic effects can not be explained in terms of classical physics. If classical physics is used, an equivalence to magnetic dipoles, represented by circulating currents, is assumed. The existence of magnetic monopoles, analogue to the electric charge, is not observed in nature. A detailed explanation and discussion of magnetism of matter without quantum mechanics is not possible. The following fundamental principles in this chapter are based on several text books [79–81].

Magnetism is caused by atomic currents as a motion of electric charges and/or by the spin of elementary particles, such as electrons, protons and neutrons, characterized by their magnetic moment. Macroscopically, the total magnetic moment of an atom is the sum of the individual magnetic moments from the electrons, protons and neutrons. In an atomic system, the total magnetic moment is the sum of all individual magnetic moments inside the system. Further, a magnetic moment is induced through an external magnetic field which superimposes the internal magnetic moment in positive or negative manner.

To understand the total magnetization of a system, one has to exploit the intrinsic magnetic moment caused by a single particle. Therefore we have to differentiate between the magnetization caused by the spin of an electron and the magnetization caused by the spin of a nucleon. One the one hand, the nuclear spin of a proton is the fundamental basis for nuclear magnetic resonance (NMR) which is fundamental for MRI. On the other hand, the spin of the electron is the dominating origin for the magnetic property of matter.

At atomic level, the magnetic moment of a free electron inside an atom has two different origins: (i) the spin $\mathbf{S}$ of the electron and (ii) the orbital angular momentum $\mathbf{L}$ caused by the movement of the electrons around the nucleus. The combination of spin and orbital momentum is summarized as total angular momentum $\mathbf{J}$ with $\mathbf{J} = \mathbf{S} + \mathbf{L}$.

The simplest atom, is the hydrogen atom with one proton and one electron. The magnetic moment $\mu$ of the electron is

$$\boldsymbol{\mu} = -g \left( \frac{q_e}{2m_e} \right) \mathbf{J} \tag{2.3}$$

where $q_e$ is the charge of the electron, $m_e$ is the mass of the electron and $g$ the "Landé g-factor", which is defined as:

$$g = \frac{3}{2} + \frac{S(S+1) - L(L+1)}{2J(J+1)} \tag{2.4}$$

The Landé g-factor of a atomic system describes the weighting of the momentum and is equal to g = 1 for pure orbital motion (S = 0) and to g = 2 for a pure spin momentum (L = 0).

When we look only at the nuclei of an atom, we have protons and neutrons moving slightly around, which possess an intrinsic spin, called nuclear spin $\mathbf{I}$. The total momentum is now defined as $\mathbf{J} = \mathbf{I} + \mathbf{L}$ and therefore the magnetic moment of a proton can be expressed as

$$\boldsymbol{\mu_p} = g_n \left( \frac{q_e}{2m_p} \right) \mathbf{J} \tag{2.5}$$

where $m_p$ is the mass of the proton and $g_n$ the nuclear g-factor. The nuclear g-factor is different to the Lande g-factor. The nuclear g-factor of a proton is +5.585. Like the electron and proton, the neutron has a magnetic moment with a nuclear g-factor of -3.826. Since the magnetic moment is scaled with the inverse of the particle mass the magnetic moments produced by the nucleus are typically much smaller than the magnetic moments produced by the electrons. Typically the factor is between $10^{-3}$ to $10^{-4}$.

An atomic magnet, with a magnetic moment proportional to the total angular momentum, will precess with a distinct frequency when it is placed inside a magnetic field. Therefore the magnetic moment is expressed as

$$\boldsymbol{\mu} = \gamma \mathbf{J} \tag{2.6}$$

where $\gamma$ is a particle dependent constant called gyromagnetic ratio. The magnetic moment precesses around the magnetic field $\mathbf{B}$ along the z-axis with the frequency

$$\omega_L = \gamma \mathbf{B} \tag{2.7}$$

which is called Larmor frequency. The gyromagnetic ratio for the electron can be expressed as $\gamma = -q_e/2m_e$. The same holds true for the magnetic moment produced by the
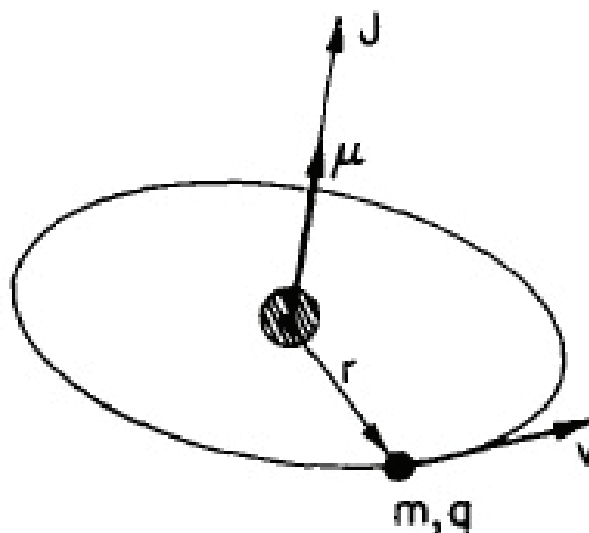
*Figure 2.7: A charged particle circulating in an orbit shows a magnetic moment $\mu$ in line with the angular momentum $J$. Taken from [79].*

proton. Therefore the different nuclei possess a different gyromagnetic ratio and Larmor frequency.

In quantum mechanics the relationship between magnetic moment and angular momentum is described in terms of energy. The energy of a magnetic moment in a magnetic field is given as

$$E_{mag} = -\mu \cdot \mathbf{B} \tag{2.8}$$

When we look now on the z component of the angular momentum, with the z axis is parallel to the magnetic field, only certain discrete values are possible. If the spin j is given, there are 2j + 1 possible states and $J_z$ can only take values between $j\hbar$, $(j-1)\hbar$, $\cdots$, $-j\hbar$. For example a system with spin 1/2 has two possible states with $-\hbar/2$ and $+\hbar/2$. Hence the magnetic energy of an atomic system has only certain values corresponding to

$$E_{mag} = g\left(\frac{q_e}{2m_e}\right) J_z B_z \tag{2.9}$$

If we insert for $J_z$ the maximum possible value $j\hbar$ we can express the energy as

$$E_{mag} = g\left(\frac{q_e}{2m}\right)\hbar j B_z \tag{2.10}$$

and define the "Bohr magneton" now as

$$\mu_B = \frac{q_e \hbar}{2m} \tag{2.11}$$

which represents the smallest possible magnetic moment. Finally, the energy of the system is given as

$$E_{mag} = g\mu_B j B_z \tag{2.12}$$

If we look again on a electron at rest without an orbital motion we have spin $1/2$ and for full spin moment g = 2. Therefore the energy can either be $\pm\mu_B B$. This is often referred as spin "up" or spin "down" of the electron. Compared to the electron, the energy of the proton is given as

$$E_{nucleus} = -g\mu_p i B_z \tag{2.13}$$

where i is the z component of the angular momentum of the nucleus. The change in the sign is based on the positive charge of the nuclei and the negative charge of the electron. The possible energy states of an electron is shown in figure 2.8. The two energy states are corresponding to the "spin-up" and "spin-down" state of the electron.

We can now calculate the fundamental magnetic moments of the electron and proton and comapere their values. The magnetic moment of a single electron is $\mu_B = 9.274 \times 10^{-24} Am^2$ and the magnetic moment of a proton is $\mu_p = 1.410 \times 10^{-26} Am^2$. Here, the contribution of the proton is much smaller than the contribution of the electron. Thus, in many cases the contribution of the nuclear magnetic moment is neglected.

In quantum mechanics the hamiltonian $\mathcal{H}$ represents the total energy of an atomic system. An atom with Z electrons can be represented as

$$\mathcal{H}_0 = \sum_{i=1}^{Z}\left(\frac{p_i^2}{2m} + V_i\right) \tag{2.14}$$
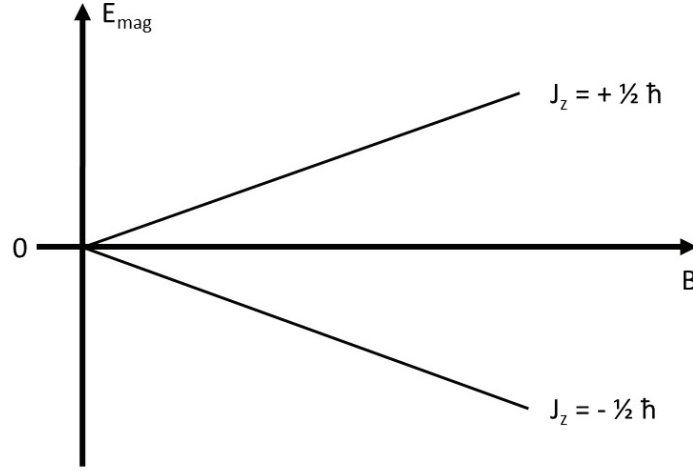
*Figure 2.8: The two possible energy states of an electron inside a magnetic field.*

where $\frac{p_i^2}{2m}$ is the kinetic energy and $V_i$ the potential energy of the $i^{th}$ electron in the atom. If the atom is placed in a magnetic field the initial hamiltonian $\mathcal{H}$ is perturbed through a paramagnetic and diamagnetic contribution and can be represented as

$$\mathcal{H} = \mathcal{H}_0 + \mu_B(\mathbf{L} + g\mathbf{S}) \cdot \mathbf{B} + \frac{e^2}{8m_e} \sum_i (\mathbf{B} \times \mathbf{r}_i)^2 \tag{2.15}$$

where $\mu_B(\mathbf{L} + g\mathbf{S}) \cdot \mathbf{B}$ is the paramagnetic term and $\frac{e^2}{8m_e} \sum_i (\mathbf{B} \times \mathbf{r}_i)^2$ the diamagnetic term. The terminology using the hamiltonian will be useful for describing complex magnetical effects and interactions between magnetic moments as described later in this chapter.

## 2.3.1 Magnetization and Field

In the previous chapter the fundamental magnetic moment of the electron and nucleus were defined and their different contributions were shown. To characterize an atomic system or material with a large number of individual magnetic moments the magnetization $\mathbf{M}$ is defined. The magnetization $\mathbf{M}$ is the net magnetic moment of all atoms per volume. If there are N atoms in the unit volume the total magnetization is represented as

$$\mathbf{M} = N \sum_i \mu_i \tag{2.16}$$

where $\mu_i$ is the average magnetic moment of a single atom inside the volume.

In free space, the magnetic field is represented either using the vector fields **B** or **H** which are related according to

$$\mathbf{B} = \mu_0 \mathbf{H} \tag{2.17}$$

where $\mu_0$ is the permeability of the free space. In free space without matter there is no magnetization. In literature two different unit systems are used: (i) the centimeter, gram, second (CGS) system and (ii) the meter, kilogram, second (MKS) system which has been adopted into the SI system of units. In the SI system **H** is given in ampere/meter (A/m), **B** in tesla (T) and $E$ in joule (J) where as in the CGS system **H** is given in oersted (Oe), **B** in gauss (G) and $E$ in erg. This can be confusing and one has to be aware of the chosen unit system when comparing different literature.

If a material is placed inside a magnetic field, the relationship between **B** and **H** is getting more complex and is given as

$$\mathbf{B} = \mu_0 (\mathbf{H} + \mathbf{M}). \tag{2.18}$$

Depending on the properties of the material, the magnetization **M** increases or decreases with the external magnetic field. This leads to the magnetic induction **B** in Tesla (T). **H** is called the magnetic field and is given in Ampere/meter (A/m). In the SI system **B** is defined as described in equation 2.18 and in the CGS system **B** is defined as

$$\mathbf{B} = \mathbf{H} + 4\pi \mathbf{M} \tag{2.19}$$

Often both, the magnetic induction **B** and the magnetic field strength **H**, are referred as the magnetic field. So, confusion between the usage and definition of **B** and **H** is common. In MRI, it is preferred to determine the magnetic field as **B** in units of Tesla. Here in this thesis, the SI units are used if not explicitly quoted.

### 2.3.2 Magnetic Susceptibility

The magnetic susceptibility is a fundamental physical quantity relating the magnetization with the magnetic field and describes the magnetic properties of matter. The magnetic

properties are classically classified into weak induced magnetism (diamagnetism and paramagnetism) and into strong spontaneous magnetism (ferromagnetism, ferrimagnetism and antiferromagnetism).

In materials with fully filled electron shells, permanent magnetic moments are missing. Thus, these materials are called diamagnetic. If a diamagnetic material is placed inside a magnetic field, a current is induced according to Lentz's law leading to a decreased magnetic field. Materials with unfilled electron shells possess small magnetic moments and are called paramagnetic. These small magnetic moments are oriented randomly based on the thermal motion. If a magnetic field is applied, the magnetic moments start to align in the direction of the magnetic field.

The difference between diamagnetic an paramagnetic materials can be shown in a simple experiment where a material is placed between the poles of a magnet as shown in figure 2.9. A diamagnetic material will be repelled out of the field, whereas a paramagnetic material will be attracted towards the field. Materials with aligned permanent magnetic
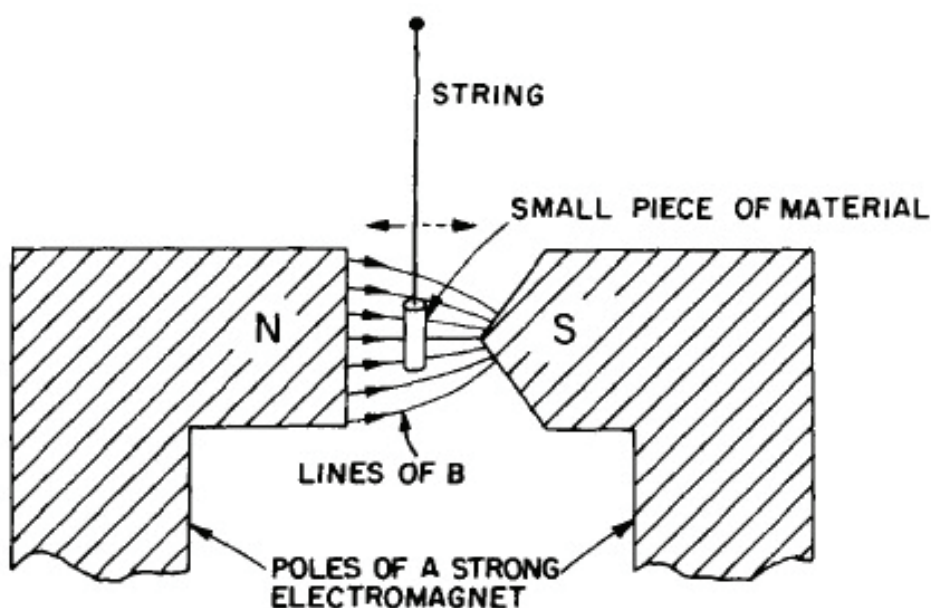


*Figure 2.9: A small cylinder of material is repelled or attracted toward the sharp pole of a magnet depending of the magnetic property. Taken from [79].*

moments are called spontaneous magnetic materials. Ferromagnetic materials show spontaneous magnetization, even in absence of an external magnetic field. In a ferromagnet, all magnetic moments are aligned in the same direction and interacting to a strong net magnetic moment. In an antiferromagnetic material, the direction of the magnetic moments

are depending on the neighbourhood and are spontaneous oriented in an antiparallel way. In an ideal antiferromagnet, no magnetic effects are observed outside the object because the magnetic moments are ideal antiparallel matched, resulting in zero net magnetization. In ferrimagnetic materials, the magnetic moments are interacting. There is a mixed ordering in parallel and antiparallel direction with one dominating direction resulting in a total non-zero magnetic moment. The different ordering states without magnetic field are shown in figure 2.10.

The magnetic property of a material is represented by the magnetic susceptibility $\chi$ which can be defined as (i) volume susceptibility, (ii) mass susceptibility and (iii) molar susceptibility. The volume susceptibility is defined as

$$\chi = \frac{M}{H} \tag{2.20}$$

in the CGS system and defined as

$$\chi = \frac{\mu_0 M}{B} \tag{2.21}$$

in the SI system. The magnetic susceptibility is principal referred to the volume susceptibility and a dimension less quantity in both, the CGS and the SI unit system. The magnetic susceptibility can additionally be defined as mass susceptibility according to

$$\chi_m = \frac{\chi}{\rho} \tag{2.22}$$

where $\rho$ is the density of the material. The mass susceptibility has the unit $m^3/kg$ in the SI system and $emu/g$ in the CGS system. The molar susceptibility is given by

$$\chi_M = \frac{\chi MW}{\rho} \tag{2.23}$$

where $MW$ is the molecular weight in $g/mol$ (CGS) or $kg/mol$ (SI).
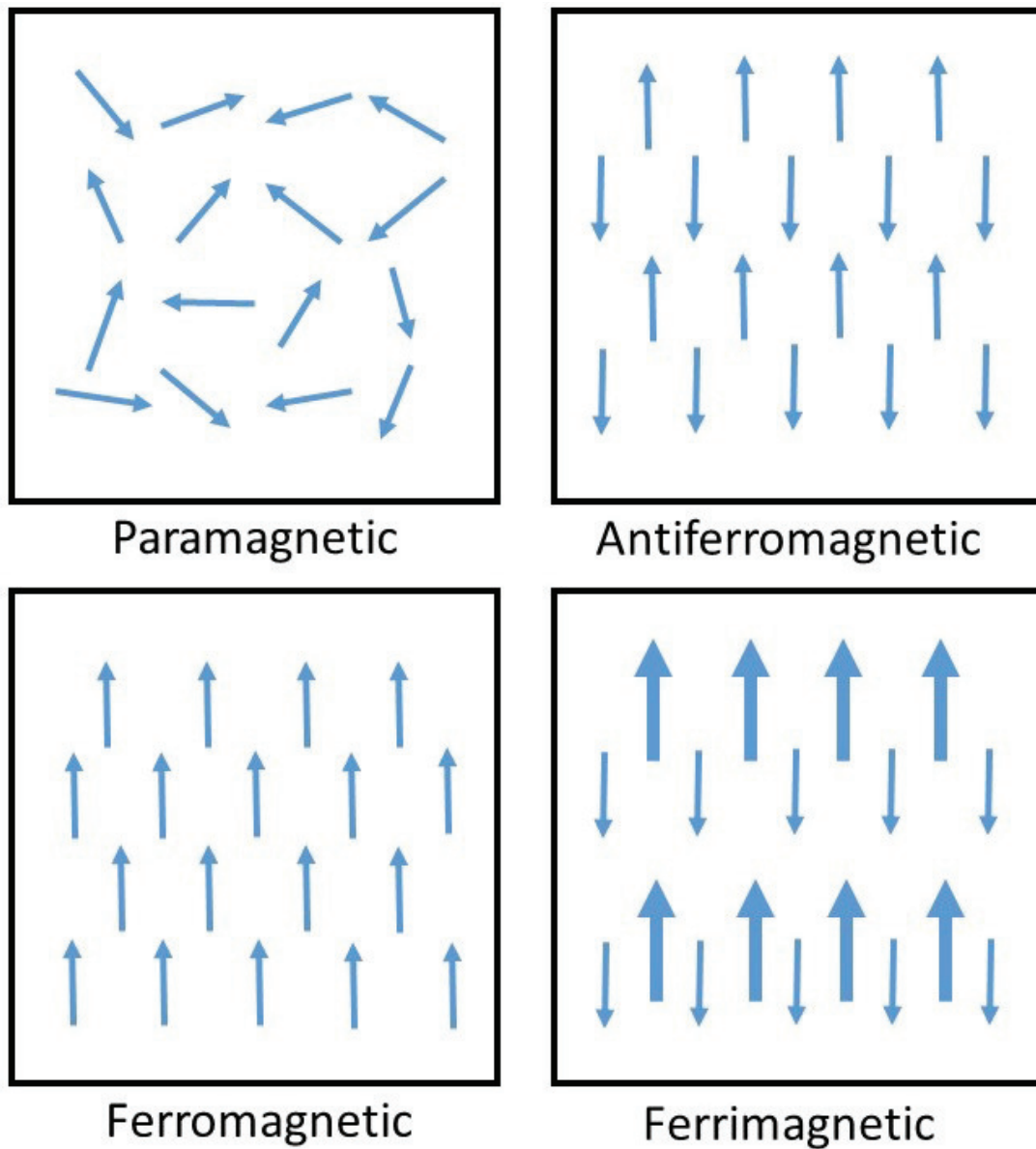
Figure 2.10: *The different ordering of the magnetic moments without an external magnetic field. In a paramagnetic material the spins are arranged based on the thermal average. In antiferromagnetic materials the two sublatice are canceling each other. Where as in a ferrimagnetic material one sublatice is dominating leading to a net magnetic moment. The spins in ferromagnetic materials are pointing in the same direction without magnetic field.*

### 2.3.3 Diamagnetism

Diamagnetism is a purely quantum mechanical effect. Atoms or molecules with fully filled orbitals have no permanent magnetic moment and called diamagnetic. If a diamagnetic material is placed inside a magnetic field, a current is induced based on "Lentz's law". This leads to a magnetic moment opposite to the external magnetic field which induced the current. The maximum diamagnetic contribution is given in the case of a magnetic field perpendicular to the orbital plane, which represents the current loop.

In the case of diamagnetism, there is no magnetic moment without an external magnetic field. Through the external magnetic field, the frequency of the current inside the atom is changed, an the relation ship is described by the Larmor frequency:

$$\omega_L = \frac{q_e B}{2m_e} \tag{2.24}$$

The change of the electron rotation caused by the external field is leading to a reduction of the magnetic moment $\Delta\mu$ described by:

$$\Delta\mu = -\frac{q_e^2}{4m_e}(x^2 + y^2)B \tag{2.25}$$

If there are Z electrons per atom and N atoms per unit volume, the diamagnetic susceptibility is defined as:

$$\chi = -\frac{q_e^2 N}{4m_e} \sum_{i=1}^{Z} \left(x^2 + y^2\right)_i = -\frac{q_e^2 N Z}{6m_e} \langle r^2 \rangle_{av} \tag{2.26}$$

The diamagnetic susceptibility has negative values and is not depending on the temperature. The largest diamagnetic contribution is present in materials with delocalized $\pi$ electrons. This electrons are very mobile and the induced current can reach large values. Diamagnetism is present in all materials but usually very weak and in many materials the diamagnetic contribution is negligible compared to other stronger magnetic effects.

### 2.3.4 Paramagnetism

Paramagnetic materials have positive susceptibility compared to the negative susceptibility of diamagnetic materials. Atoms without a fully filled shell have an non vanishing orbital and/or spin momentum and hence a net magnetic moment. In a material with

a certain amount of magnetic moments and no external magnetic field, this magnetic moments are pointing in all directions based on their thermal motion. If a paramagnetic material is placed in a magnetic field, the small magnetic moments start to align with the field, as shown in figure 2.11, leading to an additional positive contribution in the direction of the external field. With increasing field strength the alignment of the magnetic moments is getting stronger. Whereas an increasing temperature counteracts the alignment and randomizes the spins.

The paramagnetism is usually weak because the lining up forces are relatively small com-
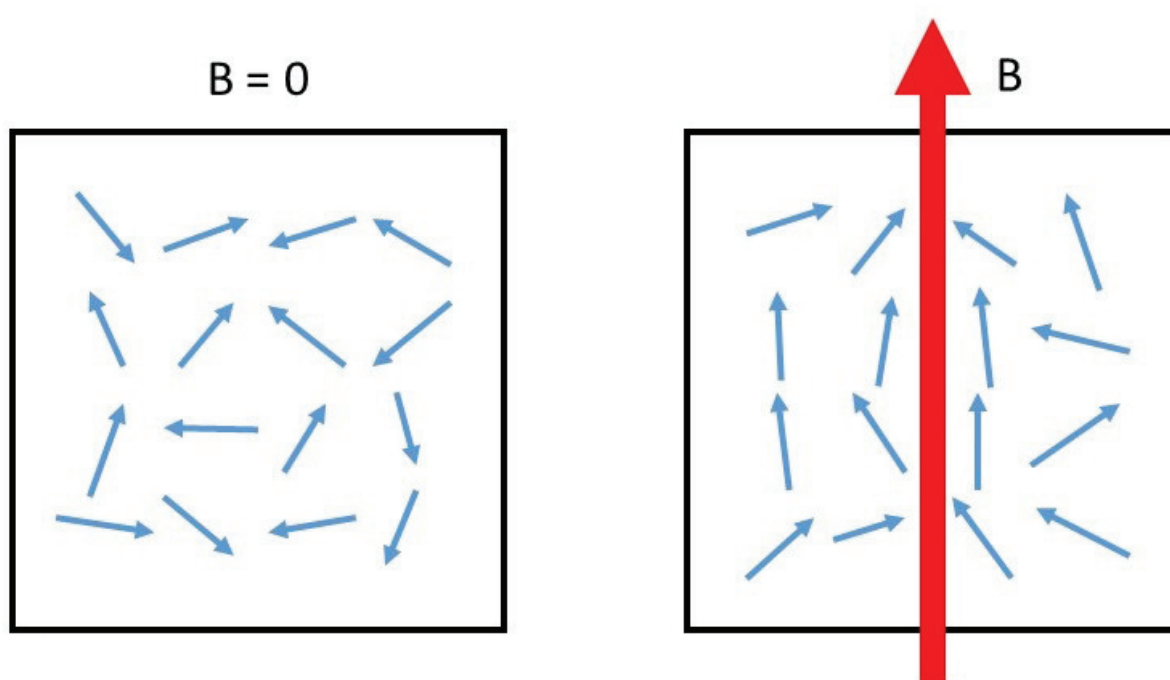


*Figure 2.11: The magnetic moments of a paramagnetic material are randomly oriented without an external field (left panel). If a magnetic field **B** is applied, the magnetic moments start to align with the field depending on the fieldstrength (right panel). If all magnetic moments are perfectly aligned, a saturation state is reached.*

pared to the forces caused by thermal motion. Thermal motion disarranges the ordering of the magnetic moments and is the strongest contribution counteracting the magnetic field. Therefore, the paramagnetic susceptibility is strongly depending on the temperature of the material. The lower the temperature the stronger the effect. The lining up, caused by the external magnetic field, is stronger at low temperatures.

In a paramagnetic material the saturation magnetization $M_S$ is given as

$$M_S = N\mu_{max} \tag{2.27}$$

where $N$ represents the number of atoms per volume and $\mu_{max}$ is the maximum magnetic moment of a single atom. The actual magnetization is given by

$$M = N\langle\boldsymbol{\mu_z}\rangle \tag{2.28}$$

where $\langle\boldsymbol{\mu_z}\rangle$ represents the thermal average magnetic moment in the volume.
In the case of classical physics with $\chi << 1$ and $B \approx \mu_0 H$ we can express the magnetization as

$$M = \frac{N\mu_{eff}^2 B}{3k_B T} \tag{2.29}$$

where $k_B$ is the Boltzmann constant and $T$ the temperature of the material. The ratio between magnetization and saturation magnetization is given by

$$\frac{M}{M_S} = \frac{\langle\mu_Z\rangle}{\mu_{max}} = \frac{\mu_{eff}^2/\mu_{max}B}{3k_B T} \tag{2.30}$$

The paramagnetic susceptibility is now given as

$$\chi = \frac{N\mu_0\mu_{eff}^2}{3k_B T}. \tag{2.31}$$

Using quantum mechanics, there are two possible energy states corresponding to $m_J \pm 1/2$ for a system with spin $= 1/2$. The magnetization, based on the occupation of spin-up and spin-down states, can be expressed as

$$M = N\frac{\mu_B e^{+\mu_B B/kT} - \mu_B e^{-\mu_B B/kT}}{e^{+\mu_B B/kT} + e^{-\mu_B B/kT}} \tag{2.32}$$

which can be written as

$$M = N\mu_B \, tanh\left(\frac{\mu_B B}{k_B T}\right). \tag{2.33}$$

The ratio between magnetization and saturation magnetization is now given as

$$\frac{M}{M_S} = \frac{\langle m_J \rangle}{J} = tanh\left(\frac{g\mu_B J B}{k_B T}\right) \tag{2.34}$$

and for small fields $tanh(x) \approx x$ and the paramagnetic susceptibility can be written as

$$\chi = \frac{N\mu_0\mu_B^2}{k_B T} \tag{2.35}$$

We now consider the general quantum mechanical case where J can have any integer or half integer value. The saturation magnetization is given as

$$M_S = Ng\mu_B J \tag{2.36}$$

and the magnetization is now defined as

$$M = M_s B_J(x) \tag{2.37}$$

where $B_J(x)$ is representing the "Brillouin function" which is defined as

$$B_J(x) = \frac{2J+1}{2J} coth\left(\frac{2J+1}{2J}x\right) - \frac{1}{2J} coth\left(\frac{x}{2J}\right) \tag{2.38}$$

and $x$ is defined as

$$x = \frac{g\mu_B J B}{k_B T}. \tag{2.39}$$

For very low temperatures and high magnetic fields the Brillouin function is approximated as

$$B_J(x) = \frac{(J+1)x}{3J} \tag{2.40}$$

The magnetization is now expressed as:

$$M = Ng\mu_B J\frac{(J+1)x}{3J} = N\frac{g^2\mu_B^2 J(J+1)}{3k_B T}B \tag{2.41}$$

We now define a new constant $\mu_{eff}$ as

$$\mu_{eff} = g\mu_B \sqrt{J(J+1)} \tag{2.42}$$

and get the total magnetization $M$ according to

$$M = N \frac{\mu_{eff}^2}{3k_B T} B \tag{2.43}$$

and with $\chi = \mu_0 M / B$ at low magnetic fields the susceptibility is expressed as

$$\chi = \frac{N\mu_0\mu_{eff}^2}{3k_B T}. \tag{2.44}$$

In the next step the Curie constant $C_{Curie}$ is defined as

$$C_{Curie} = \frac{N\mu_0\mu_{eff}^2}{3k_B} \tag{2.45}$$

and define Curie's law as

$$\chi = \frac{C_{Curie}}{T} \tag{2.46}$$

which describes the temperature dependency of the paramagnetic susceptibility at low magnetic fields. At very high magnetic fields the magnetization saturates and reaches its maximum $M_S$.

## 2.3.5 Interactions of Magnetic Moments

To understand the phenomena of ordered magnetic moments in absence of an external magnetic field, one must understand the different interaction mechanism. In the paramagnetic case the spins can be assumed as independent without any coupling.

A very weak interaction is the classical dipole interaction between two magnetic moments ($\mu_1$ and $\mu_2$) which are separated by a distance $\mathbf{r}$. The energy of the magnetic moments can be expressed as

$$E = \frac{\mu_0}{4\pi r^3} \left[ \mu_1 \cdot \mu_2 - \frac{3}{r^2} (\mu_1 \cdot \mathbf{r})(\mu_2 \cdot \mathbf{r}) \right]. \tag{2.47}$$

For magnetic moments in the range $\mu \approx \mu_B$ and distances $r \approx 1 \mathring{A}$ the energy is in the order of $\sim 10^{-23} J$ and therefore too low to be responsible for the spontaneous magnetic ordering.

In an atomic system with a non vanishing orbital momentum, a spin-orbit interaction is possible. The spin-orbit interaction is the origin of several physical effects such as magnetic crystalline anisotropy and magneto-optical effects (Faraday effect and Kerr effect). The spin-orbit interaction can be expressed in terms of an exchange energy given by

$$E_{spin-orbit} \propto \alpha \frac{\xi}{4\mu_B} \mathbf{S} \cdot \mathbf{L} \tag{2.48}$$

where $\alpha$ is a parameter depending on the structure of the lattice, $\xi$ is the interaction strength, $\mathbf{S}$ the spin momentum and $\mathbf{L}$ the orbital momentum. The magnetization can be orientation dependent and anisotropic based on the spin-orbit interaction. In typical solid state materials, the orbital momentum is quenched (L = 0).

The strongest interaction mechanism is the exchange interaction which is the fundamental quantum mechanical effect describing the spontaneous magnetic ordering. The exchange interaction is based on the interaction of spins through their Coulomb potential and the antisymmetric wave functions of the changing spins described by the Pauli exclusion principle. The exchange interaction is a pure quantum mechanical effect and is described by the "Heisenberg-Hamiltonian" given as

$$\mathcal{H} = -\sum_{ij} J_{ij} \mathbf{S}_i \cdot \mathbf{S}_j \tag{2.49}$$

where $J_{ij}$ represents the exchange integral between the $i^{th}$ and the $j^{th}$ spin. $\mathbf{S}_i$ and $\mathbf{S}_j$ are representing spin vectors. This interaction is responsible for the spontaneous magnetization and the ferromagnetic ordering.

The exchange integral $J_{ij}$ can be a very complex parameter depending of the different exchange processes, such as indirect exchange, direct exchange, double exchange or asymmetric exchange. In the case of an external magnetic field, the total energy can be represented as:

$$\mathcal{H} = -\sum_{ij} J_{ij} \mathbf{S}_i \cdot \mathbf{S}_j - \sum g\mu_B \mathbf{S}_i \cdot \mathbf{B} \tag{2.50}$$

Using the mean field approximation theory the spin vectors $\mathbf{S}_i$ and $\mathbf{S}_j$ can be replaced by their thermal average $\langle \mathbf{S}_i \rangle$ and $\langle \mathbf{S}_j \rangle$ and equation 2.50 can be expressed as

$$\mathcal{H} = -\sum_i \mathbf{S}_i \cdot \left( g\mu_B \mathbf{B} + 2\sum_j J_{ij}\langle \mathbf{S}_j \rangle \right) - \sum_{ij} \langle \mathbf{S}_i \rangle \cdot \langle \mathbf{S}_j \rangle \tag{2.51}$$

which represents the contribution of the exchange interaction in addition to the Zeeman term in an external field. The mean field approximation theory neglects the quadratic thermal fluctuations $(S_i - \langle S_i \rangle)^2$ of the spins.

## 2.3.6 Ferromagnetism

The strongest spontaneous magnetic ordering is the ferromagnetism. In ferromagnetic materials, there are aligned magnetic moments without an external field caused by the exchange interaction of the spins. A ferromagnetic material in an external magnetic field can be expressed with a hamiltonian given as

$$\mathcal{H} = -\sum_{ij} J_{ij}\mathbf{S}_i \cdot \mathbf{S}_j + g\mu_B \sum_j \mathbf{S}_j \cdot \mathbf{B} \tag{2.52}$$

with a positive exchange integral. The mean field theory states that there is a magnetic field, called exchanged field $\mathbf{B}_{exchange}$, which is proportional to the magnetization and acting on each atom. The relationship between the exchange field and the magnetization is given as:

$$\mathbf{B}_{exchange} = \lambda \mathbf{M} \tag{2.53}$$

The magnetic susceptibility of a ferromagnetic material can be expressed according to the "Curie-Weiß-law" as

$$\chi = \frac{C}{T - C\lambda} = \frac{C}{T - T_C} \tag{2.54}$$

where $T_C$ represents the Curie temperature which is defined as

$$T_C = \frac{N\lambda\mu_{eff}^2}{3k_B} \tag{2.55}$$

where $\lambda$ is a constant representing the strength of the molecular field which represents the ordering of the system.

The spontaneous magnetization of ferromagnetic materials is disturbed with increasing temperature and breaks down when the temperature is above the Curie temperature. At the temperature $T = C\lambda$ the susceptibility has a singularity. There is an approximation between the exchange integral and the Curie temperature which is given as

$$J = \frac{3k_B T_C}{2zS(S+1)} \tag{2.56}$$

where $z$ represents the number of neighbouring atoms.

For temperatures $T < T_C$ there is a spontaneous magnetic moment which is shifting with
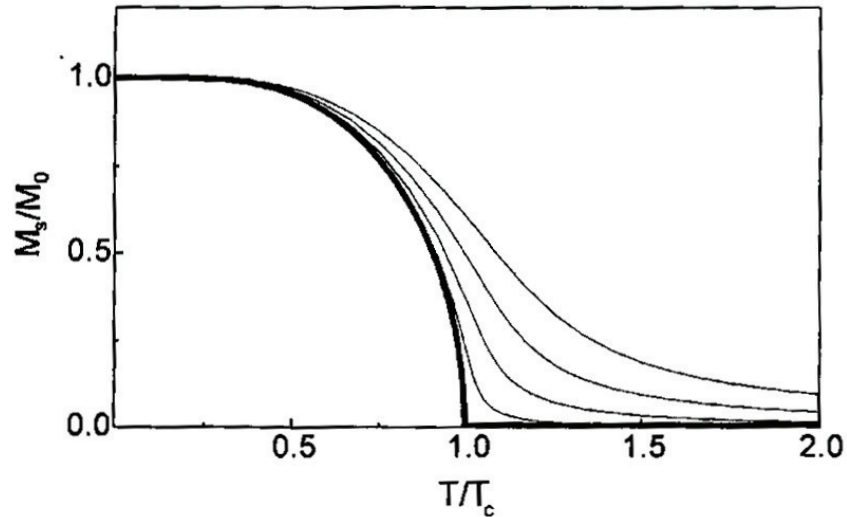


*Figure 2.12: The magnetization of a ferromagnetic material depending on the temperature at varying field strengths. Figure by courtesy of Prof. Heinz Krenn.*

increasing temperature. Above the Curie temperature $T > T_C$ the spontaneous magnetization is vanishing and the symmetry of the system is broken. In general, ferromagnetic materials can have extremely high susceptibility values.

## 2.3.7 Antiferromagnetism

In nature, the most common magnetic ordering is the antiferromagnetism. A simple antiferromagnet consists of two antiparallel ferromagnetic sublattices, where each magnetic moment has an antiparallel neighbour. The exchange integral $\mathbf{J}_{ij}$ is negative, indicating

a antiferromagnetic ordering. Based on the mean field approximation, the hamiltonian for each sublattice can be expressed as

$$\mathcal{H}_1 = g\mu_B \mathbf{B} + 2p_1 \mathbf{J}_1 \langle S_1 \rangle + 2p_2 \mathbf{J}_2 \langle S_2 \rangle \tag{2.57}$$

$$\mathcal{H}_1 = g\mu_B \mathbf{B} + 2p_1 \mathbf{J}_1 \langle S_1 \rangle + 2p_2 \mathbf{J}_2 \langle S_2 \rangle \tag{2.58}$$

where $p_1$ the number of parallel neighbouring spins and $p_2$ the number of antiparallel neighbouring spins. The constants $p$ are depending on the crystal structure of the system. For a simple antiferromagnet with two sublattices the exchange integrals are given as $J_1 = 0$ and $J_2 < 0$. As compared to a ferromagnet, there is a distinct ordering temperature for the antiferromagnet which is represented by the "Neel temperature". This is similar to the "Curie temperature" of ferromagnets. The Neel temperature is defined as

$$T_N = \frac{2S(S+1)}{3k_B} \sum_{j=1}^{p_2} (-\mathbf{J}_{ij}) \tag{2.59}$$

alternatively the Neel temperature can be expressed in terms of $\mu_{eff}$ as:

$$T_N = \frac{N\lambda\mu_{eff}^2}{3k_B} \tag{2.60}$$

The magnetic susceptibility of an antiferromagnet can be expressed using the "Curie-Weiß-law" as given by

$$\chi = \frac{2C}{T + T_N} \tag{2.61}$$

At temperatures below the ordering Neel temperature, the total magnetic moment is vanishing due to the antiparallel ordering of the spins. Above the Neel temperature this symmetry is broken. The Curie-Weiß-law is valid for ferromagnets at temperatures $T > T_C$ and for antiferromagnets for temperatures $T > T_N$.
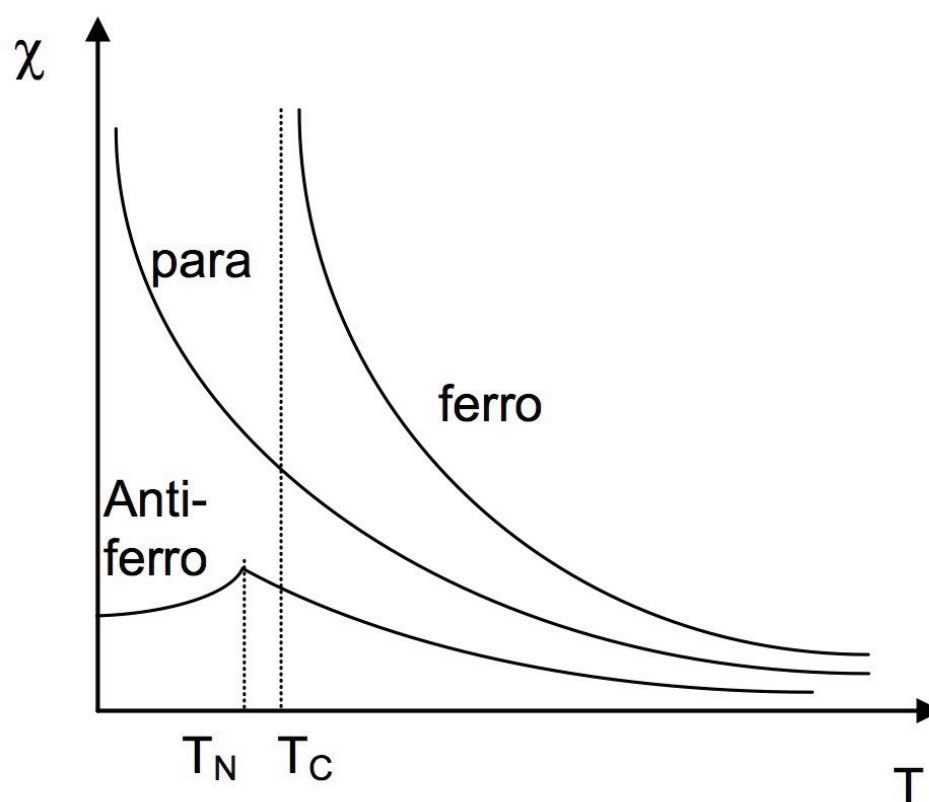
*Figure 2.13: The temperature dependency of a paramagnetic, ferromagnetic and antiferromagnetic material with their corresponding ordering temperature. Figure by courtesy of Prof. Heinz Krenn.*

## 2.3.8 Ferrimagnetism

In the case of an antiferromagnetic ordering, it is assumed that the two sublattice are equal and cancel each other. In a ferrimagnetic material, this is not the case. There, the two sublattice possess different properties based on the crystal structure of the ferrimagnetic material. We will describe the concept of ferrimagnetism based on the properties of magnetite ($Fe_3O_4$ or $FeOFe_2O_3$), which is a prominent ferrimagnet and present in different biological tissue.

Magnetite consists of $Fe^{3+}$ ions with spin S = 5/2 and of $Fe^{2+}$ ions with spin S = 2. One would expect that both ion varieties contribute, corresponding to their spin, to the total magnetization. In an ideal case this would be $14\mu_B$ but experimentally only approximately $4.1\mu_B$ are observed. The reason for this behaviour is that the $Fe^{3+}$ ions are aligned antiparallell and do not contribute to the total magnetic moment. In the case

of magnetite, the magnetic moment is driven by the contribution of $Fe^{2+}$ leading to a ferrimagnetic ordering.

In the case of two different spin sublattice **A** and **B**, exchange interactions occur, which
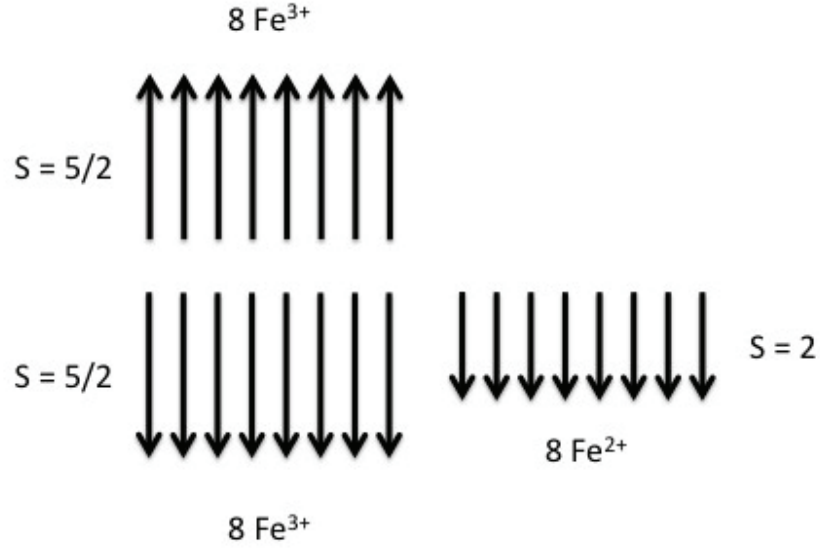


*Figure 2.14: Configuration of $Fe^{3+}$ and $Fe^{2+}$ spin moments of magnetite.*

are described by an exchange field of each sublattice and given as

$$\mathbf{B}_A = -\lambda \mathbf{M}_A - \mu \mathbf{M}_B \tag{2.62}$$

and

$$\mathbf{B}_B = -\mu \mathbf{M}_A - \nu \mathbf{M}_B \tag{2.63}$$

where $\lambda$, $\mu$ and $\nu$ are constants and the exchange energy can be expressed as

$$E = -\frac{1}{2} \left( \mathbf{B}_A \cdot \mathbf{M}_A + \mathbf{B}_B \cdot \mathbf{M}_B \right). \tag{2.64}$$

The energy has its minimum when both magnetic moments are antiparallel aligned ($\mathbf{M}_A = \mathbf{M}_B = 0$) and its maximum when $\mathbf{M}_A$ and $\mathbf{M}_B$ are parallel aligned.

Two different Curie temperatures, $C_A$ and $C_B$, are defined for the two spin sublattice. Only antiparallel exchange effects between A and B are assumed. Again, the mean field

approximation is used to get

$$M_A T = C_A(\mathbf{B} - \mu M_B) \tag{2.65}$$

and

$$M_B T = C_B(\mathbf{B} - \mu M_A) \tag{2.66}$$

thus one can define the ferrimagnetic susceptibility for temperatures $T > T_C$ as

$$\chi = \frac{(C_A + C_B)T - 2\mu C_A C_B}{T^2 - T_C^2} \tag{2.67}$$

where the ferrimagnetic Curie temperature is defined as $T_C = \mu(C_A C_B)^{1/2}$.
The magnetic susceptibility of a ferrimagnet is depending on the crystal structure and the interactions between the different spin sublattice in the structure.

## 2.4 Effects of Iron in MRI

Biological tissue is highly diamagnetic based on its high water content. The susceptibility is approximately in the range of $\pm 10\% - 20\%$ of the susceptibility of water. This leads to an overall diamagnetic susceptibility in the range of $-11 \times 10^{-6} < \chi_{tissue} < -7 \times 10^{-6}$ [82]. The strong diamagnetic background susceptibility of the tissue structure can additionally be influenced by diamagnetic contributions of $Na^+$, $K^+$ and $C^-$ or paramagnetic contributions of $O_2$ or iron ($Fe^{2+}$, $Fe^{3+}$). The mean iron concentration in the whole human brain is approximately 1-2 mg in total and the highest iron concentrations are found in the substantia nigra with approximately $210.3 \pm 74.6$ mg/kg [83]. Iron itself is highly paramagnetic, but the concentrations in the different brain regions are too low to change the total susceptibility from diamagnetic to paramagnetic.

The effect of iron in MRI was first observed as loss of signal, in $T_2$ weighted images, in areas with high iron content [19]. This so called $T_2$ hypointensitiy is linked to a decrease of the $T_2$ relaxation time caused by microscopic magnetic fields induced by the iron particles. The effect of iron particles on the MR signal is even stronger in gradient echo sequences (GRE) where the decay of the transversal magnetization is described in terms of $T_2^*$ relaxation time.

The effect of magnetical particles, such as iron, inside tissue is modeled using an *outer sphere approach* where the particles are magnetized through an external magnetic field $B_0$ and therefore induce a microscopic magnetic field which superimposes with the external magnetic field [19, 84, 85].

The total magnetic field of the sample can be expressed as the sum of the external field $B_0$ and an additional term $\Delta B$ representing the field inhomogeneities caused by magnetic particles and/or imperfect magnetic fields. The total magnetic field is given as

$$B = B_0 + \Delta B \tag{2.68}$$

and if the additional contributions of the spatial encoding are included we can extend equation 2.68 to

$$B(r) = B_0 + G_x \cdot x + G_y \cdot y + G_z \cdot z + \Delta B_0(r) \tag{2.69}$$

where $G_x$, $G_y$ and $G_z$ are the additional gradient fields. The field inhomogeneities are now depending on the location. Therefore, the corresponding Larmor frequency is changed based on the strength of the field inhomogeneities $\Delta B(x, y, z)$ and is given as

$$\omega(r) = -\gamma B(r). \tag{2.70}$$

The magnetic field inhomogeneities can origin from (i) macroscopic field inhomogeneities, typically larger than the voxel size, and (ii) mesoscopic field inhomogeneities, typically smaller than the voxel size [86]. Macroscopic field inhomogenities are caused by imperfect $B_0$ shimming, large susceptibility shifts at air-tissue interfaces or ferromagnetic objects, such as implants. Mesoscopic field inhomogeneities arise from susceptibility differences between different tissue structures inside a voxel or small paramagnetic inclusions, such as iron. The mesoscopic field inhomogeneities provide valuable information about the microstructure and properties of biological tissue and is reflected in the $T_2^*$ relaxation time. Thus, $T_2^*$ is sensitive to contributions of iron, myelination or calcifications inside tissue [87].

To distinguish the different field inhomogeneities we consider a homogeneous voxel of tissue inside a magnetic field $B$ without perturbation of the magnetic field as shown in figure 2.15 (a). In a second step we consider an inhomogeneous voxel, including an iron particle, leading to a field perturbation as shown in figure 2.15 (b). The contribution $\Delta B$ is depending on the shape and the magnetic properties of the object inside the voxel. For a spherical object with radius $a$ one can express the field perturbation inside the object and along the $z$ direction of the magnetic field as

$$\Delta B_z = \frac{2}{3}\Delta\chi B_0 \tag{2.71}$$

and outside the object as

$$\Delta B_z = \frac{\Delta\chi B_0 a^3}{3}\frac{(2z^2 - x^2 - y^2)}{(x^2 + y^2 + z^2)^{5/2}}. \tag{2.72}$$

The magnetic field lines of a sphere are shown in figure 2.16.

The time dependent MR signal can be expressed as

$$S(t) = S(0) \cdot e^{-t/T_2} \cdot e^{j\varphi} \tag{2.73}$$
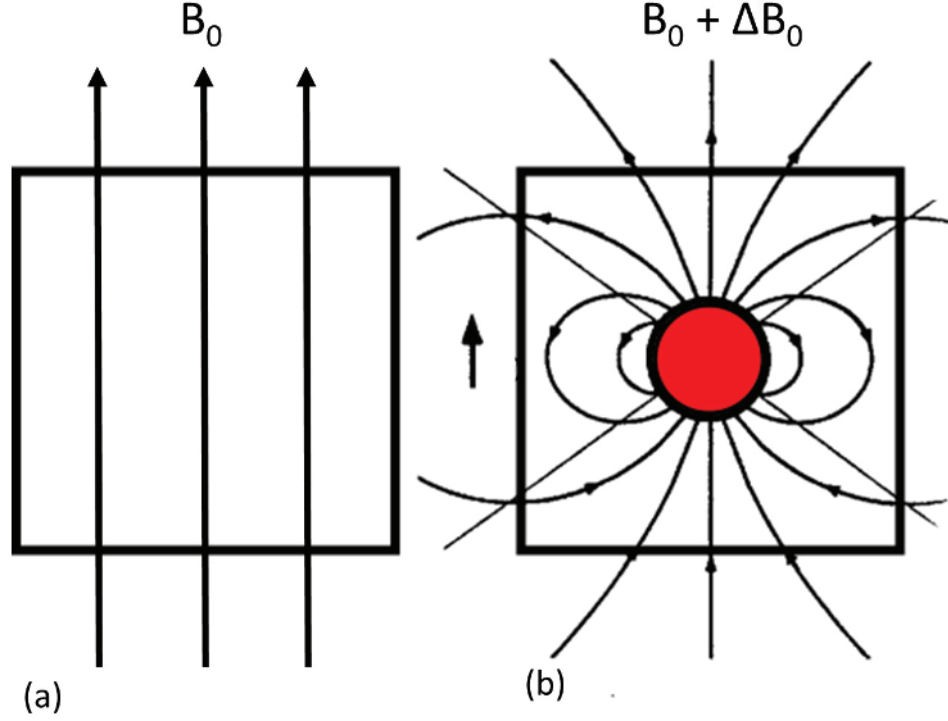
*Figure 2.15: A homogeneous voxel of tissue (a) and inhomogeneous voxel of tissue with iron particles (b). The iron particles produce a field perturbation affecting the total magnetic field of the voxel.*

where $S(0)$ is the initial signal and $\varphi$ the phase of the MR signal. The phase in MRI is expressed as

$$\varphi = -\gamma \cdot \Delta B \cdot t \tag{2.74}$$

where t represents the time and is usually replaced by the discrete echo time TE.

The equilibrium longitudinal magnetization ($M_0$) for a system with spin $= 1/2$ and a total number of N spins is given as

$$M_0 = \frac{N\gamma^2\hbar^2 B_0}{4k_B T} \tag{2.75}$$

with $\gamma$ the gyromagnetic ratio, $\hbar$ the Planck's constant divided by $2\pi$, $k_B$ the Boltzmann's constant and $T$ the temperature. The time dependent change of the magnetization in MRI
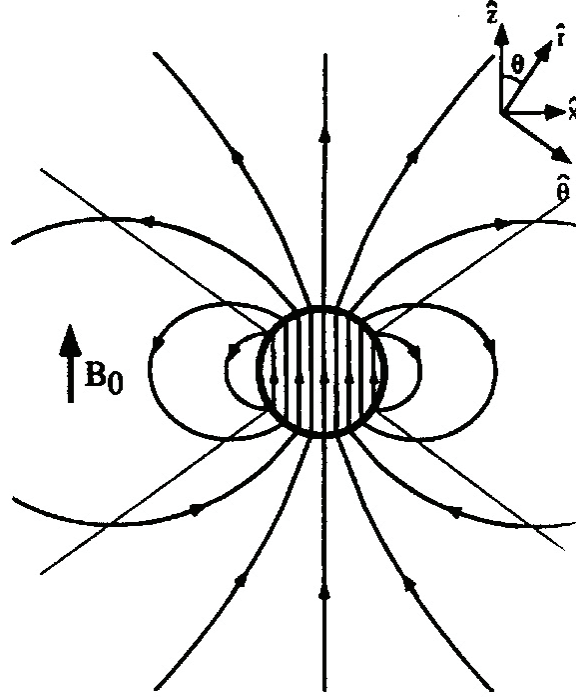
*Figure 2.16: The magnetic field lines of a uniformly magnetized sphere inside a magnetic field $B_0$.*
*Adapted from [82].*

in presence of relaxation mechanisms is described by the Bloch equations [6].

$$\frac{d\mathbf{M}}{dt} = \gamma \left( \mathbf{M} \times \mathbf{B} \right) - \frac{M_x}{T_2} - \frac{M_y}{T_2} + \frac{(M_0 - M_z)}{T_1} \tag{2.76}$$

After the system is excited by a RF pulse, the transversal magnetization $M_{xy} = M_x - jM_y$ is given as

$$M_{xy}(t) = M_{xy}(0) \cdot e^{-t/T_2} \int_r e^{j\gamma \Delta B(r)t} dr = M_{xy}(0) \cdot e^{-t/T_2^*} \tag{2.77}$$

where $\Delta B_0(r)$ represents the local field inhomogeneities and $T_2^*$ is the effective transversal relaxation time in a gradient echo sequence. For a spin echo sequence (SE), the spin dephasing caused by the field inhomogeneities are refocused with the 180° pulse and the integral in equation 2.77 is getting equal one. This leads to

$$M_{xy} = M_{xy}(0) \cdot e^{-t/T_2} \tag{2.78}$$

where $T_2$ represents the irreversible transversal relaxation time. Therefore we can express $1/T_2^*$ as

$$\frac{1}{T_2^*} = \frac{1}{T_2} + \frac{1}{T_2'} \tag{2.79}$$

with $T_2^*$ the effective, $T_2$ the irreversible and $T_2'$ the reversible transversal relaxation time. In terms or relaxation rates equation 2.79 can be written as

$$R_2^* = R_2 + R_2' \tag{2.80}$$

and extended to

$$R_2^* = R_2 + \gamma \Delta B. \tag{2.81}$$

A magnetic object inside a voxel is causing a preturbation of the magnetic field which is leading to a change of the magnitude and phase of the MR signal as expressed in the equations above. The field inhomogeneities cause an additional contribution to the dephasing of the spins, resulting in a reduced transversal relaxation which is sensed by a hydrogen proton close to an iron particle as shown in figure 2.17.

Langkammer et al. [32] reported the counteracting contributions of iron and myelin on the total magnetic susceptibility of brain tissue. Especially in white matter, there is a strong contribution of myelin. Thus, a reliable iron quantification is not always possible. Compared to the susceptibility, iron and myelin are affecting $R_2^*$ in the same direction as shown in figure 2.18. The influence of iron and myelin to the total $R_2^*$ relaxation rate is inseparable.

## 2.5 Methods for Iron Mapping

The concentration of iron in the human brain is high enough to effect the MR signal. It is suggested that ferritin and hemosiderin are the two major components affecting the MR signal. The concentration of transferrin and other minor iron compounds are to low to influence the MR signal [19, 20].
The paramagnetic susceptibility of iron and its influence on relaxation mechanisms enables MRI as suitable tool to assess iron. Several techniques to assess iron based on relaxation
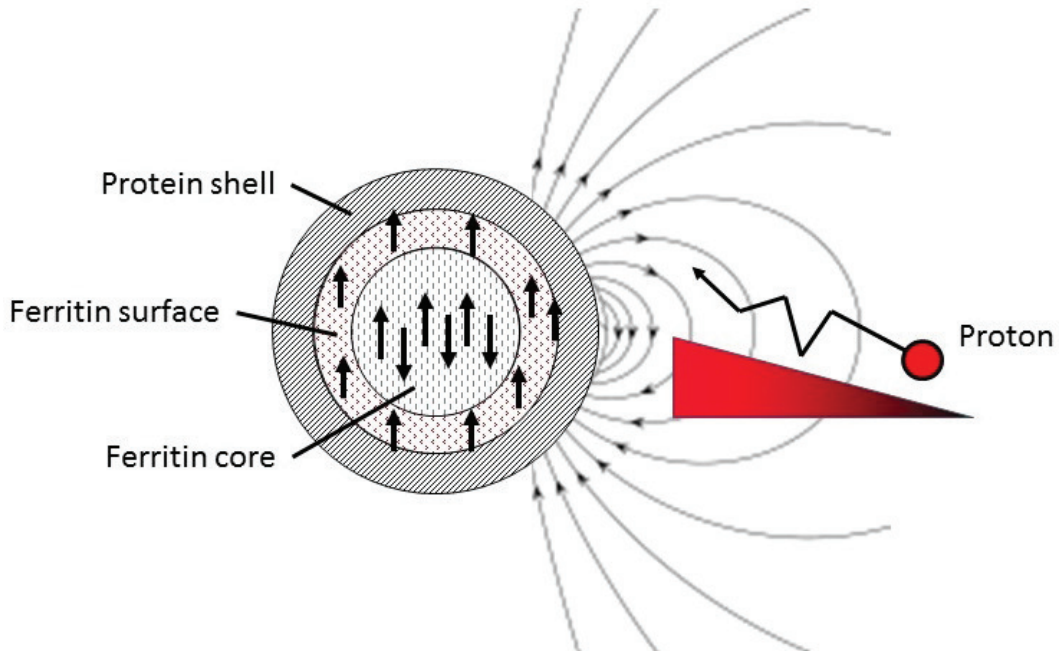
*Figure 2.17: A ferritin molecule, with the proton shell, and the ferrihydrite, consisting of a shell layer and core layer, is producing a field perturbation which is sensed by the proton close to the ferritin.*

time mapping [20–22], phase imaging [23,24], magnetic field correlation [25,26], direct saturation imaging [27] and quantitative susceptibility mapping (QSM) [28–30] are described in literature. A possible implementation of these techniques is given in neurological diseases involving disturbed iron metabolism, such as MS [31].

The most promising approaches are quantitative relaxation time mapping $T_1$, $T_2$ and $T_2^*$ and phase imaging, such as quantitative susceptibility mapping (QSM) [31].

## 2.5.1 Relaxation Time Mapping

### Longitudinal Relaxation Time T1

The time dependent magnetization in presence of relaxation effects is described by the Bloch equations [6], as stated in equation 2.76. The longitudinal equilibrium magnetization $M_0$ (equation 2.75) is excited by a time dependent RF pulse into the transversal plane. The recovery of the longitudinal magnetization is characterized by the $T_1$ relaxation time. The decay of the transversal magnetization is characterized by the $T_2$ relaxation time.
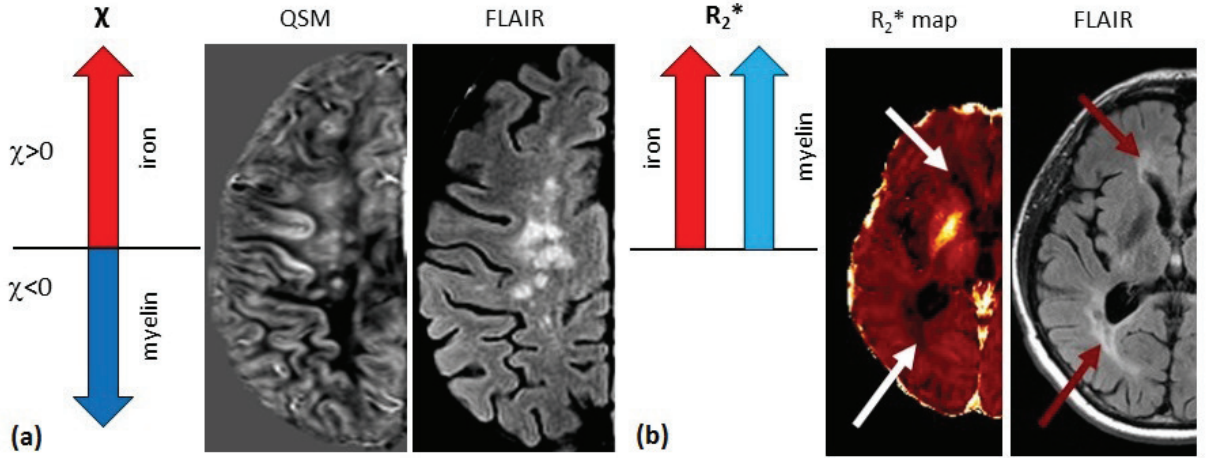
*Figure 2.18: Iron and myelin are counteracting in QSM (a) and summing up in $R_2^*$ (b). In demyelinated WM lesions, as indicated by the FLAIR images, a suitable assessment of iron using QSM or $R_2^*$ is not possible.*

The $T_1$ relaxation is based on the energy exchange between the excited spins and the surrounding lattice described by dipolar interactions [85]. The rate at which the energy is transferred from the spin to the lattice is described by the correlation time $\tau_c$. The correlation time is depending on the size of the molecules and the diffusion constant. The $T_1$ relaxation time of brain tissue is strongly depending on the water content [88] and the molecular structure [89]. Myelin and iron are affecting the $T_1$ relaxation time leading to the prominent contrast between WM and GM in the human brain [90].

Iron depositions reduce the $T_1$ relaxation time, and its inverse $R_1$ is linearly depending on the iron concentration over the whole physiological range [21].

Several methods to calculate the $T_1$ relaxation time, based on inversion recovery (IR) or saturation recovery (SR) are proposed in the literature [91]. The gold standard to calculate $T_1$ is a series of IR sequences with different inversion times (TI). In an IR sequence, the longitudinal magnetization $M_0$ is inverted by a 180° pulse and after a specific time, defined by TI, the MR signal is measured. Images with a different weighting can be generated to calculate $T_1$ based on

$$S(TI) = M_0 \cdot \left(1 - a \cdot e^{-TI/T_1}\right) \tag{2.82}$$

where $a$ is a factor and equal two, in case of perfect inversion behaviour.
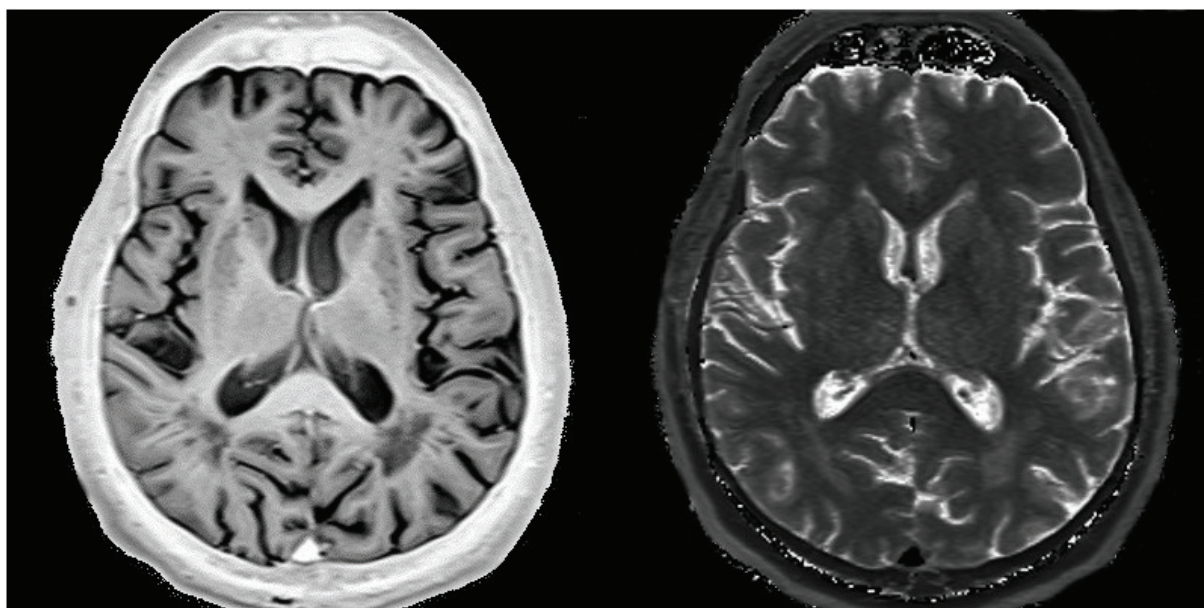
*Figure 2.19: A $T_1$ weighted image (left) and the corresponding quantitative $T_1$ map (right) of a 67 year old male patient.*

**Transverse Relaxation Time T2**

The transverse relaxation time $T_2$ characterizes the decay of the transverse magnetization after RF excitation. The physical mechanism behind the magnetization decay are based on spin-spin interactions. Due to random and time dependent fluctuations in the magnetic field, different spins may have a slightly different precession frequency leading to a dephasing of the spins [85]. The loss of coherence through the dephasing spins is leading to a reduction of the $T_2$ relaxation time. The presence of iron accumulations, cause additional field gradients and contribute to the dephasing and reduction of $T_2$. The influence of iron on $T_2$ is observed as hypointensity on $T_2$ weighted images [92]. The reduction of $T_2$ in presence of iron is even stronger at higher field strengths [93]. $R_2$, the inverse of $T_2$, correlates linearly with the iron content of gray matter [22, 94].

$T_2$ is usually obtained using a spin echo (SE) based sequence with multiple echo times to fit a mono exponential decay according to

$$S(TE) = M_0 \cdot e^{-TE/T_2} \tag{2.83}$$

with typically 16 to 32 echos [95]. Further, $T_2$ can be estimated using an early $(TE_1)$ and late $(TE_2)$ echo according to

$$T_2 = \frac{TE_2 - TE_1}{ln\left(\frac{S(TE_1)}{S(TE_2)}\right)} \tag{2.84}$$

where $S(TE_1)$ is the signal intensity of the first echo and $S(TE_2)$ the signal intensity of the second echo [96]. The two above described approaches assume a single $T_2$ component. This is usually not the case in the human brain, where different $T_2$ components were observed [97]. The multiple $T_2$ components are associated with myelin water, which is trapped inside the myelin sheaths, as well as extracellular water and intracellular water. The multiple water components are leading to a multi exponential decay of $T_2$ [98–101]. So, the relationship between $T_2$ and iron in white matter is confounded by the effects of myelin and the different water compartments. A precise estimation of $T_2$ or multiple $T_2$ components is still a challenging task and topic for further research.
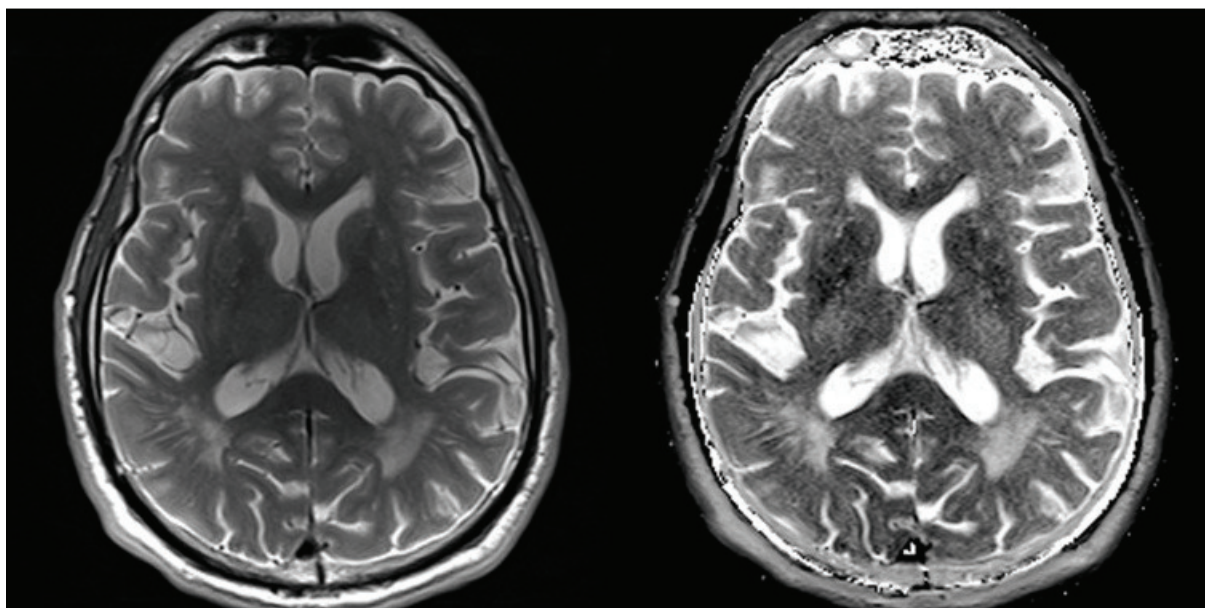


*Figure 2.20: A $T_2$ weighted image (left) and the corresponding quantitative $T_2$ map (right) of a 67 year old male patient.*

**Effective Transverse Relaxation Time T2\***

In contrast to $T_2$, $T_2^*$ reflects the effective transverse relaxation time due all kind of perturbations affecting the spin dephasing. While in a spin echo sequence the 180° pulse

is refocusing the non-random dephasing effects, this is not possible using gradient echo sequences. The influence of diffusion, spectral broadening, multiple water compartments and field inhomogeneities additionally contribute to the dephasing leading to an effective transverse relaxation time $T_2^*$ [87]. The relation between $T_2$ and $T_2^*$ is given as

$$\frac{1}{T_2^*} = \frac{1}{T_2} + \frac{1}{T_2'}. \tag{2.85}$$

The effective transverse relaxation rate $R_2^*$ ( $= 1/T_2*$) can be expressed as sum of an irreversible ($R_2$) and reversible ($R_2'$) transverse relaxation rate [86]. $R_2$ is representing the intrinsic tissue properties and $R_2'$ is representing microscopic field variations. These field variations are caused by paramagnetic contributions, such as iron, and to a lesser part by other tissue components whit a distinct susceptibility.

The relationship between $R_2^*$ and iron [19] can be expressed as

$$R_2^* = \frac{1}{T_2^*} = R_2^{*0} + \alpha^*[Fe] \tag{2.86}$$

where [Fe] represents the iron concentration. The iron concentration can be estimated using age matched literature data of Hallgren and Sourander [48] or assessed in a post-mortem set-up by biomedical analysis, such as mass spectrometry [83]. A post-mortem study by Langkammer et al. [22] showed a linear correlation over the entire range of iron concentrations, valid for gray matter structures. The contribution of myelin to $R_2^*$ is disturbing iron quantification based on $R_2^*$ in brain regions like WM [32].

Assuming a mono-exponential model, $R_2^*$ can be calculated based on $T_2^*$ weighted images acquired at different echo times, using a gradient echo sequence (GRE). The signal at the echo time TE is represented as

$$S(TE) = S_0 \cdot exp\left(\frac{-TE}{T_2^*}\right) \tag{2.87}$$

where $S_0$ is the initial signal at zero echo time. The gradient echo signal is effected by several factors, such as the slice profile, $B_0$ inhomogeneities, stimulated echoes. To correct for this influences the signal equation is extended to

$$S(TE) = S_0 \cdot exp\left(\frac{-TE}{T_2^*}\right) \cdot |sinc\left(\frac{\gamma \cdot G \cdot \Delta z \cdot TE}{2}\right)| \tag{2.88}$$

where $\gamma$ is the gyromagnetic ratio, G is the gradient strength and $\Delta z$ is the field gradient in z direction [102, 103]. The correction of the mono-exponential decay term can be extended to all three directions [104].

The gradient field along the z direction $\Delta B_z = G \cdot \Delta z$ can be estimated by several approaches such as iterative approaches based on a mono-exponential assumption [105, 106] or a direct fit of the phase versus echo time [107].

The influence of different water compartments, such as myelin water, intracellular or extracellular water, inside a voxel causes a multi exponential decay of $T_2^*$ [99]. The estimation of the multiple components is based on

$$S(TE) = A_{my} \cdot e^{-TE/T_{2,my}^*} + A_{ma} \cdot e^{-TE/T_{2,ma}^*} + A_{mx} \cdot e^{-TE/T_{2,mx}^*} + A_{bl} \tag{2.89}$$

where $my$ represents the myelin water, $ma$ the axonal water, $mx$ the mixed water pool. The factor $A_{my}$, $A_{ma}$ and $A_{mx}$ represents the amplitude of corresponding water component and $A_{bl}$ the residual base line signal [108]. The multi-exponential model is complex in acquisition and data processing, thus a mono-exponential model is preferred. The multi-exponential model is suitable to improve $R_2^*$ as myelin dependent marker through calculation of specific myelin water components.

Previous studies showed the suitability of $T_2^*$ magnitude and phase as potential marker for white and gray matter microstructure, depending on size, density and orientation of the myelinated fibres in respect to the magnetic field [109–113].

In case of $R_2^*$ as iron marker, no additional benefit is given by the multi-exponential model. $R_2^*$ is a suitable iron marker limited to gray matter structures. This allows a quantitative assessment of gray matter iron content in neurological diseases such as MS [17, 70, 71, 114].

## 2.5.2 Quantitative Susceptibility Mapping (QSM)

In human brain tissue, iron, myelin, calcium and lipids [20, 109] are the major contributions to MRI phase contrast. Quantitative susceptibility mapping (QSM) is a novel and promising technique to assess new insights into microstructure and properties of biological tissue [30, 116]. The relationship between phase and susceptibility is expressed as:

$$\varphi(x, y, z) = -\gamma \cdot B_0 TE \cdot FT^{-1} \left( \frac{1}{3} - \frac{k_z^2}{K^2} \right) \otimes \chi(x, y, z) \tag{2.90}$$
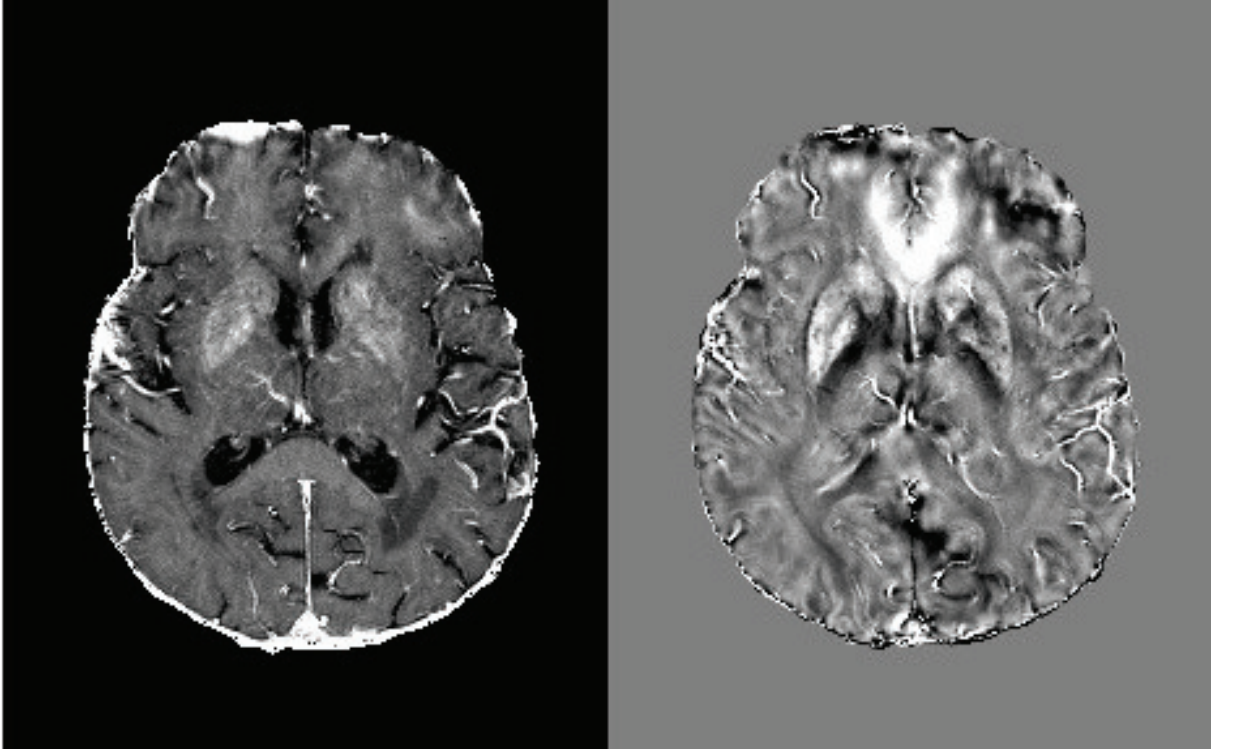
*Figure 2.21: A $R_2^*$ map (left) and QSM map (right) of a 67 year old male patient. The $R_2^*$ map was calculated using a mono-exponential model and the QSM map was calculated according to Langkammer et al [115].*

The convolution of the susceptibility is replaced by a multiplication of the Fourier transformed susceptibility. Thus, equation 2.90 is given as

$$\varphi(x,y,z) = -\gamma \cdot B_0 TE \cdot FT^{-1} \left( \frac{1}{3} - \frac{k_z^2}{K^2} \right) \cdot FT\left( \chi(x,y,z) \right) \tag{2.91}$$

where $\chi$ is the magnetic susceptibility, $B_0$ the field strength, $TE$ the echo time, and $FT$ represents the Fourier transformation and $FT^{-1}$ the inverse Fourier transformation. $K^2$ is representing the magnitude of the k-space vector and $k_z$ its z component [117–119]. To calculate the magnetic susceptibility, equation 2.91 is inverted to

$$\chi(x,y,z) = FT^{-1} \left[ FT \left( \frac{\varphi(x,y,z)}{-\gamma \cdot B_0 \cdot TE} \right) \cdot \right] \tag{2.92}$$

where $F$ denotes the convolution kernel given as

$$F = \frac{1}{\frac{1}{3} - \frac{k_z^2}{K^2}}. \tag{2.93}$$

The inversion from phase to susceptibility, is leading to an ill-posed inverse problem. There is a zero value of the kernel function $F$ at an angle of 54.7° in respect to $k_z$. A simple kernel division and the use of a truncation level will avoid zero values in the kernel, but it is leading to streaking artefacts and noise amplification in the susceptibility estimation [119].

There are several basic steps for the calculation of susceptibility maps [30, 116]:

- Phase reconstruction of multi channel data
  Phase images obtained from multi-channel coils possess different phase offsets based on the coil sensitivity. This may cause an imperfect combination of the complex phase signal to a combined phase image. Imperfect phase combination results in open ended fringe lines or signal cancellation which can not be corrected using phase unwrapping techniques. Several approaches for phase combination are described in literature [23, 120–122].

- Phase unwrapping
  In the original phase image, phase wraps occur, because MRI phase is represented in the range of $-\pi$ to $\pi$ which means unwrapping is needed [123, 124]. Several QSM algorithms use the Laplacian of the phase for background field removal, thus no prior phase unwrapping is needed [115, 125]. Imperfections in phase unwrapping will effect the background field removal and the result of the QSM calculation [116].

- Generation of brain masks
  The generation of a brain mask is an important step for background field removal. Regions with artefacts and unreliable phase information are excluded in the mask to avoid false susceptibility estimation. Typically brain masks are generated with tools, such as the Brain Extraction Tool (BET) of the FSL software package [126].

- Background Field Removal
  The field inhomogeneities, sensed with phase images, are separated into local and background field. Thus the total field inhomogeneities are given as

$$\Delta B_z = \Delta B_{local} + \Delta B_{background}. \tag{2.94}$$

The background field $\Delta B_{background}$ is produced by susceptibility shifts at air-tissue interfaces and global magnetic field inhomogeneities. The local field $\Delta B_{local}$ is generated by the local tissue susceptibility distribution, in which we are interested in QSM. To remove the background field, high pass filter [127], geometry dependent artifact correction [128], dipole fitting [129] or special methods such as Sophisticated Harmonic Artifact Reduction for Phase data (SHARP) [130] have been used.

- Solving the ill-posed inverse problem
  Over the last decade, several approaches to solve the ill-posed inverse problem and calculate the susceptibility distribution are proposed in literature and summarized in recent review articles [30,116]. By solving the ill-posed inverse problem, as stated in equation 2.92, the susceptibility distribution $\Delta\chi(x, y, z)$ can be obtained. Different approaches such as truncation and division of the k-space kernel [119], incorporating information of multiple angle acquisition [131], the use of a priori information, gained in magnitude images [132] or several other high sophisticated approaches [115,133] are possible.

Calculating QSM based on acquisition of phase images with different orientation of the object in respect to the main magnetic field is called calculation of susceptibility through multiple orientation sampling (COSMOS). Through information acquired at multiple angles, the inverse problem is getting over-determined and can be solved [131]. This technique is preferred for post-mortem MRI, because of the possibility to rotate the object almost without restriction in the magnetic field. Therefore, an over determination of the ill-posed problem is easily achieved. Another advantage is the increased SNR, compared to single orientation approaches. The multi-orientation acquisition is a time consuming approach and the rotation of the patients head is not always possible. Thus, single angle approaches are preferred for in vivo imaging.

## 2.6 Post-mortem MRI

An ideal post-mortem MRI experiment would produced "life-like" image contrast close to *in vivo* conditions. In principal there are three different ways to aquire post-mortem MRI images of the human brain tissue: (i) *in situ* post-mortem MRI of the entire body, (ii) *ex vivo* post-mortem MRI of the entire extracted brain in unfixed or fixed condition and (iii) *ex vivo* post-mortem MRI of single brain slices in unfixed or fixed condition. There are several factors affecting post-mortem MRI acquisition and the imaging result, depending on the chosen set-up. As there are several processes starting at the time of death or within several hours after death, the tissue properties and composition will change based on autolysis and degradation processes. These processes influence the contrast and quantitative MR parameters in all described set-up's. The most prominent post-mortem factor confounding MR images is the post-mortem interval between death, autopsy and MR acquisition. The preparation of tissue plays an important role when performing post-mortem MRI of entire extracted brains or single brain slices. Extracted tissue can be measured in unfixed or fixed condition. Fixation solutions are influencing the image contrast and quantitative parameter in post-mortem MRI. The temperature is one of the most prominent influences on the MR signal in a post-mortem MRI set-up. Conventional post-mortem MRI is usually performed at room temperature or below compared to approximately 37 °C core body temperature in *in vivo* MRI. Therefore consideration of different post-mortem effects is important when performing or planing post-mortem MRI.

The post-mortem interval is linked with the autolysis process of the body. Approximately 6 hours after death autolysis begins. Several cell-specific enzymes begin to degrade the tissue. This degeneration will change the tissue composition and properties and affects the image contrast and quantitative MR parameters. The post-mortem interval leads to an increase of the magnetization transfer ratio and a decrease of the diffusion properties as reported by D'Arceuil [134]. After three days of storage at room temperature human brain tissue showed an increase in $R_2^*$ values in different brain regions. In subsequent magnetometry measurements, a change of the paramagnetic and diamagnetic susceptibility was observed which is in line with the increase of $R_2^*$ observed in MRI. The temperature dependent magnetic moment of two brain tissue samples (basal ganglia and white matter) in fresh condition, directly after autopsy, and after two days of autolysis are compared in figure 2.23. The magnetic moment was measured at 1000 Oe and in a temperature range of 2.7 K to 100 K using Superconducting Quantum Interference Device (SQUID)
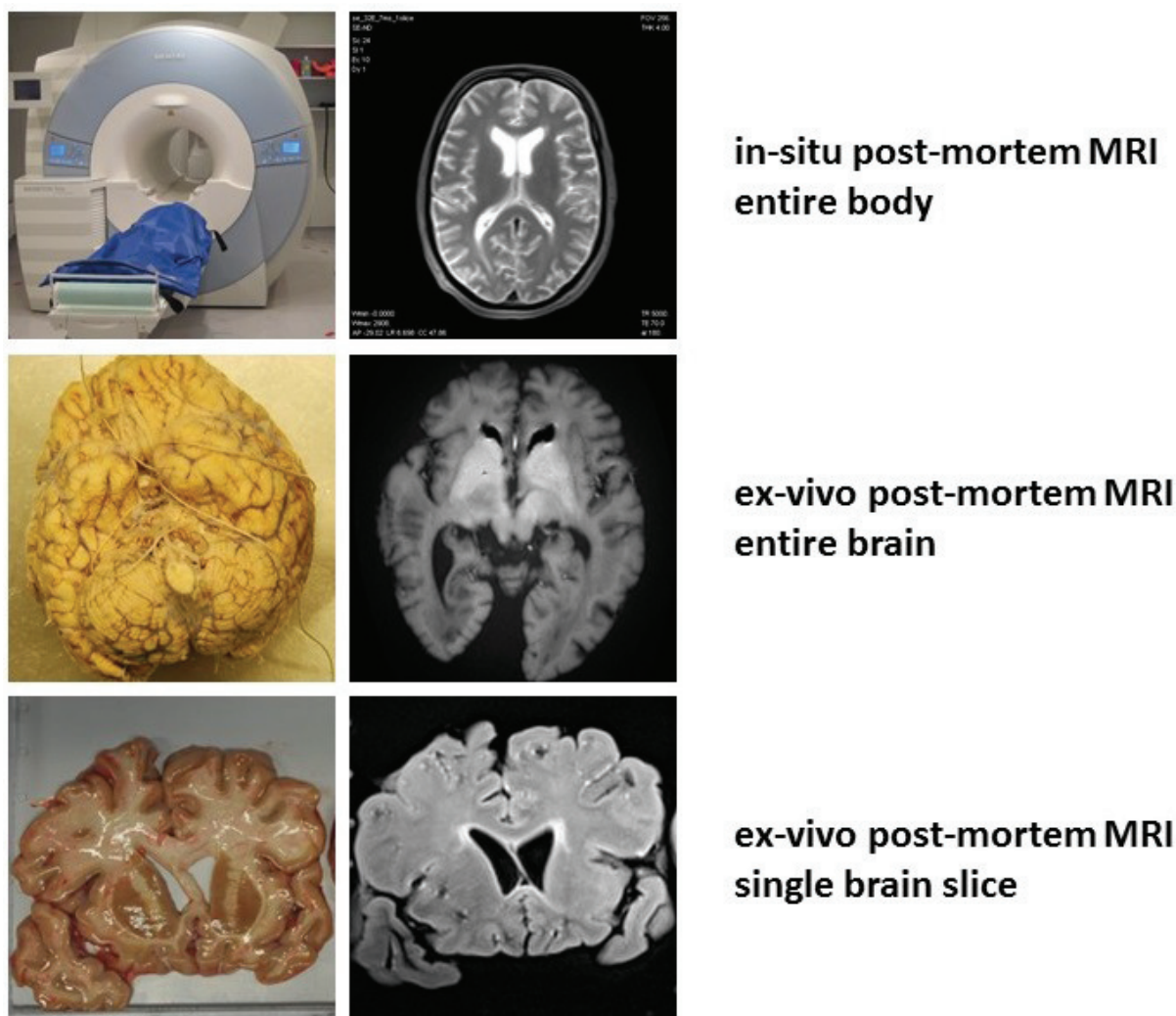
Figure 2.22: *The different possible post-mortem MRI acquisition strategies and a representative image acquired by post-mortem MRI of (i) the entire body, (ii) the entire extracted brain (formalin fixed condition) and (iii) a single brain slices (unfixed condition).*

magnetometry. The change of the paramagnetic and diamagnetic susceptibility caused by the autolysis is clearly visible.

Post-mortem imaging of the human brain can be performed *in-situ* or *ex-situ*. During the *in-situ* set-up the whole corpus is places in the scanner and the intact skull with the brain is placed in the head coil. In this set-up the brain is protected against deformation by the intact skull, comparable to *in-vivo*. MRI acquisition of extracted brains in an *ex-situ* set-up is challenging based on several confounding factors. The most important
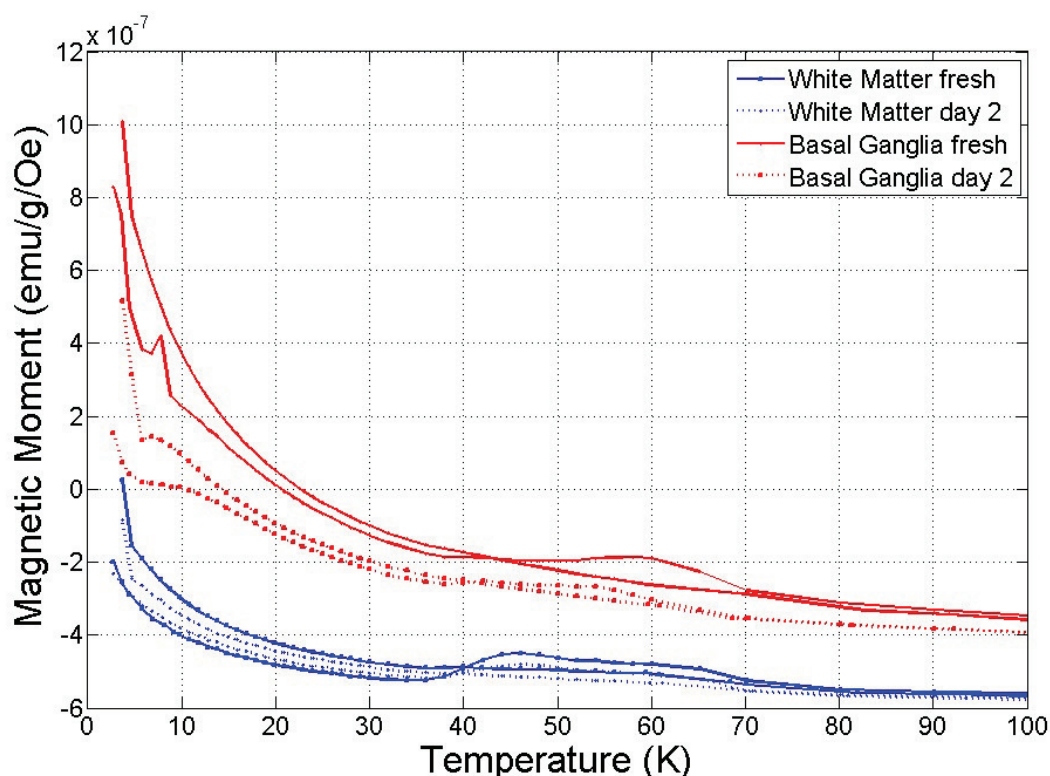
*Figure 2.23: The temperature dependent magnetic moment obtained with SQUID magnetometry of white matter and basal ganglia in fresh condition and after two days following autolysis.*

part is the stabilization of the extracted brain, to prevent deformation of the brain during image acquisition. This step is more important for unfixed brain tissue, than for fixed brain tissue based on the changed tissue stiffness after fixation. Different embedding procedures such as surrounding the brain with agar gel or surrounding the brain with a fluid, e.g. a proton free, inert fluid (Galden SV 80) are possible to protect the brain against deformation. If the whole brain is sliced before scanning, the embedding can be extended to a combined embedding with a gel and additional vacuum packing as shown in figure 2.24. To prevent autolysis and to store tissue samples over long time periods, a fixation reagent is used. Typically the tissue is immersed with formalin solution for a sufficient time to fix the tissue. This fixation process stops the tissue degradation and enables a suitable storage over long time periods. The chemical process of formalin fixation will dramatically change the tissue properties which define the contrast in MR images. Formalin fixation dramatically changes the relaxation times and diffusion properties. The $T_1$ relaxation time is reduced, up to 76% after formalin fixation. The $T_2$ and $T_2^*$ relaxation

(a) An unfixed human brain slice. (b) The brain slice after surrounding with agar gel. (c) After vacuumpacking of the gel surrounded tissue slice.

*Figure 2.24: The different steps of embedding an unfixed human brain slice (a) with agar gel (b) and subsequent vacuum packing (c).*

times are reduced similar to $T_1$ but with a magnitude between 5% and 35% depending on the brain region. The reduction of relaxation times is based on the change of water content and molecular protein structure. Formaldehyde cross links different side groups of proteins which arrange in huge complexes. These crosslinked structures and a slightly reduced water content are responsible for the changed tissue properties, leading to decreased relaxation times.

Usually post-mortem MRI is performed at room temperature or even at lower temperatures. The temperature of the sample during MRI is directly affecting the equilibrium magnetization and the relaxation processes. The equilibrium magnetization for a sample with N spins is given as

$$M_0 = \frac{N\gamma^2\hbar^2 J(J+1)}{3k_B T} B_0 \tag{2.95}$$

where $\gamma$ is the gyromagnetic ratio, $\hbar$ the Planck's constant devided by $2\pi$ and $J$ the quantum spin number, $k_B$ the Boltzmann constant, $T$ the temperature and $B_0$ the external magnetic field [135]. For protons with spin $= 1/2$ equation 2.95 is expressed as

$$M_0 = \frac{N\gamma^2\hbar^2 B_0}{4k_B T}. \tag{2.96}$$

If the temperature is reduced, the total steady state magnetization is increased. Beside the magnetization, all relaxation times ($T_1$, $T_2$ and $T_2^*$) as well as the magnetization transfer

ratio (MTR) show a tissue specific temperature dependency. The relaxation times showed a linear increase with increasing temperature in a range between 4 to 37 ℃.

The influence of the temperature on the proton resonance frequency was first described by Hindman in 1966 [136]. Thus, the temperature of the sample is affecting the magnitude and phase images resulting in a frequency shift [137]. A temperature difference $\Delta\vartheta(r)$ at a position $r$ can be calculated using phase images at different echo times according to

$$\Delta\vartheta(r) = \vartheta_2(r) - \vartheta_1(r) \approx -\frac{\varphi_2(r) - \varphi_1(r)}{\gamma B_0 \left(\Delta\sigma + \frac{2}{3}\Delta\chi_i\right) TE} \tag{2.97}$$

where $\Delta\sigma$ and $\Delta\chi$ are the temperature coefficients of the chemical shift and the susceptibility and $\varphi_1$ and $\varphi_2$ represents the two phase images. MRI is a suitable tool to monitor temperature changes, such as caused by thermal ablation. This is possible in post-mortem MRI and *in vivo* MRI. Several methods for MR thermometry are proposed in the literature and summarized in a review article of Rieke and Pauly [138].

The temperature effect of the phase is reflecting a change of the magnetic susceptibility based on the relationship between the phase $\varphi$ and the susceptibility $\Delta\chi$

$$\varphi = -\gamma \cdot \Delta\chi \cdot B_0 \cdot TE \tag{2.98}$$

where the temperature dependency of the magnetic susceptibility is depending on the magnetic properties of the material and described by Curie's law as discussed in the previous chapter.

The temperature is not only affecting relaxation mechanisms and magnetic susceptibility, but also to a certain level the diffusion of the water molecules. The decrease of diffusion, measurable in MRI, is directly linked with the temperature dependency of the Brownian motion. If the temperature is decreased, the random motion is slowed down. The relationship between the temperature and diffusion is given as

$$D \approx e^{-\frac{E_a(D)}{k_B T}} \tag{2.99}$$

where $D$ is the diffusion coefficient and $E_a(D)$ the activation energy of the molecular diffusion [138]. Using MRI, different diffusion properties, such as the mean diffusivity (MD), the radial diffusivity (RD) or the axial diffusivity (AD) can be calculated based on diffusion weighted sequences (DWI) [139]. These diffusion parameters shown a strong temperature influence, which is prominent when performing post-mortem MRI. The in-

crease of MD with increasing temperature is depending on the brain region as shown in figure 2.25. As discussed above, the temperature is a key parameter in post-mortem MRI,
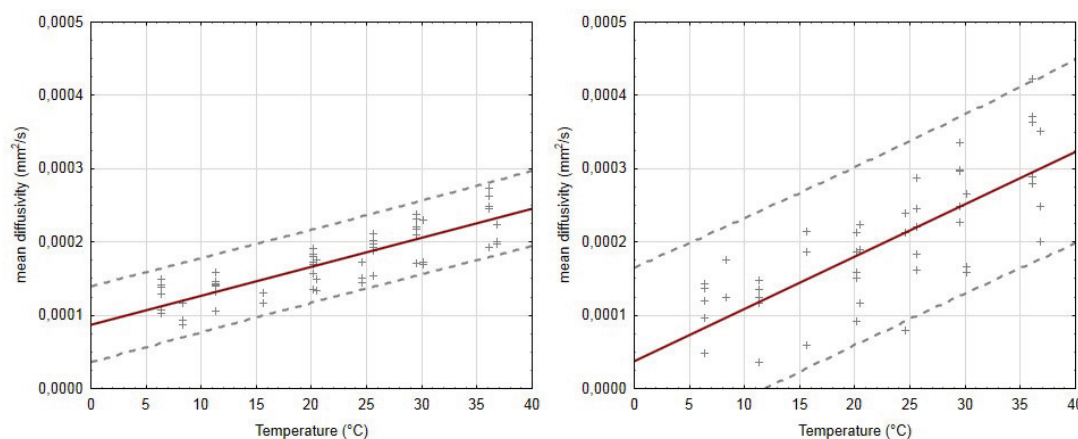


*Figure 2.25: The MD of white matter (left) and basal ganglia (right) versus temperature, measured in unfixed post-mortem brain samples. The temperature dependent increase in diffusion is depending on the brain region.*

which one can manipulate, compared to *in vivo* where the core body temperature is kept constant through a complex thermoregulation network to approximately 37 ℃.

Changing the temperature of the sample inside the magnet can be achieved using several methods. An easy but time consuming method would be to store the sample inside a refrigerator for several hours, to cool the sample to a certain level. The cooled sample is than placed inside the scanner for image acquisition. The sample is heated by the surrounding air until the sample temperature is equal to the room temperature. This is a slow process depending on the initial sample temperature and surrounding room temperature.

A more precise method would be to actively heat the sample using a second media such as water. To change the sample temperature a water circulation system is used. The scheme for an active temperature control is shown in figure 2.26. Therefore the sample is placed inside a sphere which is flooded with water. The temperature of the water is controlled by an heating and cooling device inside the water bath. The tempered water is pumped through the container to cool or heat the sample. Through the closed system the water is continuously exchanged and the temperature inside the sphere is stabilized after a specific time.

Through the changed temperature the steady state magnetization (equation 2.95), the contrast and relaxation times are changed depending on the chosen temperature [140] .
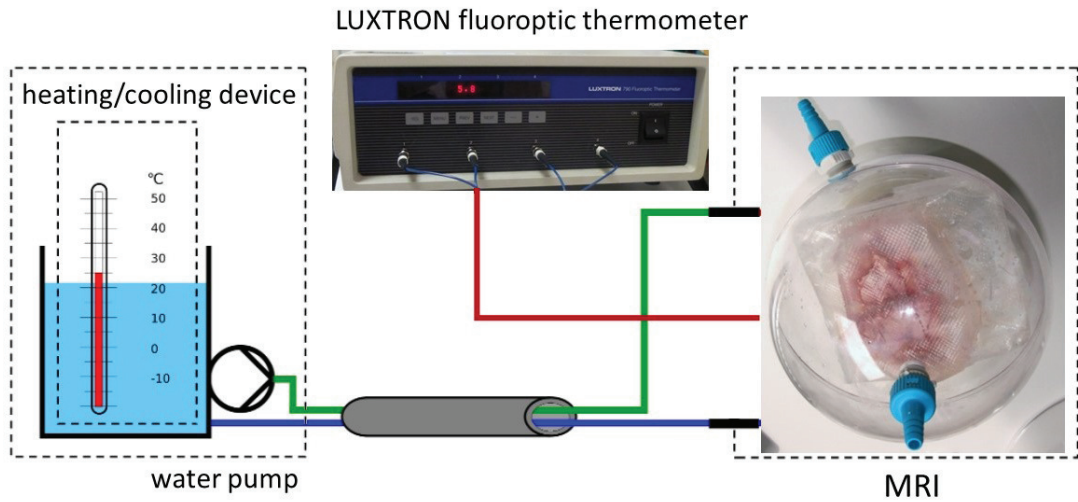
*Figure 2.26: A typical set-up for active temperature control based on a water circulation system. The brain slice is mounted in plastic sphere and the sphere is flushed with water at a controlled temperature.*

The relaxation times $T_1$, $T_2$ and $T_2^*$ are decreasing with decreasing temperature depending on the brain region.

The detailed influence of the temperature on the MR relaxation parameters and the susceptibility was one of the main topics in this thesis and is discussed in detail in the next sections.

# 3

# Temperature induced changes of MR relaxation times in the human brain: A post mortem study

Christoph Birkl[1], Christian Langkammer[1], Johannes Haybäck[2], Christina Ernst[2], Rudolf Stollberger[3], Franz Fazekas[1] and Stefan Ropele[1]

[1] Department of Neurology, Medical University of Graz, Austria
[2] Department of Neuropathology, Institute of Pathology, Medical University of Graz, Autria
[3] Institute of Medical Engineering, Graz University of Technology, Austria

## 3.1 Introduction

MR relaxation times are the most dominant sources of tissue contrast in MRI. Because the rotational and translational motion of water protons is linked with the correlation time for spin-spin and spin-lattice interaction, it is commonly assumed that $T_1$ and $T_2$ relaxation times are strongly affected by temperature [141, 142]. While this is of limited relevance for in vivo MRI where body temperature is auto regulated within a narrow range, considerable variations in tissue contrast can arise in post mortem MRI [143, 144] or in situations where MRI is used to monitor hyperthermia [145, 146] or cryotherapy [138].

The potential of MRI as a means to monitor tissue temperature is closely related to the exact knowledge of the temperature dependency of the relaxation times of specific tissue types. Similarly, findings from post mortem MRI can be translated to clinical MRI contrasts only if the effect of temperature is properly accounted for. However, the current knowledge on temperature dependency of relaxation times is very limited and widely lacking experimental validation. It is unclear for instance, if brain gray and white matter exhibit a different dependency on temperature. In addition, there seems to be a big discrepancy between temperature coefficients predicted by theory and those reported in the very sparse literature. While some conflicting results have been reported for $T_1$ [138] and $T_2$ [142], no temperature coefficients at all are available for $T_2^*$. Measurements of the coefficients for $T_1$ and $T_2$ in liquids or in tissue following chemical tissue fixation cannot serve to conclude on relaxation properties of the fresh human brain but rather introduce further bias [143].

Based on the relaxation theory of Bloembergen et al. [147], the effect of temperature on $T_1$ and $T_2$ was modelled by Bottomley et al. [141], Nelson and Tung [142] and Young et al. [89]. Nelson and Tung described the Fast Exchange Two State (FETS) model predicting a relationship between $T_1$ and the term $exp(-Ea/kT)$ where $Ea$ is the activation energy in $eV$, $k$ the Boltzmann constant and $T$ the absolute temperature in Kelvin. Over a small range of temperature, the relationship between temperature and $T_1$ can be assumed to be linear. Additionally, the FETS model predicts a small $T_2$ temperature dependency which is usually neglected. While the $T_1$ model may serve well for water or simple protein solutions it remains unclear if it is also suited for human tissue where water protons are usually compartmentalized and further restricted in their molecular mobility.

The goal of this study therefore was to experimentally assess the temperature dependency of the $T_1$, $T_2$, and $T_2^*$ relaxation times of different brain structures. Additionally, we

wanted to investigate how temperature affects the magnetization transfer ratio ($MTR$), a semi quantitative measure of magnetization transfer ($MT$) between tissue water and bound protons [148]. As formalin fixation can significantly affect the relaxation properties of tissue, we used in this study fresh unfixed human brain with a short post mortem interval to minimize autolytic changes. With this work, we expected to provide precise temperature coefficients which can serve as reference for other studies and to improve our understanding on the relevance of molecular mobility in highly compartmentalized structures for relaxation phenomena.

## 3.2 Methods

### 3.2.1 Preparation of brain samples

Five deceased subjects (mean age = 70 years) with an autopsy requested by the local health authorities were included in this study (Table 3.1). Immediately after autopsy a coronal brain slice with a thickness between 10 mm and 20 mm was harvested from each subject and prepared for MRI. To increase the stiffness of the unfixed tissue the brain slabs were embedded in agar gel (14 g/l), vacuum packed, and mounted in a plastic sphere with a diameter of 180 mm. Before and during MRI, the sealed plastic sphere was flushed with water at predefined temperatures between 4 °C and 37 °C. A refrigerated water bath with a heating immersion circulator (Julabo F20-C, Seelbach, Germany) was used for circulating the water through the sphere and for maintaining a predefined and constant temperature of the brain slice. To prevent flow artifacts, the water was not circulated during the MRI measurements but the temperature of the brain slice was measured continuously during the entire heating/cooling and scanning process using a LUXTRON 790 Fluoptic Thermometer (LumaSense Technologies, Santa Clara, CA, USA). The temperature variation during the MRI scans at a defined temperature level was approximately 0.5 °C.

### 3.2.2 MRI

All measurements were performed on a 3 T whole body MRI system (Magnetom Tim Trio, Siemens Healthcare, Erlangen, Germany) using a 12 element receive coil array. Starting at a temperature of approximately 4 °C, the samples were heated up and after a sufficient time the relaxometry was performed. After each scan the temperature was increased about

8 °C and the described procedure was repeated until the sample reached the maximum temperature of 37 °C. A typical scheme of temperatures was 5 °C, 12 °C, 21 °C, 30 °C, and 37 °C. All MR sequences were performed with FOV = 192 × 192 mm$^2$, matrix = 256 × 256, 7 slices, slice thickness = 3 mm, and GRAPPA acceleration Factor = 2. $T_1$ relaxation time data was acquired using a turbo inversion recovery (TIR) sequence with TE/TR = 6.4/8000 ms, 4 inversion times (TI = 200, 800, 1600, 3200 ms), and a turbo factor of 9. The $T_2$ relaxation time was determined with a turbo spin echo (TSE) sequence with three echo times (TE = 10, 73, 115 ms), a TR of 4000 ms, and a turbo factor of 5. $T_2^*$ relaxation data was acquired using a 3D RF spoiled gradient echo (GRE) sequence with 6 echoes (TE = 4.92, 10.34, 15.76, 21.18, 26.60, 32.02 ms), a TR of 300 ms, a flip angle of 15°, and 5 averages. MT weighted images were acquired with the same sequence as used for $T_2^*$ mapping, but with an additional off-resonant saturation RF pulse (offset frequency = 1.2 kHz, duration = 10 ms, flip angle = 500°) that was applied before the excitation pulse [148]. Relaxometry for a single temperature step lasted approximately 15 minutes.

## 3.2.3 Image processing and statistical analysis

Image processing and statistical analysis Image analysis was performed using MATLAB (The MathWorks, Natick, MA, USA) and statistical analysis was performed using GNU R Version 2.15.0 (The R Foundation for Statistical Computing). Relaxation times were assessed in white matter (frontal or occipital WM), cortical gray matter and in deep gray matter (basal ganglia and thalamus) of each brain sample by manually outlining the regions of interest. The $T_1$ relaxation time was calculated using a 3-parameter mono-exponential fitting routine which inherently corrects for flip angle errors and coil sensitivity. $T_2$ was calculated using the approach reported by Hasan et al. [96]. $T_2^*$ relaxation time was fitted assuming monoexponential signal decay. The MTR was calculated according to

$$MTR = 1 - \frac{M_S}{M_0} \cdot 100 \text{ in } \% \tag{3.1}$$

where $M_S$ and $M_0$ are the signal intensities acquired with and without MT saturation, respectively [149]. A linear regression model was applied to obtain the temperature coefficient from relaxation data at different temperatures. The temperature coefficient for each structure was assessed by determining the slope of the regression line between temperature

and relaxation time or MTR, respectively. After regional assessment, temperature coefficients were averaged across all samples. Results were considered as statistically significant with a p-value <0.05. The study was approved by the local ethics committee.

## 3.3 Results

Visual inspection of the TIR images showed distinct temperature induced changes in gray-white matter contrast. These changes are exemplarily shown in figure 3.1 which provides a series of TIR images (TI = 800 ms) acquired at five different temperatures. The best gray-white matter contrast was observed at temperatures closer to in-vivo conditions.

*Table 3.1: Subject Characteristics and post mortem time delay.*

| No. | Sex | Age | Time-delay (death to MRI) | Time-delay (autopsy to MRI) | Cause of death |
|-----|-----|-----|---------------------------|------------------------------|----------------|
| 1 | W | 58 | 43 h | 10 h | Sepsis |
| 2 | W | 53 | 44 h | 8 h | Dilatation of the left ventricular cavity |
| 3 | M | 76 | 24 h | 10 h | Pneumonia |
| 4 | M | 74 | 26 h | 8 h | Multiple organ dysfunction |
| 5 | M | 88 | 42 h | 10 h | Dilatation of the heart |
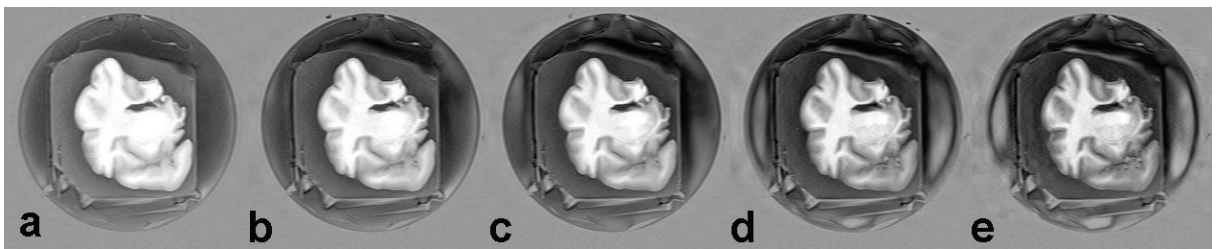


*Figure 3.1: Temperature induced change of T1 contrast in a TIR sequence (TI = 800 ms). Images are shown for a brain temperature of (a) 8.5 °C, (b) 15.9 °Cs, (c) 21.5 °C, (d) 30.1 °C and (e) 36.5 °C. At higher temperatures (right) the gray-white matter contrast is close to in-vivo conditions, while at lower temperatures the basal ganglia cannot be delineated owing to the lack of contrast (please see the intersection for these structures in Figure 3.3 at 10°C).*

For $T_2$, $T_2^*$ and MTR no such changes could be observed by visual inspection over the range of temperature investigated.

Table 3.2 summarizes all relaxation times ($T_1$, $T_2$, $T_2^*$) and MTR values separately for white matter (13 ROIs), cortex (9 ROIs), basal ganglia (4 ROIs), and the thalamus (4 ROIs). Among all parameters, $T_1$ showed the strongest dependency on temperature. The highest $T_1$ temperature coefficient, i.e. change of the relaxation time with temperature, was found in the cortex (coefficient = 17.4 ms/°C), followed by the basal ganglia (coefficient = 13.1 $ms$/°C), thalamus (coefficient = 7.6 ms/°C), and white matter (coefficient = 3.4 ms/°C) (Figure 3.2). In contrast, $T_2$ did not show a significant dependency on tem-

*Table 3.2: Relaxation times, MTR values and corresponding temperature coefficients of different brain regions at 3T.*

|  |  | $T_0$ | Temp. coeff. (1/°C) | $R^2$ | P | Std. error slope (%) |
|---|---|---|---|---|---|---|
| White Matter | $T_1$ (ms) | 695.8 ± 29.2 | 3.4 ± 0.7 | 0.91 | 0.007* | 0.031 |
|  | $T_2$ (ms) | 91.2 ± 17.4 | -0.2 ± 0.2 | 0.35 | 0.299 | 0.016 |
|  | $T_2^*$ (ms) | 36.5 ± 6.6 | 0.1 ± 0.1 | 0.58 | 0.192 | 0.007 |
|  | MTR | 0.315 ± 0.036 | 0.0015 ± 8e-04 | 0.67 | 0.093 | 0.060 |
| Cortex | $T_1$ (ms) | 962 ± 67.7 | 17.4 ± 5.3 | 0.97 | 0.002* | 0.149 |
|  | $T_2$ (ms) | 132.1 ± 23 | 0.2 ± 0.7 | 0.33 | 0.319 | 0.030 |
|  | $T_2^*$ (ms) | 39.3 ± 10 | 0.2 ± 0.3 | 0.56 | 0.171 | 0.019 |
|  | MTR | 0.231 ± 0.062 | 0.0015 ± 9e-04 | 0.62 | 0.108 | 0.076 |
| Basal Ganglia | $T_1$ (ms) | 738.5 ± 52.2 | 13.1 ± 2.4 | 0.96 | <0.001* | 0.116 |
|  | $T_2$ (ms) | 84.7 ± 27.7 | 0.3 ± 0.2 | 0.54 | 0.133 | 0.038 |
|  | $T_2^*$ (ms) | 31.9 ± 11.9 | 0.2 ± 0.1 | 0.91 | 0.003* | 0.023 |
|  | MTR | 0.290 ± 0.029 | 0.0026 ± 0.0013 | 0.87 | 0.006* | 0.036 |
| Thalamus | $T_1$ (ms) | 656.8 ± 11.9 | 7.6 ± 0.4 | 0.97 | <0.001* | 0.053 |
|  | $T_2$ (ms) | 82.1 ± 26.7 | 0.2 ± 0.2 | 0.33 | 0.352 | 0.050 |
|  | $T_2^*$ (ms) | 19.6 ± 5.8 | 0.2 ± 0 | 0.79 | 0.033* | 0.011 |
|  | MTR | 0.256 ± 0.034 | 0.002 ± 0.0013 | 0.74 | 0.040* | 0.125 |

perature in any of the investigated brain structures. A similar observation was made for $T_2^*$ with the exception of the basal ganglia and the thalamus where a significant positive relationship was found. In parallel, the MTR showed a positive correlation with tissue temperature in the basal ganglia (coefficient = 2.6 ms/°C) and the thalamus (coefficient = 2.0 ms/°C) but not in white matter and the cortex as shown in figure 3.3. Using the linear correlation model the $T_1$, $T_2$ and $T_2^*$ relaxation times were extrapolated to 37 °C and compared to in-vivo values reported in literature. As shown in Table 3.3, there was
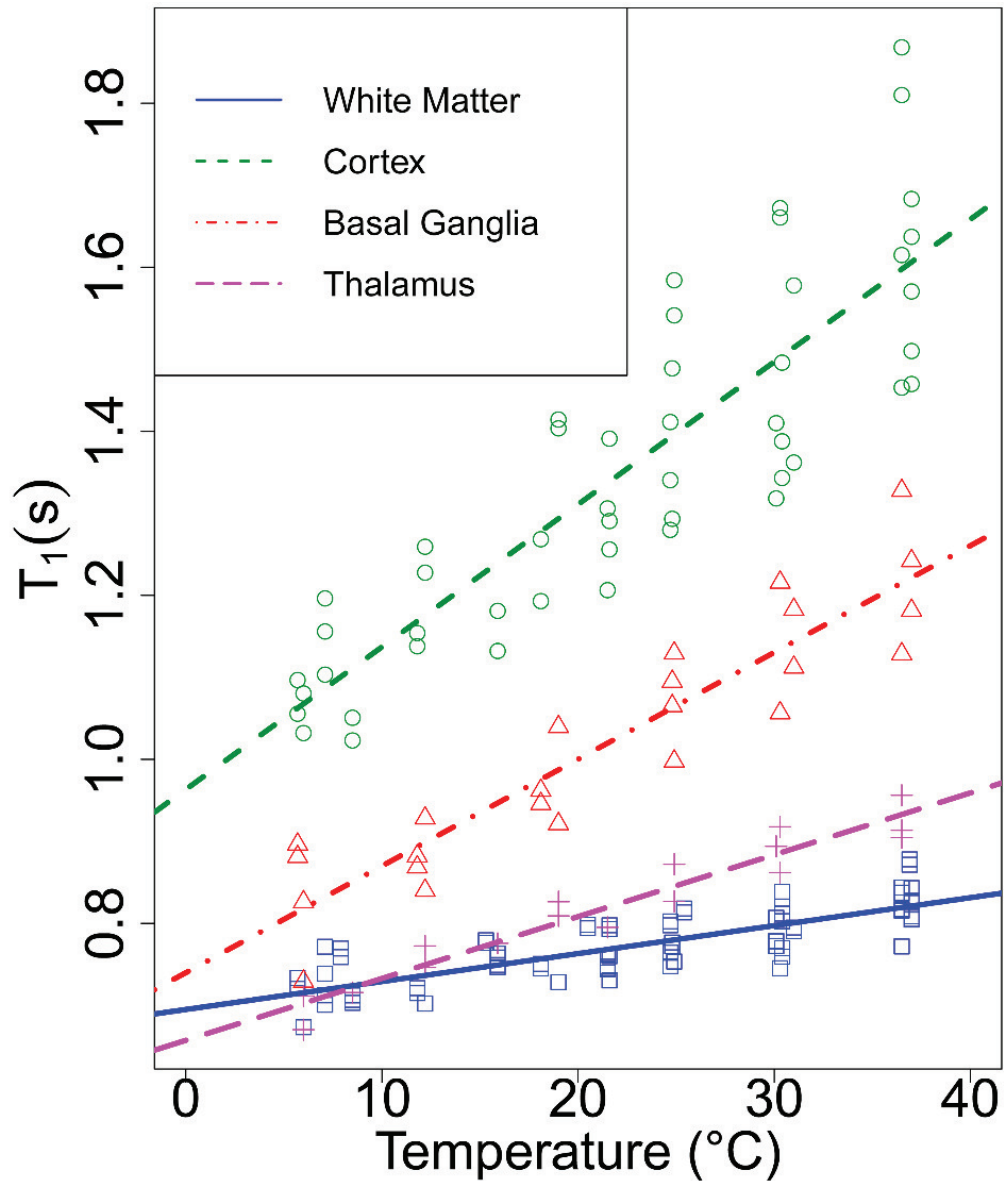
Figure 3.2: *Longitudinal $T_1$ relaxation time versus temperature in white matter, cortex, basal ganglia and thalamus. Each symbol corresponds to a brain sample from an individual subject.*

an excellent agreement with literature in particular in the cortex and in white matter.

## 3.4  Discussion and Conclusion

The post mortem setup used in this work enabled the investigation of the relationship between temperature and relaxation times in brain tissue. In contrast to previously re-
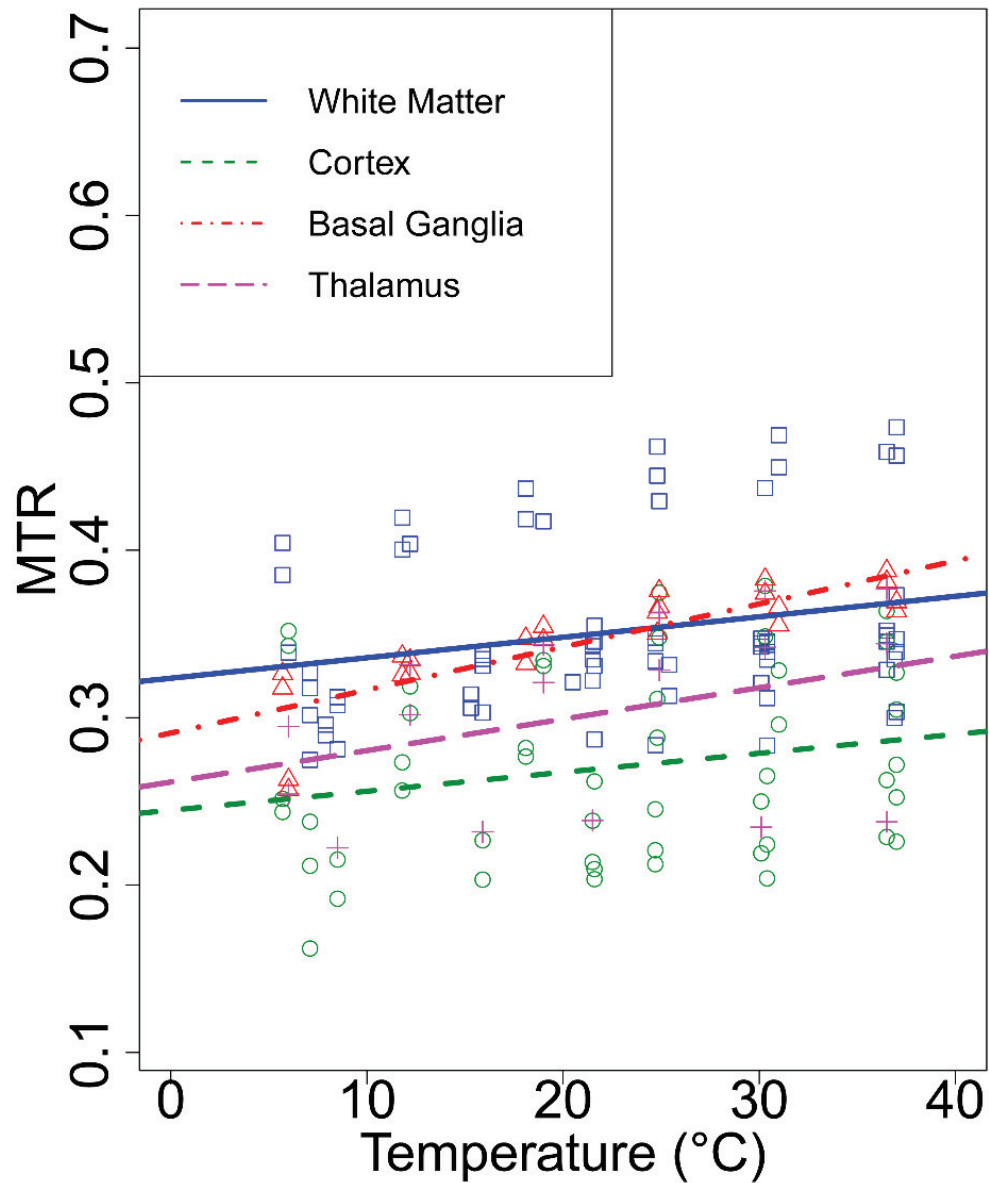
*Figure 3.3: Magnetization transfer ration (MTR) versus temperature in white matter, cortex, basal ganglia and thalamus. Each symbol corresponds to a brain sample from an individual subject.*

ported post mortem work, we aimed at assessing these parameters in the absence of any fixation effects [144, 156] by using fresh brain tissue within a post mortem delay of less than 48 hours. By keeping the time between death and image acquisition as short as possible, we wanted to minimize autolysis effects and to achieve a situation that is very close to an in vivo condition. To our knowledge, this work for the first time provides

Table 3.3: $T_1$, $T_2$ and $T_2^*$ relaxation times obtained in this study (extrapolated to 37°C) compared to literature.

| Tissue | Parameter | This study | Literature | Reference |
|---|---|---|---|---|
| White Matter | $T_1$ (ms) | $821.6 \pm 55.1$ | $838 \pm 50$ | [150] |
| | $T_2$ (ms) | $83.8 \pm 24.8$ | $76 \pm 3$ | [151] |
| | $T_2$* (ms) | $40.2 \pm 10.3$ | $53.2 \pm 1.2$ | [152] |
| Cortex | $T_1$ (ms) | $1605.8 \pm 263.8$ | $1607 \pm 112$ | [153] |
| | $T_2$ (ms) | $139.5 \pm 48.9$ | $88 \pm 3$ | [154] |
| | $T_2$* (ms) | $55.2 \pm 14.1$ | $66.0 \pm 1.4$ | [155] |
| Basal Ganglia (Putamen) | $T_1$ (ms) | $1253.4 \pm 50.6$ | $1363 \pm 58$ | [153] |
| | $T_2$ (ms) | $84.6 \pm 21.1$ | $66 \pm 2$ | [154] |
| | $T_2$* (ms) | $35.9 \pm 6.5$ | $31.5 \pm 2.5$ | [155] |

detailed systematic temperature coefficients of $T_1$, $T_2$, $T_2^*$ relaxation times and MTR for different structures of the human brain.

Longitudinal relaxation showed the strongest temperature dependency with a linear behavior in the range of interest. While the linear relationship is predicted by the FETS model, the estimation of the temperature coefficient by this model fails because the activation energy in tissue is an empirically determined constant and is unknown for brain tissue. The activation energy itself is independent of temperature but is affected by the chemical structure of the tissue. When comparing the temperature coefficients found in this study with those reported in the literature, it appears that previous efforts have markedly underestimated the temperature coefficient for the longitudinal relaxation at least in gray matter. Rieke and Pauly [138] as well as Quesson et al. [157] reported a temperature coefficient in the order of $1\,\%/°C$ which is significantly lower than found in our specimen. A possible explanation for this discrepancy is that these authors used mixed tissue samples, i.e. material with contributions from white matter for their investigations.

A previously unrecognized finding is that different brain compartments exhibit different

temperature coefficients for $T_1$ with lowest coefficients in white matter. A likely reason for this is the fact that longitudinal relaxation is strongly determined by the molecular mobility and is already limited in the intracellular cytoplasm of the myelinated axons. The approximately $10\%$ higher water content in gray matter than white matter structures may have additionally contributed to a three-fold increased temperature coefficient of gray matter compared to white matter [150,151]. Interestingly, microstructural changes related to autolysis seem to play only a minor role regarding the temperature coefficient of $T_1$. While the variation in the post mortem interval of our samples may have introduced some overall changes in $T_1$ the variability of the temperature coefficient was very low across samples (Figure 3.1).

The TIR sequence used to obtain $T_1$ is known for its sensitivity for off-resonant saturation effects introduced by the train of refocusing RF pulses. As a consequence, multi-slice $T_1$ mapping can underestimate $T_1$ due to magnetization transfer effects [152]. Nevertheless, we have opted for this sequence because a conventional inversion recovery sequence would have had significantly increased the post mortem delay and also the likelihood of tissue warming as the water was not circulated during MRI. While the TIR sequence is insensitive to $B_1$ errors or inhomogeneities, other fast methods would have required a $B_1$ correction [158,159]. We expected that the MT effect for the TIR was low, because only a few slices with a moderate turbo factor were acquired. This could be confirmed when comparing the temperature corrected $T_1$ values with literature. In contrast to longitudinal relaxation, our results suggest that temperature does not play a significant role for transverse relaxation. Although a small effect on $T_2$ is predicted by the FETS model and also has been observed in a 10% Liposyn solution [142], compartmentalization of tissue water seems to reflect a condition which is not fully addressed by a simple temperature model. Similar observations were made for $T_2^*$ with the exception that a positive correlation of $T_2^*$ and the temperature was found in deep gray matter structures. These parts of the brain are known to be rich in iron and the iron content could in fact be an explanation for our finding. The rate $1/T_2^*$ can be considered as the sum of $1/T_2$ and $1/T_2'$ with the latter being proportional to $\Delta B_0$ if the magnitude of the magnetic susceptibility $\chi$ is very small [82]. According to Curie's law, the paramagnetism of iron drops with increasing temperature while the diamagnetism constituted by other tissue components is independent of temperature [86,160]. Consequently, iron induced susceptibility variations DeltaChi are smaller at higher temperatures which should result in a longer $T_2^*$ time. Despite blood was not fully flushed out during brain extraction, we did not expect any effect on the regional

$T_2^*$ analyses because all regions were outlined distant from larger vessels and the relative blood volume constituted by capillaries is very low. Susceptibility changes induced by deoxyheme are usually much smaller than ferritin induced changes.

In this study we also were interested to investigate the impact of temperature on the MTR. Most MT validation studies comparing MR and histopathologic findings have been done at room temperature and this might also explain the differences between MTR values reported from these experiments and those found under in vivo conditions [156, 161]. In brain tissue, modeling of MT is usually done with the two-pool model [148], which accounts for macromolecular bound protons that act as an additional relaxation sink and therefore enables the tissue water pool to faster achieve steady state magnetization. The MTR can be considered as weighted sum of all 6 fundamental pool parameters. Temperature is expected to affect at least two pool parameters, the $T_1$ relaxation time of the tissue water pool and the rate of magnetization exchange between both pools mediated by chemical exchange and dipolar coupling. This means that a temperature induced prolongation of the tissue water $T_1$ is counteracted by a faster exchange of magnetization with the bound pool which in turn results in a shortening of $T_1$. Which of both $T_1$ modulating mechanisms is more dominant will depend on the underlying pulse sequence (proton density weighted versus $T_1$ weighted). Thus our finding of an overall small effect of temperature on the MTR appears plausible. A more quantitative consideration would require a numerical simulation of the coupled Bloch equations. Again, the significant association between MTR and temperature which we found in the basal ganglia and thalamus is most likely related to the effect of iron. The temperature induced susceptibility shift in these structures is expected to decrease microscopic field gradients which in turn decreases direct saturation effects of the MT pulse by narrowing the resonance peak of the tissue water [27].

In conclusion, temperature has a strong effect on $T_1$ especially in brain gray matter and much smaller in white matter. This has to be considered when performing post mortem MRI studies at room temperature. The temperature coefficients provided by this study can serve as reference for correcting $T_1$ or for adjusting relaxivity based temperature mapping methods in the brain given the linearity of observed associations. The transverse relaxation times $T_2$ and $T_2^*$ as well as MTR do not show a significant temperature dependency except for the thalamus and basal ganglia. Respective temperature related variations in these regions appear most likely related to the high iron content of these structures.

**4**

# Iron mapping using the temperature dependency of the magnetic susceptibility

Christoph Birkl[1], Christian Langkammer[1], Heinz Krenn[2], Walter Gössler[3], Christina Ernst[4], Johannes Haybäck[4], Rudolf Stollberger[5], Franz Fazekas[1] and Stefan Ropele[1]

[1] Department of Neurology, Medical University of Graz, Austria

[2] Institute of Physics, Experimental Physics, University of Graz, Austria

[3] Institute of Chemistry, Analytical Chemistry, University of Graz, Austria

[4] Department of Neuropathology, Institute of Pathology, Medical University of Graz, Autria

[5] Institute of Medical Engineering, Graz University of Technology, Austria

# 4.1 Introduction

Iron is the most abundant trace element in the human brain which also reflects its multiple and important roles in maturation of the central nervous system and brain metabolism. Not unexpected, iron homeostasis is distorted in several inflammatory and neurodegenerative diseases including multiple sclerosis, Alzheimer's disease, Parkinson's disease or amyotrophic lateral sclerosis [92,162–168]. As the etiology of iron in the inflammatory and neurodegenerative cascade is largely unknown, there is increasing interest in techniques for non-invasively assessing iron levels.

Magnetic resonance imaging (MRI) is the only imaging technique in this context, because it is non-invasive and sensitive to local field changes induced by iron compounds. Several MR based methods for measuring iron concentration in the brain have been proposed including relaxation time mapping [20,104], also under varying field strength [164], magnetic field correlation imaging [25], direct saturation imaging [27], and quantitative susceptibility mapping (QSM) [169–171]. So far, QSM and $R_2^*$ mapping have been identified and validated as the most promising approaches because they can be derived from a conventional gradient echo sequence that is readily available on clinical scanners and because they scale linearly over the entire physiological range of iron concentration [22,28].

The latter, however, was shown for gray matter only. White matter has a diamagnetic bulk susceptibility which is mainly constituted by the myelin and tissue water which means that the paramagnetic effect of iron is counteracted by the diamagnetic myelin [109,110]. Additionally, the contribution of the myelin depends on the orientation of the myelinated fiber bundles with respect to the main magnetic field ($B_0$) [109,172–174]. Consequently, iron concentrations derived from white matter are not reliable regardless of the method applied.

We here present a new approach for iron mapping which is particular relevant for white matter. It is based on the temperature dependency of the paramagnetic effect of iron, which is predicted by Curie's law and which we recently observed in brain structures with high iron content [140]. The proposed approach was tested in postmortem brain tissue and validated with Superconducting Quantum Interference Device (SQUID) magnetometry and with ICP mass spectrometry.

## 4.2 Theory

The magnetic tissue susceptibility $\chi_{tissue}$ is the sum of all individual paramagnetic and diamagnetic contributions. According to Curie's law, the paramagnetic part of the magnetic susceptibility shows an inverse temperature dependency,

$$\chi_{tissue} = \chi_{para} + \chi_{dia} = \frac{C}{T - \vartheta} + \chi_{dia} \tag{4.1}$$

where $C$ is the material specific Curie constant, $\vartheta$ is the paramagnetic Curie temperature, and $T$ is the temperature. In contrast, the temperature dependency of the diamagnetism is based on indirect effects such as tissue volume change due to molecular rearrangement and is insignificant. While the magnetic susceptibility is often derived from MR phase images [170, 171, 175], this work is based on the transverse relaxation rate $R'_2(= 1/T'_2)$ which is directly related to the microscopic susceptibility difference between the tissue matrix and paramagnetic contributions within a voxel or volume of interest ($\Delta\chi$) [102]

$$R'_2 = \lambda\gamma\Delta\chi B_0 \tag{4.2}$$

where $\lambda$ is a geometric factor that considers the microscopic distribution of susceptibilities, $\gamma$ is the gyromagnetic ratio and $B_0$ is the main magnetic field.
$R'_2$ cannot be assessed in a single measurement but can be calculated from $R^*_2(= 1/T^*_2)$ and $R_2(= 1/T_2)$ because $R^*_2 = R_2 + R'_2$. The rate $R_2$ reflects the rate of coherence loss due to non-static dephasing effects which cannot be reversed with an RF refocusing pulse. Therefore, the susceptibility difference can be calculated by reforming Equation 4.2.

$$\Delta\chi = \frac{(R^*_2 - R_2)}{\lambda\gamma B_0} = \frac{R'_2}{\lambda\gamma B_0} \tag{4.3}$$

It should be mentioned that $\Delta\chi$ is not a measure of bulk susceptibility. However, in most tissues iron is equally distributed over tissue compartments (e.g. neurons, oligodendrocytes, and endothelia cells) rather than focally accumulated. The microscopic variation of susceptibility therefore is expected to scale with iron concentration which is the basis for the proposed approach. Microscopic field gradients in a tissue are built up by paramagnetic and diamagnetic sources. In most biological tissue, the high water content leads to a weak diamagnetic behavior with a bulk susceptibility of about -9.05 ppm [82]. Considering the two possible sources of the susceptibility variation only the paramagnetism

induced dephasing of the transverse magnetization causes a temperature dependency of $R_2'$

$$R_2'(\vartheta) = R_{2,para}'(\vartheta) + R_{2,dia}' \tag{4.4}$$

where $\vartheta$ is the temperature of the tissue.

We here propose to estimate the iron content from a linear model by mapping $R_2'$ at different tissue temperatures

$$R_2'(\vartheta) = R_{2,0}' + \vartheta \cdot TcR2p \tag{4.5}$$

Here, the temperature coefficient $TcR2p$ of $R_2'$ represents the paramagnetic source and the offset ($R_{2,0}'$) the diamagnetic source of the microscopic variation of susceptibility. In biological tissues, where iron is by far the most abundant paramagnetic trace element, the temperature coefficient $TcR2p$ is depending on the iron concentration and thus resulting in

$$TcR2p(Fe) = TcR2p_0 + k \cdot [Fe] \tag{4.6}$$

where $k$ is the slope depending on the iron concentration and $TcR2p_0$ the offset which is expected to be zero in the absence of instrumentation errors.

SQUID magnetometry allows to probe the susceptibility of tissue samples at very low magnetic fields (5 – 1000 Oe). Additionally, magnetic blocking effects of ultra-small iron compounds (iron-oxides encapsulated in protein shells such as ferritin) can be investigated using sophisticated time-measurement protocols. As interacting iron-oxide nanomagnets relax very slowly (hours or even days) and are therefore beyond the time frame of MR techniques for a direct detection, SQUID can provide complimentary insights to MR based susceptibility measurements. Neglecting magnetic blocking phenomena, the tissue susceptibility as assessed by SQUID can be modeled by Equation 4.1. Then, the Curie constant $C$ can be obtained by fitting Equation 4.1 to the SQUID data with (see also Table VII of Ref. [82])

$$C = \frac{N_{Fe}\mu_{eff}^2}{3k_B} = \frac{C_{Fe}N_{tissue}\mu_{eff}^2}{3k_B} = 10^{-6}C_{Fe}[\frac{\mu g_{Fe}}{g_{tissue}}]\frac{M_{sat}g\mu_B(S+1)}{3k_B} \tag{4.7}$$

Since iron is sparsely distributed within tissue, the Curie constant $C$ here is normalized to the tissue mass in units of $emuK/(g_{tissue}Oe)$. The iron concentration $N_{Fe}$ in Equation 4.7 is expressed by $C_{Fe}N_{tissue}$ with $C_{F}e$ in units of $\mu$g-iron/g-tissue. The square of the effective magnetic moment of Fe-ions is $\mu_{eff}^2 = g^2\mu_B^2 S(S+1)$ and can be substituted by $\mu_{eff}^2 = g\mu_B(S+1)M_{sat}/N_{tissue}$, using $M_{sat} = N_{tissue}g\mu B_S$ as the saturation magnetization of iron per gram tissue. $M_s at$ corresponds to approximately $500\,$emu/g (if all tissue atoms are replaced by iron atoms, i.e. $C_{Fe} = 106\,\mu$g/g $= 1$). S is the spin of an iron-atom (S = 2 for $Fe^{2+}$), g = 2 the Landé-factor, $\mu_B = 9.274 \cdot 10 - 24$ J/T the Bohr's magneton, and $k_B = 1.38 \cdot 10 - 23$ J/K Boltzmann's constant. The Curie constant can slightly vary for $Fe^{2+}$ and $Fe^{3+}$ depending on a low or high spin moment.

## 4.3 Methods

### 4.3.1 Preparation of brain samples

MRI and mass spectroscopic measurements were performed with brain tissue from five deceased subjects (mean age = 70 years) after an autopsy requested by the local health authorities. Following autopsy, the brains were cut into 10 mm to 20 mm thick coronal slices. The unfixed brain slices were prepared for MRI by embedding them in agar gel (14 g/l) and by vacuum packing to minimize autolysis and to increase the stiffness of the tissue. After MRI the agar gel was removed and the brain slices were fixed in a solution of 4 % formalin until further analysis with a SQUID magnetometer and a mass spectrometer. SQUID magnetometry was performed with three samples (two samples from white matter and one sample from grey matter) from a single brain slice. For testing whole brain mapping of the temperature coefficient, a freshly extracted brain was mounted in a plastic container filled with Galden SV80 (Solvay Solexis S.p.A) which is a 1H-free fluorinated solution that minimizes macroscopic susceptibility artifacts at brain-solution boundaries. Approximately 30 minutes were required for tissue preparation for MRI and another 30 minutes were required to prepare the samples for SQUID magnetometry. The study was approved by the local ethics committee.

### 4.3.2 Experimental setup and MRI

The prepared tissue samples were mounted in a plastic sphere (180 mm diameter) and centered in the head coil. The sphere was flushed with water at a controlled temperature

to heat or cool the tissue sample. Relaxometry was performed at 6 different temperatures between 4 ℃ and 37 ℃. During the entire experiment the temperature at the surface of the sample was measured with a LUXTRON 790 Fluoroptic Thermometer (LumaSense Technologies, Santa Clara, CA, USA). All experiments were performed on a 3 $T$ whole body MRI system (Magnetom Tim Trio, Siemens Healthcare, Erlangen, Germany) using a 12 element receive coil array. All MR sequences were performed with common geometric parameters FOV = $192 \times 192$ mm$^2$, matrix = $256 \times 256$, 7 slices, slice thickness = 3 mm and GRAPPA acceleration Factor = 2. The $T_2$ relaxation time was determined with a dual echo turbo spin echo (TSE) sequence ($TE_1 = 10$ ms, $TE_2 = 73$ ms, TR of 4000 ms, TSE turbo factor = 5). $T_2^*$ relaxation data was acquired using a 3D RF spoiled gradient echo (GRE) sequence with 6 echoes (TE = 4.92, 10.34, 15.76, 21.18, 26.60, 32.02 ms, TR = 300 ms, flip angle of 15°, 5 averages). The total scan time was approximately 15 minutes for each temperature point. For temperature coefficient mapping of the entire ex vivo brain the same sequences were used with an in-plane resolution of $1 \times 1$ mm$^2$, slice thickness = 2 mm, 10 averages and a total scan duration of 20 minutes for each temperature point.

### 4.3.3 SQUID magnetometry

Superconducting Quantum Interference Device (SQUID) measurements were performed with a Quantum Design MPMS-XL-7 (Quantum Design Inc., San Diego, CA, USA) to measure the absolute susceptibility of three tissue samples from a single brain slice. To avoid spurious magnetic signals due to volume changes by swelling and to reduce residual amounts of paramagnetic oxygen, the tissue samples were exposed to a reduced-pressure helium gas atmosphere of 50 mbar in the SQUID-cryostat-chamber above 260 K. Only formalin fixed samples were used because of logistic restrictions it was not possible to analyze unfixed brain tissue. Following a cool down under zero magnetic field to 1.7 K, the magnetic field (1000 Oe) was turned on and the temperature was first cycled up to room-temperature (ZFC-zero field cooled scan) and then back to 1.7 K (FC-field cooled scan). By fitting Equations 4.1 and 4.7 to the resulting temperature dependent susceptibility curve, the Curie constant, the paramagnetic Curie temperature, the diamagnetic background, and the iron content were obtained. To relate the paramagnetic susceptibility of iron to the temperature dependent MRI relaxivity studies, we extrapolated the low-temperature SQUID data to the high temperature range of interest (4 ℃ – 37 ℃) and subtracted the diamagnetic background in this temperature range. The measure-

ment procedure was repeated at a much higher magnetic field comparable to the MRI scanner field (2.89 T). To directly compare the SQUID results with MRI data, Equation 4.2 was used to estimate $R_2'$. The microscopic susceptibility variation $\Delta\chi$ was obtained by taking the difference between the paramagnetic susceptibility obtained by SQUID and tissue water ($\chi_{water} = 9.05 \cdot 10^{-6}$). For simplicity, the effect of myelin was neglected and the geometric factor $\lambda$ was fixed to 1 for all tissue types. The mass susceptibility (in units of emu/g/Oe) was converted to SI volume susceptibility by multiplication with the tissue mass density ($\rho = 1.05 \cdot 10^3$ kg/m$^3$), and the units emu /g Oe were transformed to the corresponding SI units.

### 4.3.4 Chemical assessment of iron concentration

Following SQUID measurements, the absolute iron concentration in 20 tissue samples from five brain slices was independently determined with inductively coupled plasma mass spectrometry (Agilent 7500ce; Agilent Technologies, Waldbronn, Germany). First the samples were freeze dried and then mineralized using nitric acid in a microwave heated autoclave (Ultra- CLAVE III; EMLS, Leutkirch, Germany). Helium was used as a collision gas at a flow rate of 5.3 mL/min to reduce possible polyatomic interferences at a mass to charge ratio of 56.

### 4.3.5 Image processing and statistical analysis

Image analysis was performed using MATLAB (The MathWorks, Natick, MA, USA) and statistical analysis was performed using STATISTICA Version 7.1 (StatSoft, Tulsa, OK, USA). $R_2^*$ maps were obtained by fitting a single-exponential decay function to the magnitude of the individual echoes. $R_2$ maps were calculated from the two echoes of the TSE sequence [96]. At each temperature point a $R_2'$ map was calculated by subtracting the $R_2$ map from the corresponding $R_2^*$ map. The temperature coefficient of $R_2'$ was obtained by a linear regression between temperature and corresponding $R_2'$. The temperature coefficient TcR2p then was compared with the slope found from the SQUID measurements for the high temperature range. A linear regression model was also used to compare the sensitivity of $R_2^*$, $R_2'$ and the temperature coefficient of $R_2'$ for the iron content in gray and white matter as determined by mass spectrometry. A p-value lower than 0.05 was considered as statistically significant.

## 4.4 Results

### 4.4.1 Superconducting Quantum Interference Device (SQUID)

The SQUID measurements yielded tissue specific susceptibility T-scans which were consistent for ZFC and FC (Figure 4.1). The cortex showed the strongest temperature dependency and also a bifurcation of the ZFC/FC-susceptibility curve which can be related to blocking effects of iron-oxide. The susceptibility of white matter was more diamagnetic with some variation between both white matter samples. The parameters extracted from the fits of Equations 4.1 and 4.7 including the estimated iron concentration (CFe) are summarized in Table 4.1.
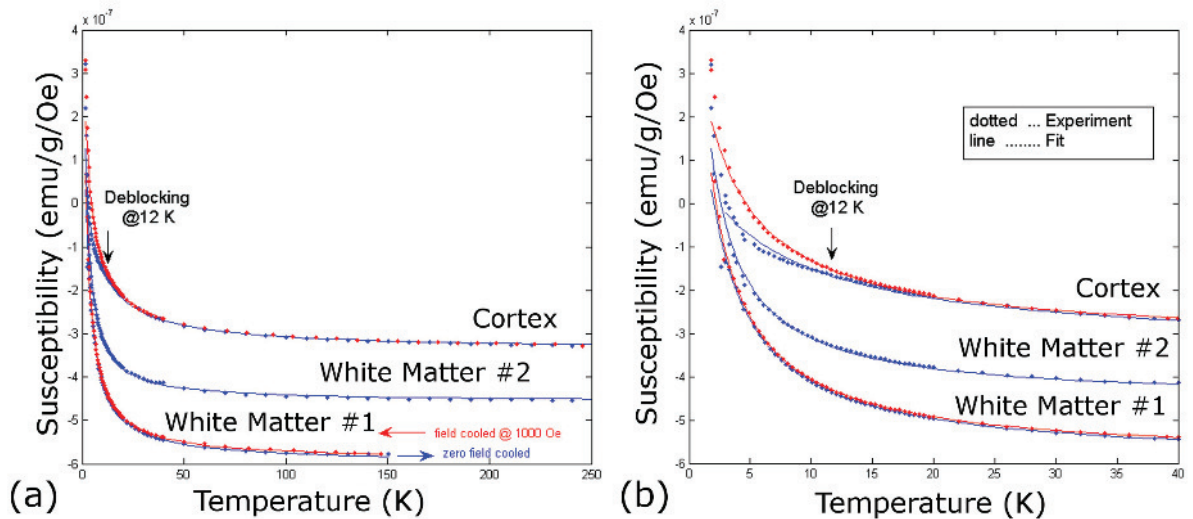


*Figure 4.1: (a) Tissue susceptibility in units of emu/g/Oe under zero-field-cooled (ZFC: blue) and field-cooled (FC: red) conditions in the tem- perature range 1.7–250 K for three different samples of a human brain slice, magnetic field was 1000 Oe. (b) The susceptibility for the range 3–40 K for which the fit to Eq. 4.1 has been optimized. Note the splitting of ZFC/FC scans in the cortex which indicates a mag- netic blocking of agglomerated (ferritin-like) iron particles.*

### 4.4.2 Mass spectrometry

Mass spectrometry revealed highest iron concentrations in the basal ganglia (mean = 130 ± 23 mg/kg) and lowest iron concentration in white matter (mean = 31.6 ± 3.4 mg/kg). Iron concentration in the cortex (mean = 33.6 ± 5.2 mg/kg) was slightly higher than in white matter. In the three samples that were referred to SQUID, there was an excellent

agreement with the concentrations found by mass spectrometric analysis (Table 4.1).

Table 4.1: *Tissue specific parameters obtained by measuring ZFC/FC-susceptibility at 1000 Oe according to Eq. 4.7 and the corresponding iron content assessed by mass spectroscopy.*

| Sample | Curie Constant C (emu K/g/Oe) | Paramagnetic Curie temperature $\Theta$ (K) | Diamagnetic background $\chi_{Dia}$ (emu/g/Oe) | iron-content SQUID Cfe ($\mu$g/g) | Iron-content Mass spectroscopy ($\mu$g/g) |
|---|---|---|---|---|---|
| White matter #1 | $(1.58 \pm 0.08)$ 10-6 | $-0.9 \pm 0.2$ | $(-4.57 \pm 0.03)$10-7 | $23.6 \pm 0.5$ | $26.6 \pm 1.9$ |
| White matter #2 | $(2.12 \pm 0.03)$ 10-6 | $-1.4 \pm 0.2$ | $(-5.93 \pm 0.02)$ 10-7 | $31.5 \pm 0.5$ | $31.6 \pm 2.3$ |
| Cortex | $(2.44 \pm 0.11)$ 10-6 | $-3.0 \pm 0.25$ | $(-3.21 \pm 0.04)$ 10-7 | $36.3 \pm 0.5$ | $37.9 \pm 2.8$ |

### 4.4.3 MRI

As shown in Figure 4.2, temperature induced contrast changes on $R'_2$ maps were moderate with a more pronounced contrast at lower temperatures. The transverse relaxation rate
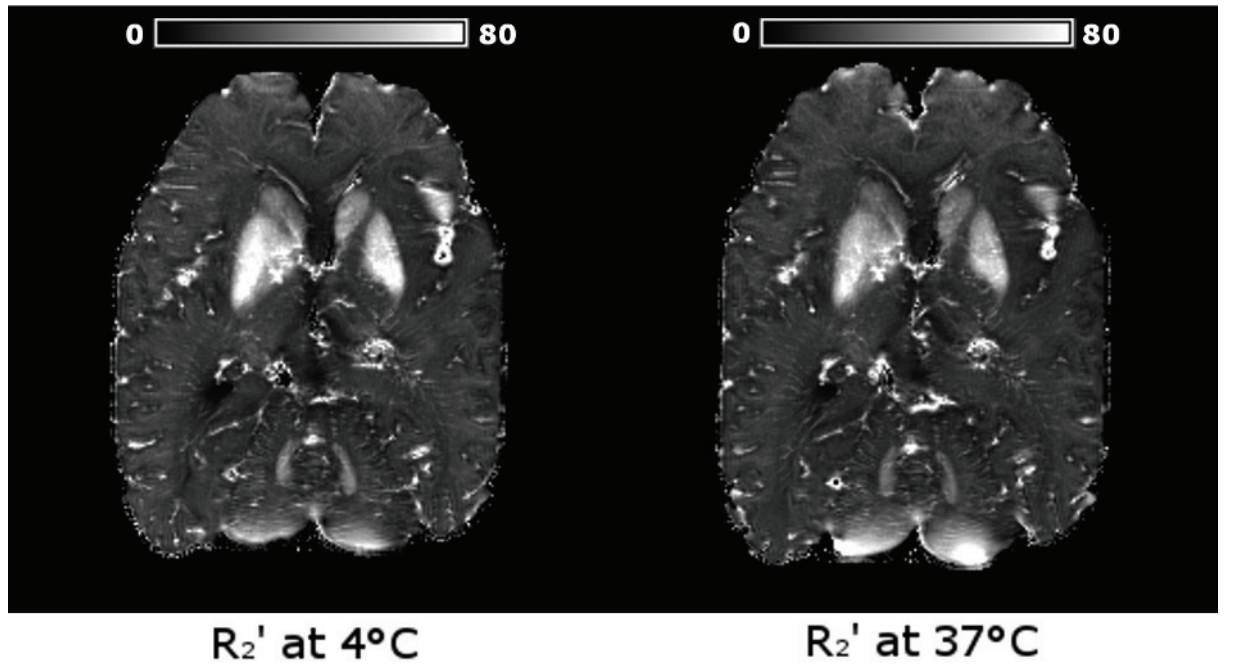


Figure 4.2: *$R'_2$ map of a fresh and unfixed brain acquired at 4 ℃(left) and 37 ℃(right). Artifacts from air inclusions were more prominent at high temperatures.*

$R'_2$ (Figure 4.3) of all five brain slices showed a linear decrease with increasing tissue temperature. The strongest temperature dependency of $R'_2$ ($s^{-1}$) was observed in the basal ganglia ($R'_2 = 49.46 – 0.55 \cdot \vartheta$) where $\vartheta$ is the temperature in ℃. White matter showed a lower temperature dependency ($R'_2 = 12.71 – 0.04 \cdot \vartheta$) compared to the cortex
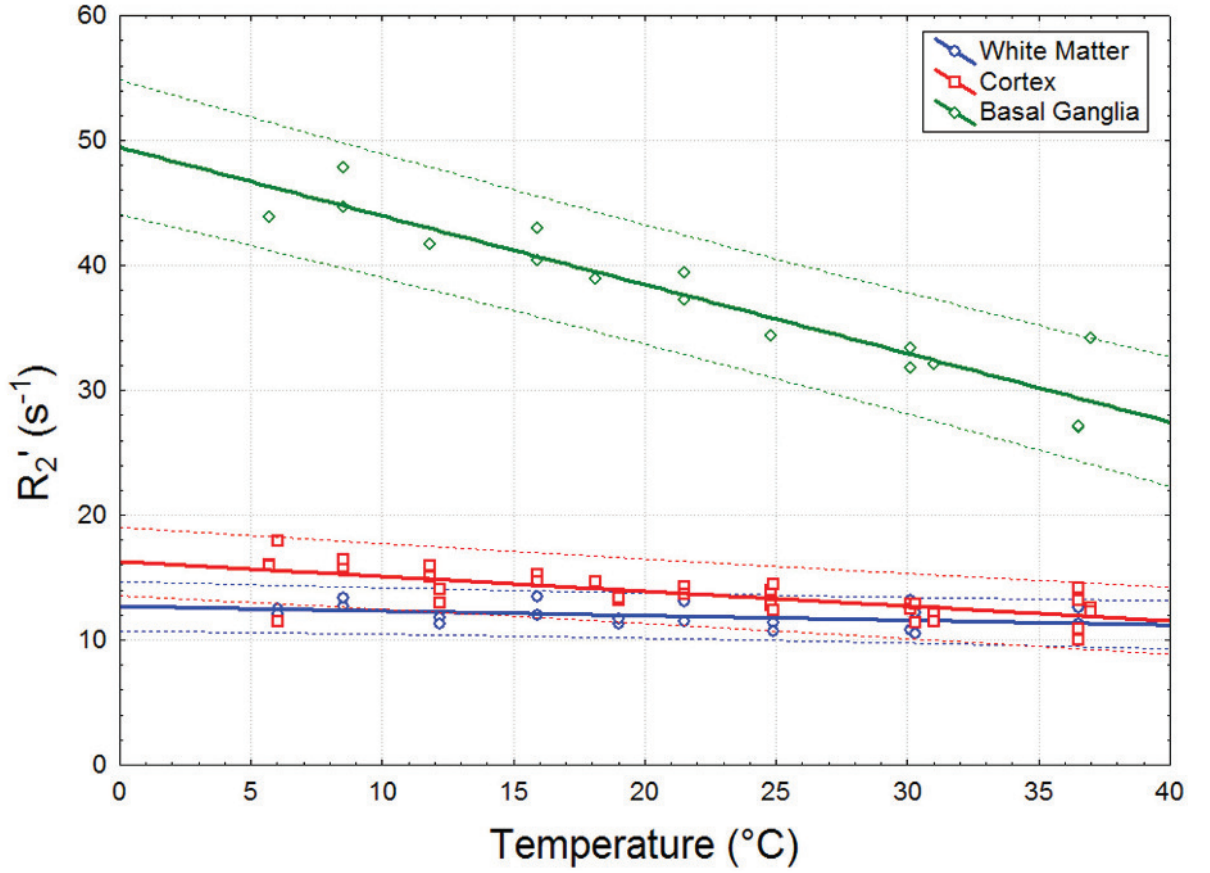
Figure 4.3: $R_2'$ in different brain regions as a function of temperature. Data from 12 regions of five brains are shown.

$(R_2' = 16.29\text{--}0.12 \cdot \vartheta)$. Regions with high iron concentrations appear bright in the $R_2'$ map and in the TcR2p map (Figure 4.4). The low contrast between white matter and the cortex reflects a very small difference in iron concentration between these structures. There was a good agreement between $R_2'$ estimated from SQUID data (Figure 4.5 a) and $R_2'$ measured by MRI (Figure 4.5 b) in the temperature range between $4\,°C$ and $37\,°C$. While $R_2'$ estimated from SQUID was significantly higher, there was an excellent agreement of the slopes in both graphs. SQUID magnetometry of the three samples revealed a slope of -0.0452 in the cortex and -0.0297 and -0.0398 in white matter, respectively. The corresponding TcR2p values determined in MRI were -0.0583 s$^{-1}$T$^{-1}$ in the cortex and -0.0375 s$^{-1}$T$^{-1}$ and -0.0396 s$^{-1}$T$^{-1}$ in white matter. The results for all regression analyses with absolute iron concentration are summarized in Table 4.2. While $R_2'$ was only a moderate marker for iron content in white matter, the temperature coefficient of
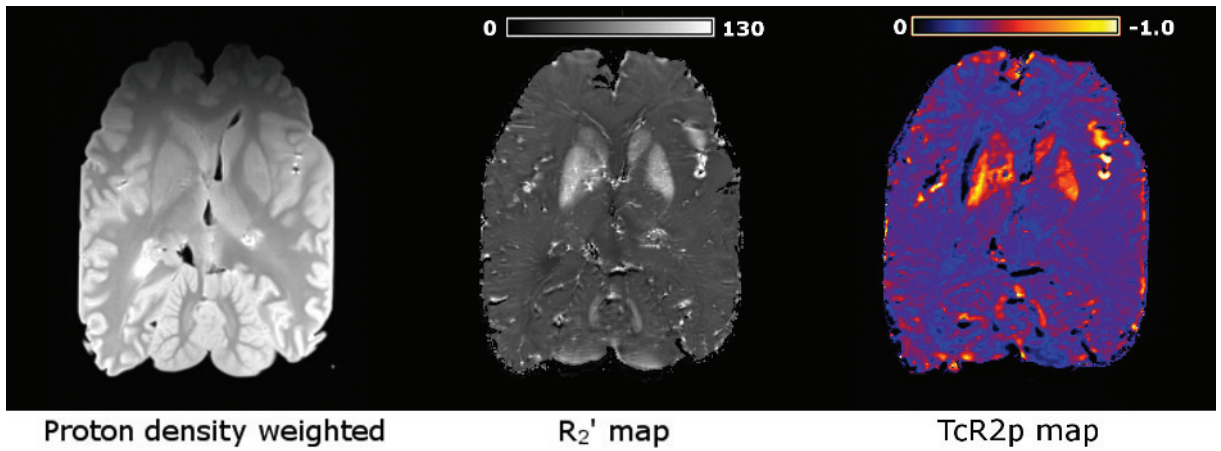
Figure 4.4: *Proton density weighted image (left), $R'_2$ map (middle) obtained at $\approx$ 20 °C, and color encoded temperature coefficient map (right), all corresponding to the brain slice shown in Figure 4.2. Iron and temperature related relaxivity changes are clearly visible in the putamen, caudate nucleus, and dentate nucleus. Please note that some temperature effects arise from residual air inclusions at the surface of the brain.*
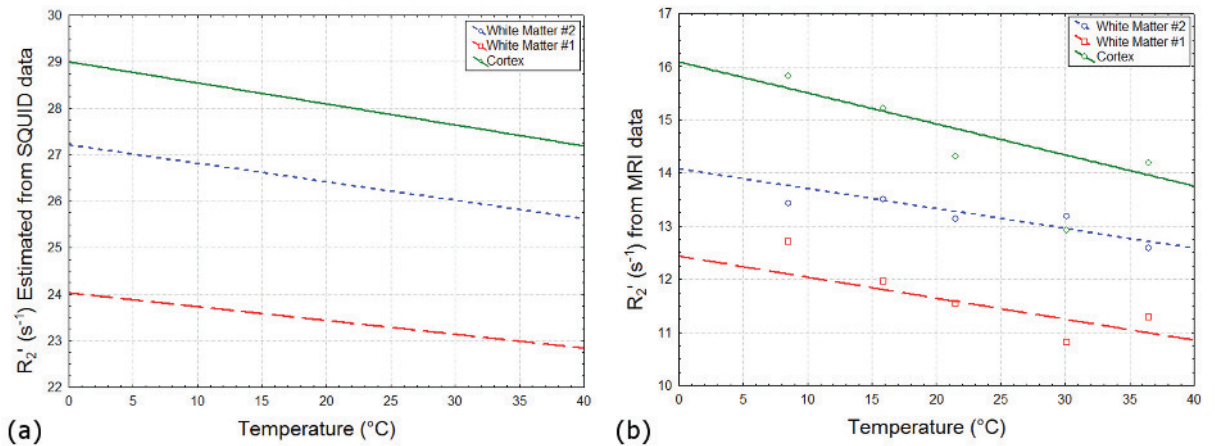


Figure 4.5: *Temperature dependent $R'_2$ estimated from SQUID data (a) and corresponding $R'_2$ of three samples from a single brain slice determined by MRI (b).*

$R'_2$ (TcR2p) was highly correlated with iron content ($r^2 = 0.97$) (Figure 4.6).

## 4.5 Discussion

Assessment of iron concentration in white matter or tissues with a strong diamagnetic background is still an unresolved challenge. We here propose to use the temperature coefficient of $R'_2$ as a measure of iron. Using fresh postmortem brain, the new concept was

Table 4.2: *Linear regression analysis of the transverse relaxation rate $R_2'$ and the temperature coefficient of $R_2'$ (TcR2p) as a function of iron (mg/kg wet mass).*

| Structure | r2 | P Value | $R_2'$ (s-1) Regression | Std. error Slope | $r^2$ | P Value | TcR2p ($s^{-1}$/°C) Regression | Std. error Slope |
|---|---|---|---|---|---|---|---|---|
| All structures | 0.94 | <0.001 | 8.85+0.11 x Fe | 1.507 | 0.98 | <0.001 | 0.030-0.004 x Fe | 0.035 |
| White Matter only | 0.84 | 0.08 | -0.87+0.43 x Fe | 1.048 | 0.97 | 0.01 | 0.084-0.005 x Fe | 0.004 |
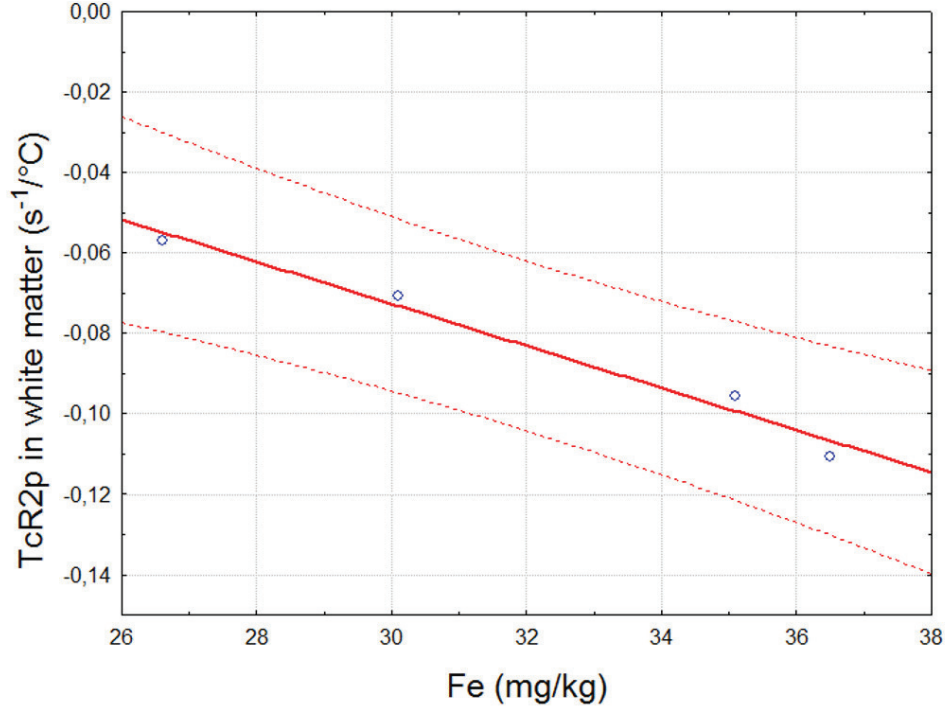


Figure 4.6: *Linear relationship between the temperature coefficient of $R_2'$ (TcR2p) and the absolute iron concentration (in mg/kg wet mass) in white matter as measured by inductive coupled plasma mass spectrometry*

evaluated with SQUID data and validated with mass spectrometry.

While rat brain [176] has been investigated with SQUID recently, we here present magnetic susceptibility profiles for human brain white and gray matter along with corresponding Curie constants and Curie temperatures. These data may contribute to a better understanding of the magnetic behavior of brain tissue.

Bulk susceptibility and $R_2'$ rates represent different measures of susceptibilities. While the bulk susceptibility can be considered as a volume average, $R_2'$ represents the dephasing effect due to susceptibility variations in a volume, where diamagnetic and paramagnetic compounds have the same effect. We roughly estimated $R_2'$ from SQUID data by

taking the susceptibility difference between water and the iron paramagnetism found by the SQUID analysis. Overall, we found an overestimation of $R'_2$ values which may have several causes. By setting $\lambda$ to 1 we did not account for geometric effects and we did also not consider orientational effects of $R^*_2$ [177]. Some offset may also have been introduced by an overestimation of $R_2$ which was derived from a TSE sequence [96] because of time constraints. However, all these effects did not affect the temperature dependency of $R'_2$ and we could clearly demonstrate that the temperature dependent slope was the same for the SQUID measurements and for $R'_2$.

Another important finding was that the iron content derived from the temperature dependent susceptibility profiles was in good agreement with the values obtained by mass spectroscopy. This confirms that iron is the major source of paramagnetism in brain tissue as already predicted by Schenck [160] and that iron is also responsible for the temperature dependency of $R'_2$.

A specific feature that we have observed only in the SQUID measurements was noticed in the cortex, where we found a bifurcation of the ZFC/FC-susceptibility curves near 12 K. We interpret this splitting as an onset of mineralization of iron into a small core of iron-oxide ($\gamma$-maghemite or magnetite). The blocking temperature as observed from the maximum of the ZFC-curve agrees with the temperature reported for ferritin [178]. As we made this observation in grey matter only, it seems that different iron configurations are present in white matter. Further investigations with SQUID magnetometry are needed to understand how iron is distributed and stored in white matter.

Using brain tissue with a short post mortem delay (<24h) between death, autopsy and image acquisition allows us to neglect autolysis effects. We showed in a previous work that relaxation times of unfixed brain tissue with short postmortem delay are comparable with in vivo values [140].

The benefit of our proposed method is the ability of determining the iron quantitatively and without destruction of the tissue sample compared to the standard histopathology. It is clearly not possible to change brain temperature in vivo, therefore the clinical applicability of the proposed approach remains limited. However, when working with postmortem tissue it could open new avenues to study the role of iron in various inflammatory and neurodegenerative diseases.

## Acknowledgements

**5**

# Effects of formalin fixation and temperature on MR relaxation times in the human brain

Christoph Birkl[1], Christian Langkammer[1,2], Nicole Golob-Schwarzl[3], Marlene Leoni[3], Johannes Haybaeck[3], Walter Goessler[4], Franz Fazekas[1] and Stefan Ropele[1]

[1] Department of Neurology, Medical University of Graz, Austria

[2] MGH Athinoula A. Martinos Center for Biomedical Imaging, Department of Radiology, Harvard Medical School, Boston, MA, USA

[3] Department of Neuropathology, Institute of Pathology, Medical university of Graz, Austria

[4] Institute of Chemistry, Analytical Chemistry, University of Graz, Austria

## 5.1 Introduction

Post-mortem MRI is an indispensable tool to improve our understanding of relaxation mechanisms in normal and abnormal tissue on a microscopic level and to validate quantitative MRI methods [22, 28, 46, 110, 156, 167, 179, 180]. Additionally, tissue samples permit very long scanning times which is a prerequisite for MR microscopy [181]. Very recently, it was also demonstrated that fixed human brain tissue can serve as a reliable model for standardization in multicenter studies [182].

An ideal post-mortem MRI investigation would be at a condition where cells and tissue components are preserved in a "life-like" state. However, autolysis starts as soon as a tissue is deprived of its blood supply and results in tissue digestion by intracellular enzymes, which are released when organelle membranes rupture. Fixation is an approach to largely protect against this decay process. Among various chemical fixatives, phosphate buffered formalin is the most frequently used fixate in routine histopathology [183]. It has been reported that formalin fixation significantly reduces $T_1$ and $T_2$ relaxation times but the exact mechanisms involved are yet unknown[184–187]. Formaldehyde reacts with water to form methylene glycol and methylene glycol interacts with protein side chains. This leads to crosslinking between the proteins through methylene bridges[188]. Thus, it has been speculated that the reduction of relaxation times originates from formalin induced dehydration [189], crosslinking [184, 190] and reduced transmembrane water exchange [187, 191], but the actual cause and the magnitude of the concomitant $T_1$ and $T_2$ changes have not been investigated systematically, so far.

Previous work has focused on single aspects of post-mortem MRI such as the effect of the post-mortem interval [134], temperature [140, 141, 143], incomplete fixation [184, 187], different embedding media [192, 193] and the optimization of post-mortem MR parameters [144]. However, most of these studies used small tissue samples or non-human brain samples at lower field strengths and do not provide formalin induced relaxation changes in absolute terms.

We here aimed at studying the effect of formalin fixation in a more comprehensive way by assessing the magnitude and origin of $T_1$, $T_2$ and $T_2^*$ changes as a function of temperature, water content, and macromolecular size of proteins. Regions were defined in white matter (WM), cortical gray matter (GM), thalamus (TH) and in the basal ganglia

(BG) of human brain to evaluate possible variations caused by tissue microstructure and to enable a comparison with previous studies.

## 5.2 Experimental

### 5.2.1 Relaxation time mapping of unfixed and fixed brain samples

To investigate the effect of formalin on the MR relaxation times and their temperature dependency, brain slices from five deceased subjects (3 male, 2 female) aged between 53 and 88 years (mean age = 70 years) and without a history of a neurological disease were used. The entire brain was extracted at autopsy following a request by the local health authorities, and cut into 10 mm-thick coronal slices. One slice of each brain was further used for MRI acquisition with a time between death and MRI in a range between 24 to 44 hours. The brain slices were embedded in agar gel (14 g/l), vacuum packed and mounted in the center of a plastic sphere. The sphere was flooded with water at a controlled temperature until the temperature was stabile for MRI acquisition. The temperature was measured at the surface of the brain sample during the whole experiment using a LUX-TRON 790 Fluoroptic Thermometer (LumaSense Technologies, Santa Clara, CA, USA).

MRI was performed at 6 different temperatures between 4 °C and 37 °C on a 3 T whole body MRI system (Magnetom Tim Trio, Siemens Healthcare, Erlangen, Germany) using a 12 channel head coil array. For each predefined temperature a set of sequences, with a total scan time of approximately 15 min was applied. Sequences were optimized with respect to acquisition time to avoid temperature drifts during MRI. All sequences were performed with the same geometrical settings of FOV = 192 × 192 mm$^2$, matrix = 256 × 256, number of slices = 7, slice thickness = 3 mm, and parallel imaging with GRAPPA using an acceleration factor of 2. $T_1$ relaxometry was performed using a turbo inversion recovery (TIR) sequence with 4 inversion times (TI = 200, 800, 1600, 3200 ms) and TE/TR = 6.4/8000 ms. A turbo spin echo (TSE) sequence with three echoes times (TE = 10, 73, 115 ms) and a TR of 4000 ms was used to assess the $T_2$ relaxation time. For $T_2^*$ relaxometry, a 2D RF spoiled gradient echo (GRE) sequence was used with 6 echoes (TE = 4.92, 10.34, 15.76, 21.18, 26.60, 32.02 ms), TR = 300 ms and a flip angle of 15°.

After MRI of the unfixed samples the agar gel was removed and the brain slices were fixed with 4 % formaldehyde solution for approximately 190 days and stored at room

temperature (22 °C) to achieve a constant fixation as plateauing is reached after 150 days [185]. Following fixation, the samples were washed with water for some seconds and MRI was repeated using exactly the same procedures.

To compare unfixed MRI at 37 °C with in-vivo values, three control patients with a mean age of 68 years were scanned with the identical protocol used for post-mortem MRI.

## 5.2.2 Image processing

Image analysis was performed using MATLAB (The MathWorks, Natick, MA, USA) and linear regression analysis using STATISTICA Version 7.1 (StatSoft, Tulsa, OK).

Relaxation time constants were fitted assuming mono-exponential relaxation and were assessed in white matter, cortical grey matter, basal ganglia and thalamus of each brain slice in unfixed and fixed conditions. Identical regions of interest (ROIs) were selected for comparison between unfixed and fixed tissue as shown in Figure 2. For assessing the temperature dependency of the relaxation times, the intercept $T_0$ and the temperature coefficient $T_C$ of the relaxation times $T_1$, $T_2$, $T_2^*$ were calculated using a linear regression model ($T_i = T_{i,0} + T_{i,C} \cdot \varphi$, with $\varphi$ the temperature in °C). Not all samples could be acquired at exactly the same temperature. Therefore, for a better comparison with in vivo values, the relaxation times of the fixed and unfixed tissue were calculated for 37 °C and 22 °C using the results from the regression analysis. The significance of relaxation time changes between fixed and unfixed state was tested with a paired t-test.

## 5.2.3 Water Content Measurements

The change of water content due to formalin fixation was determined by excising samples of different regions (white matter, cortex, basal ganglia and thalamus) from one additional unfixed human brain without neurological disease (age = 75 years) with a post-mortem delay of less than 24 hours. All samples were approximately 1 cm$^3$ and divided into two subsamples and weighted. In the next step, one subsample of each region was stored at −80 °C while the other was fixed in a 4 % formaldehyde solution. Based on the small sample volume and a penetration speed of 0.5-1 mm/h [194], 10 days of formalin fixation were felt to be sufficient to achieve a fully fixed condition. The unfixed and fixed samples were freeze-dried in a Gamma 1-16 LSC freeze-dryer (Martin Christ Gefriertrocknungsanlagen GmbH, Germany). After freeze-drying the water content (WC) was calculated with WC = 100 × (mwet - mdry)/mwet where mwet is the weight of the wet sample and mdry

the weight of the dry sample. After calculating this interim WC result all samples were heated in an oven at 60 °C for additional 17 hours. The dried samples were weighted again to calculate the wet-to-dry mass ratio and the water content after the additional oven-drying. For comparison of the water content of the unfixed and fixed samples an independent t-test was used.

## 5.2.4 Assessment of macromolecular size

To study the effect of covalent linking of proteins induced by crosslinking and the corresponding increase in molecular weight on relaxation rates, sodium dodecyl sulfate polyacrylamide gel electrophoresis (SDS-PAGE) was performed using brain tissue of an 2nd additional human brain without history of neurological disease (age = 66 years) and a post-mortem delay less the 24 hours. Samples were excised and processed from regions that exactly matched the regions for the water content measurements.

For protein extraction, the samples were mixed with 400 $\mu$l of NP-40 lysis buffer (0.05 mol Tris-HCl, 0.15 mol NaCl, 0.5 % NP-40, 0.001 mol Pefabloc, 0.001 mol DTT, complete Mini, PhosSTOP). The tissue samples were homogenized with a Potter tissue homogenizer (MagNA Lyser, Roche Diagnostics, Switzerland) at 6500 rpm for 30 sec. Then, the samples were centrifuged at 10,000 rpm for 10 min at 4 °C. The supernatant was transferred to a 1.5 ml reaction tube. Subsequently the supernatant was directly subjected to protein quantification and stored at $-80$ °C until SDS-PAGE analysis was performed. Protein quantification was performed using the Bio-Rad Protein Assay (Bio-Rad Laboratories GmbH, Munich, Germany). Therefore, 998 $\mu$l of the working solution was added to 2 $\mu$l protein lysate and incubated for 15 min at 25 °C. Absorbance was determined at a wavelength of 595 nm using a BioSpectrometer (Eppendorf, Germany). The protein concentration was determined based on a bovine serum albumin standard curve (Roche, Germany) ranging from 0 to 10 mg/ml. An 8 % SDS gel (30 % Acrylamid/Bisacrylamid solution from ROTH) was loaded with 30 $\mu$g total protein and subjected to electrophoresis in Mini-vertical electrophoresis units (Amersham Biosciences, UK). For an overall detection of all proteins the gel was stained with Coomassie Brilliant Blue G250 (Bio-Rad Laboratories GmbH, Munich, Germany).

## 5.3 Results

In the unfixed tissue, $T_1$ showed a strong temperature dependency between 3.4 – 17.4 ms/°C while $T_2$ showed only a moderate temperature dependency between -0.2 – 0.3 ms/°C in all regions. $T_2^*$ was affected by temperature only in the basal ganglia and thalamus. The temperature coefficient values of the unfixed tissue are published in previous work [140]. Overall, formalin fixation reduced the temperature coefficient of $T_1$ (Figure 5.1) and increased the temperature coefficient of $T_2$ in all regions.

The temperature coefficient of $T_2^*$ was increased in the basal ganglia and thalamus only
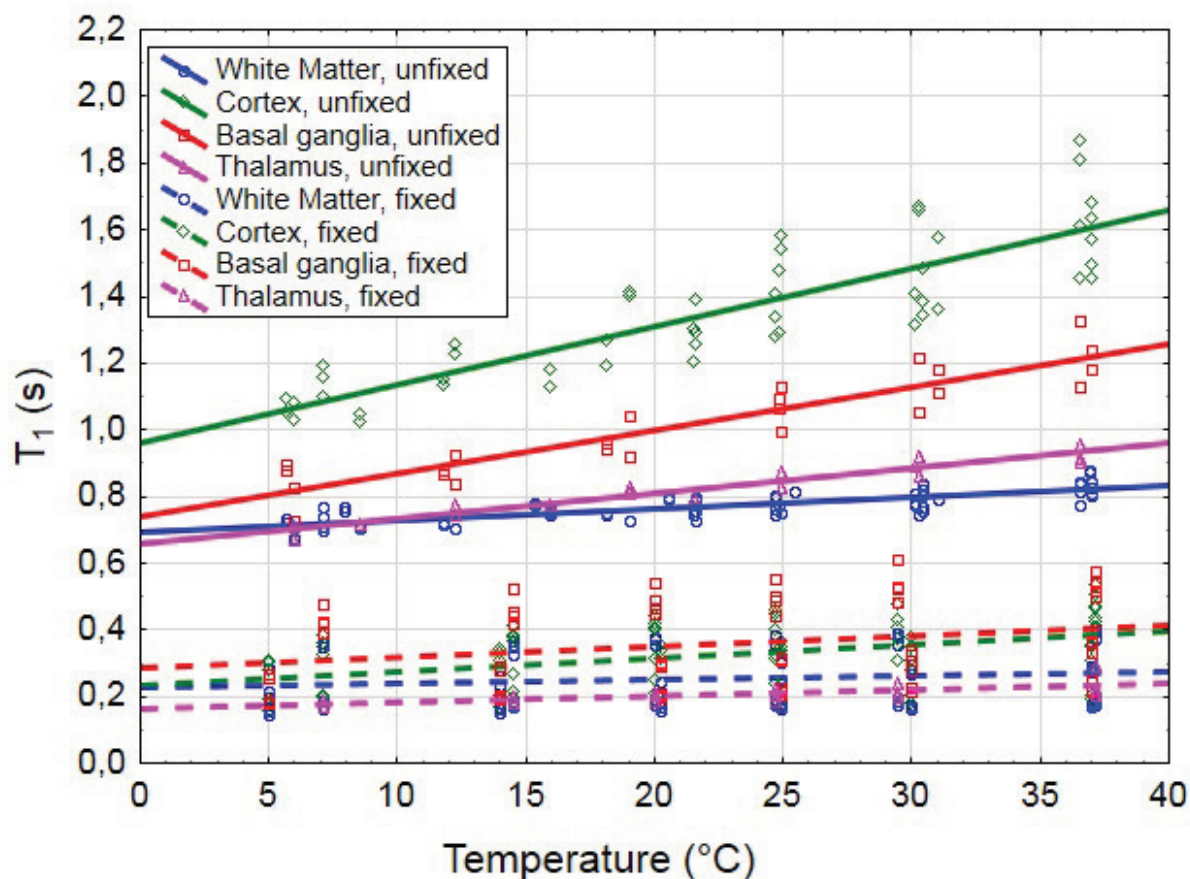


Figure 5.1: *Longitudinal $T_1$ relaxation time versus temperature in white matter, cortex, basal ganglia, and thalamus of unfixed and fixed brain samples. Solid lines represent the unfixed tissue and dashed lines the fixed tissue $T_1$ times.*

while it remained unchanged within standard deviation in white matter and cortex. The temperature coefficients and intercepts for all relaxation time constants for unfixed and fixed conditions are summarized in Table 5.1.

To consider the effects of both, formalin fixation and temperature induced changes, relaxation times of the unfixed and fixed tissue were compared at 37 °C. Additionally, to rule out any relevant autolysis effects, these values were compared with in-vivo values at 37 °C using the same sequence parameters. The in-vivo values and unfixed values at 37 °C were comparable within standard deviation. Additionally the relaxation times of unfixed tissue at 37 °C and fixed tissue at 22 °C were compared to assess differences that commonly can be observed in most post-mortem imaging situations. As summarized in Table 5.2, fixation without temperature influence caused a decrease of all relaxation times with the strongest effect observed for $T_1$. $T_1$ was reduced about 67 % in white matter, 76 % in the cortex, 67 % in the basal ganglia, and 75 % in the thalamus. The fixation induced decrease of relaxation times at 37 °C was statistically significant for $T_1$ (p <0.001), $T_2$ (p <0.001) and $T_2^*$ (p = 0.001). When post-mortem tissue is scanned at room temperature, the temperature coefficient contributes to an additional decrease of the relaxation times. Consequently, the difference in relaxation times between unfixed state at 37 °C and fixed state at 22 °C was significant for $T_1$ (p <0.001), $T_2$ (p <0.001) and $T_2^*$ (p <0.001).

The most evident macroscopic effects of 190 days formaldehyde fixation are shrinking of the tissue and a change of the grey-white matter contrast. Although shrinking suggested a loss of water, overall fixation caused only a moderate decrease of the water content compared to unfixed tissue. For the unfixed samples, oven-drying had no additional affect over freeze-drying while in the fixed samples oven-drying further reduced residual water and therefore provided a smaller apparent dry mass. An apparent reduction of the dry mass corresponds to an initially higher water content as shown in Figure 5.2. After both, freeze-drying and oven-drying, a mean decrease (± standard error) of water content of −2.7 % (±1.4) in white matter, 0.7 % (±1) in the cortex, −1.6 % (±0.6) in the basal ganglia and −4.3 % (±0) in the thalamus, was observed. The water content of the unfixed and fixed brain samples is summarized along with values reported in literature in Table 5.2. The water content of the unfixed samples was in good agreement with results published by Cummings [195].

All unfixed samples showed a distribution of molecular weight over the whole range between 10-260 kDa (Figure 5.4). The protein weights of formalin fixed samples were greater than 260 kDa, only visible at the loading slot, and inseparable on the gel, which clearly

reflects crosslinking of the proteins to larger complexes.

Table 5.1: *Results of the linear regression model describing the relaxation time constants as a linear function of the temperature coefficient ($T_C$) and intercept ($T_0$) for different brain regions in unfixed and fixed conditions. Statistically significant results ($p < 0.05$) are highlighted in bold. R is the Pearson's correlation coefficient of the linear regression analysis.*

|  |  |  | $T_0$ (ms) | $T_C$ (ms/°C) | $R^2$ | p value | SE slope (%) |
|---|---|---|---|---|---|---|---|
| | Unfixed | $T_1$ | 695.8 ± 29.2 | 3.4 ± 0.7 | 0.91 | 0.007 | 0.031 |
| | Fixed | $T_1$ | 230.6 ± 82.6 | 1.1 ± 0.7 | 0.74 | 0.041 | 0.008 |
| White Matter | Unfixed | $T_2$ | 91.2 ± 17.4 | -0.2 ± 0.2 | 0.35 | 0.299 | 0.016 |
| | Fixed | $T_2$ | 58.4 ± 13.6 | 0.1 ± 0.2 | 0.53 | 0.176 | 0.002 |
| | Unfixed | $T_2^*$ | 36.5 ± 6.6 | 0.1 ± 0.1 | 0.58 | 0.192 | 0.007 |
| | Fixed | $T_2^*$ | 24.9 ± 4.7 | 0.1 ± 0.1 | 0.31 | 0.205 | 0.003 |
| | Unfixed | $T_1$ | 962 ± 67.7 | 17.4 ± 5.3 | 0.97 | 0.002 | 0.149 |
| | Fixed | $T_1$ | 232.7 ± 91.4 | 4.1 ± 2.5 | 0.90 | 0.005 | 0.07 |
| Cortex | Unfixed | $T_2$ | 132.1 ± 23 | 0.2 ± 0.7 | 0.33 | 0.319 | 0.030 |
| | Fixed | $T_2$ | 64.8 ± 14.7 | 1.6 ± 0.7 | 0.97 | 0.001 | 0.012 |
| | Unfixed | $T_2^*$ | 39.3 ± 10 | 0.2 ± 0.3 | 0.56 | 0.171 | 0.019 |
| | Fixed | $T_2^*$ | 26 ± 8.9 | 0.2 ± 0.2 | 0.63 | 0.097 | 0.01 |
| | Unfixed | $T_1$ | 738.5 ± 52.2 | 13.1 ± 2.4 | 0.96 | <0.001 | 0.116 |
| | Fixed | $T_1$ | 285.6 ± 112.1 | 3.1 ± 1.1 | 0.90 | 0.004 | 0.094 |
| Basal Ganglia | Unfixed | $T_2$ | 84.7 ± 27.7 | 0.3 ± 0.2 | 0.54 | 0.133 | 0.038 |
| | Fixed | $T_2$ | 49.5 ± 11 | 1.1 ± 0.3 | 0.99 | <0.001 | 0.013 |
| | Unfixed | $T_2^*$ | 31.9 ± 11.9 | 0.2 ± 0.1 | 0.91 | 0.003 | 0.023 |
| | Fixed | $T_2^*$ | 17.9 ± 5.8 | 0.3 ± 0.2 | 0.91 | 0.013 | 0.007 |
| | Unfixed | $T_1$ | 656.8 ± 11.9 | 7.6 ± 0.4 | 0.97 | <0.001 | 0.053 |
| | Fixed | $T_1$ | 165.1 ± 12.4 | 1.8 ± 1.2 | 0.92 | 0.002 | 0.006 |
| Thalamus | Unfixed | $T_2$ | 82.1 ± 26.7 | 0.2 ± 0.2 | 0.33 | 0.352 | 0.050 |
| | Fixed | $T_2$ | 55.4 ± 3.6 | 0.8 ± 0.3 | 0.99 | <0.001 | 0.002 |
| | Unfixed | $T_2^*$ | 41.5 ± 5.8 | 0.3 ± 0.1 | 0.79 | 0.033 | 0.011 |
| | Fixed | $T_2^*$ | 29.4 ± 5.4 | 0.4 ± 0.1 | 0.90 | 0.004 | 0.007 |

## 5.4 Discussion and Conclusion

From a chemical point of view, formaldehyde ($CH_2O$) reacts with water ($H_2O$) to form methylene glycol ($HO(CH_2OH)_n$) leading to a low concentration of free formaldehyde in the fixation solution. The chemical reaction of formaldehyde with tissue components can be separated into two stages [183, 188, 196, 197]. In the first stage, formaldehyde is penetrating the tissue and is reacting with amino acid side groups of proteins (e.g. lysine
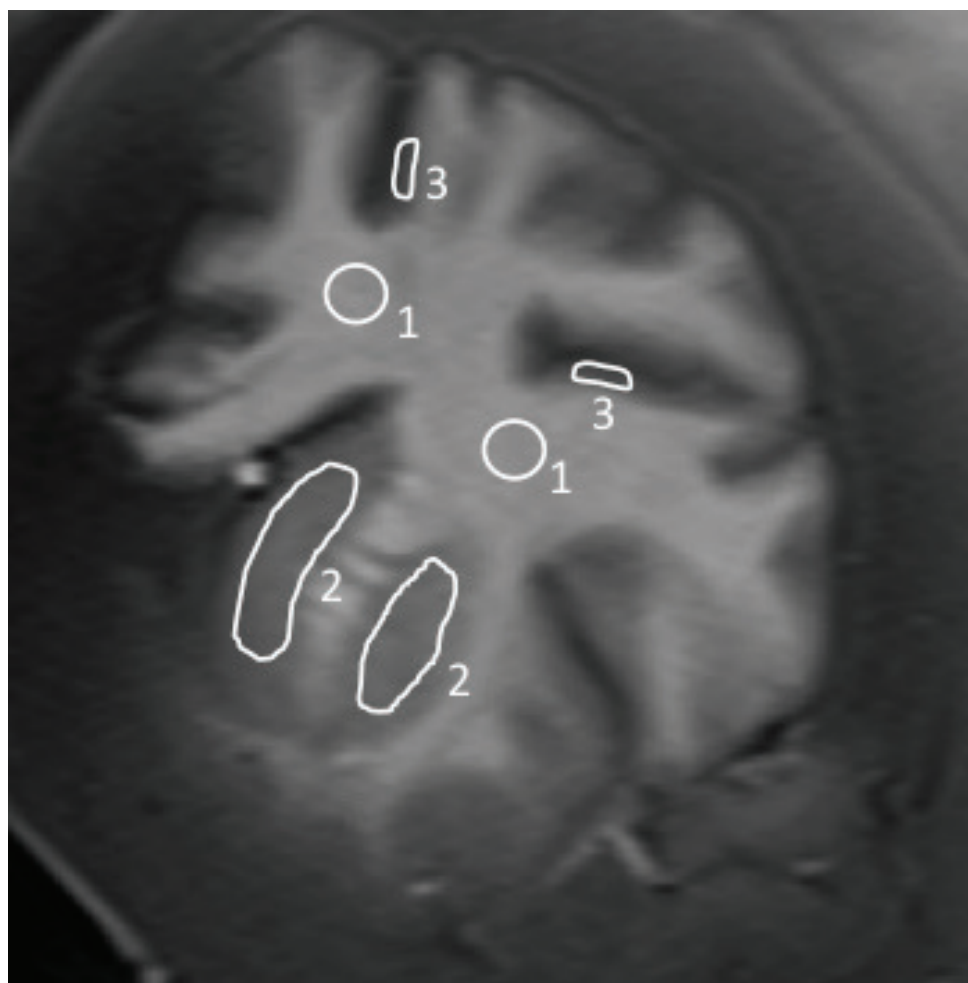
*Figure 5.2: Unfixed coronal brain slice acquired with a turbo inversion recovery. Representative ROIs are shown for (1) white matter, (2) basal ganglia, and (3) cortex.*

side-chain) by forming hydroxymethylene groups ($CH_2OH$). This first reaction step can be reversed by washing the tissue in water. Beside rapid penetration of formaldehyde and methylene glycol, based on the low molecular weight, the second stage of the chemical reaction is quite slow. When two binding sites are sufficiently close, a methylene bridge ($-CH_2-$) is built and the corresponding proteins are linked together. During this crosslinking, large protein complexes are formed and the permeability of the microstructure is reduced. The penetration and rate of crosslinking does not exclusively depend on the fixation time, but also on the temperature at which the fixation takes place. A higher temperature allows a better fixation result in terms of hardening and less shrinking of the tissue [183].

Table 5.2: *Relaxation times of the unfixed and fixed brain tissue for in-vivo conditions (37 °C) and for room temperature (22 °C). Relaxation times of three age matched in-vivo controls are reported as comparison. Mean values ± standard deviation are provided.*

| tissue | relaxation time | in-vivo at 37 °C (ms) | unfixed at 37 °C (ms) | fixed at 37 °C (ms) | fixed at 22 °C (ms) | fixation induced decrease (%) | fixation and temperature induced decrease (%) |
|---|---|---|---|---|---|---|---|
| White Matter | $T_1$ | $885.8 \pm 76.8$ | $821.6 \pm 55.1$ | $271.3 \pm 108.5$ | $254.8 \pm 9$ | 67.0 | 69.0 |
| | $T_2$ | $89.7 \pm 5.9$ | $83.8 \pm 24.8$ | $62.1 \pm 21$ | $60.6 \pm 2$ | 25.9 | 27.7 |
| | $T_2^*$ | $45.6 \pm 6.0$ | $40.2 \pm 10.3$ | $28.6 \pm 7.4$ | $27.1 \pm 6.9$ | 28.7 | 32.6 |
| Cortex | $T_1$ | $1444.6 \pm 266.1$ | $1605.8 \pm 263.8$ | $384.4 \pm 183.9$ | $322.9 \pm 146.4$ | 76.1 | 79.9 |
| | $T_2$ | $110.6 \pm 24.4$ | $139.5 \pm 48.9$ | $124 \pm 40.6$ | $100 \pm 30.1$ | 11.1 | 28.3 |
| | $T_2^*$ | $65.3 \pm 10.1$ | $46.7 \pm 21.1$ | $33.4 \pm 16.3$ | $30.4 \pm 13.3$ | 28.5 | 34.9 |
| Basal Ganglia | $T_1$ | $1220.7 \pm 72.0$ | $1223.2 \pm 141$ | $400.3 \pm 152.8$ | $353.8 \pm 136.3$ | 67.3 | 71.1 |
| | $T_2$ | $88.0 \pm 10.4$ | $95.8 \pm 35.1$ | $90.2 \pm 22.1$ | $73.7 \pm 15.4$ | 5.9 | 23.1 |
| | $T_2^*$ | $37.3 \pm 8.3$ | $39.3 \pm 15.6$ | $29 \pm 13.2$ | $24.5 \pm 10.2$ | 26.21 | 37.7 |
| Thalamus | $T_1$ | $1096.6 \pm 73.5$ | $938 \pm 26.7$ | $231.7 \pm 56.8$ | $204.7 \pm 38.8$ | 75.3 | 78.2 |
| | $T_2$ | $100.4 \pm 10.0$ | $89.5 \pm 34.1$ | $85 \pm 14.7$ | $73 \pm 10.2$ | 5.0 | 18.4 |
| | $T_2^*$ | $51.7 \pm 3.4$ | $52.6 \pm 5.8$ | $44.2 \pm 9.1$ | $38.2 \pm 7.6$ | 16.0 | 27.4 |

This study confirms previous reports of reduced relaxation times in fixed tissues but showed a difference in their magnitude [186, 190]. Here, the examination of the same tissue samples at two different conditions and at several temperatures, allowed to measure the fixation and temperature induced changes precisely and relate them to changes in molecular structure and water content. The biggest change was observed for $T_1$ with variations in different brain compartments. $T_1$ relaxation reflects the efficiency of the energy transfer between excited spins and their molecular surrounding. The correlation time for energy exchange is strongly determined by the viscosity, the water content, and by the size of the interacting molecules. Our results suggest that dehydration, which is a well-known consequence of crosslinking, does not play a major role for the observed $T_1$ shorting. The biggest $T_1$ drop was seen in the cortex, however the corresponding change in water content was only 1 %. In white matter, the water content was reduced by approximately 4 % which can explain at maximum a 15 % drop of $T_1$ based on the reported relationship between water content and $T_1$ [198, 199] instead of the 67 % of $T_1$ reduction found in this study. According to relaxation theory, T1 is depending on the radius of the molecules, the distance between the spins in a molecule and the viscosity of a medium [89]. Our results from SDS-PAGE therefore suggest that $T_1$ shortening is mostly caused by changes in the macromolecular structure as a consequence of cross-linking.

A linear dependency of the $T_1$ relaxation time on temperature is in line with literature [89, 141] and was observed in the unfixed and to a lower extent in the fixed brain. One could hypothesize, that the reduced temperature dependency of the fixed brain comes from the increased viscosity which is related to the water content and cross-linking of
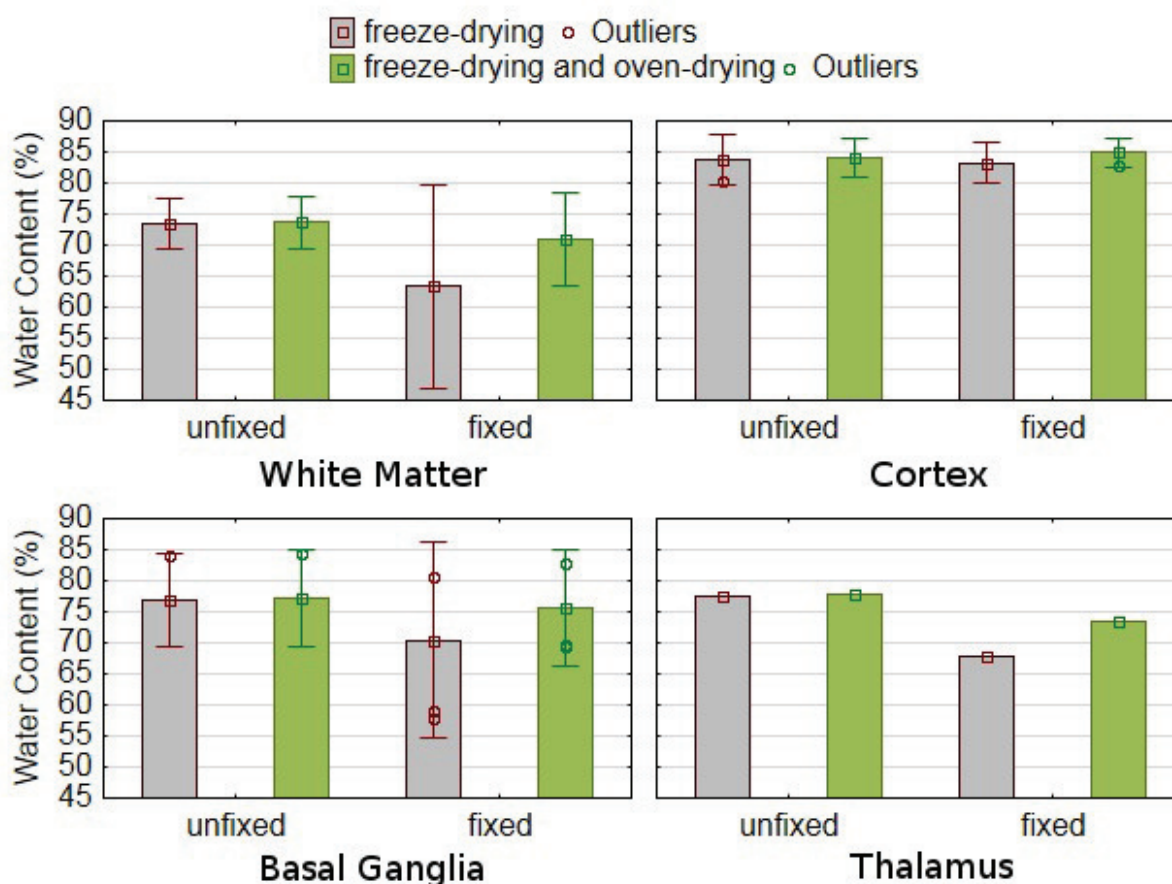
Figure 5.3: *Water content of different brain regions determined by freeze-drying (green bars) and by freeze-drying plus oven-drying (grey bars). Only a single sample was obtained from the thalamus, thus no error bar is given.*

proteins [142].

Compared to $T_1$, formalin induced shortening of $T_2$ was much lower and ranged between 5 % and 26 % in the thalamus and white matter, respectively. The exact mechanisms remain unclear but this effect may be attributed to the increased viscosity which affects the intramolecular and intermolecular spectral density functions [141]. It also has to be considered that water in brain tissue is compartmentalized and that the apparent $T_2$ obtained from a mono-exponential fit reflects the relative size, $T_2$, and exchange rate of the individual water pools [97]. In this context it has been shown, that fixation reduces the $T_2$ of the intra- and extracellular water only while the myelin water remains unaffected [100]. $T_2$ is usually not dependent on temperature in unfixed brain tissue but fixation causes an
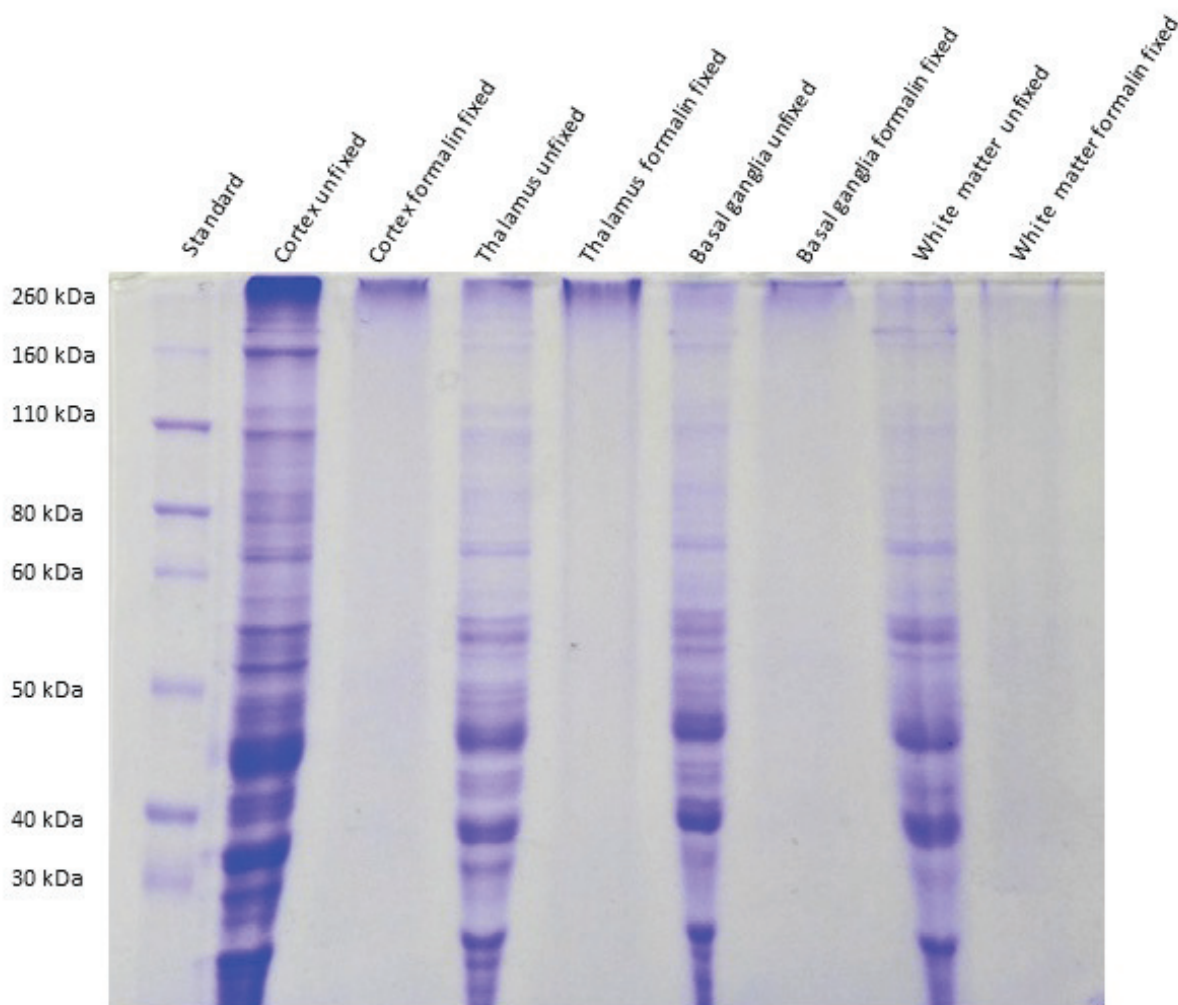
*Figure 5.4: SDS-PAGE of unfixed and formalin fixed brain tissue samples of the cortex, thalamus, basal ganglia and white matter compared to a Novex Sharp pre-stained protein standard.*

increase of the temperature coefficient. This controversial behavior of the temperature coefficients for $T_1$ and $T_2$ will need further investigations. Considering room temperature and fixation, the relaxation time decrease is more prominent in $T_2$ and $T_2^*$ than in $T_1$ as shown in Table 5.2. Consequently, the small differences induced by fixation, get enhanced by a factor of up to 4 when comparing in vivo $T_2$ with $T_2$ obtained from fixed tissue at room temperature.

$T_2^*$ reflects spin dispersion due to microscopic field gradients introduced by tissue components with different magnetic susceptibility such as tissue water, proteins and iron. The

formalin induced shortening of $T_2^*$ suggests an increase of these gradients. One possible explanation for this observation is that interstitial water is partially replaced by formalin, which has a different susceptibility than water. However, the magnetic susceptibility of formalin has not been analyzed so far and this needs further investigations..

Differences between the reported values of several studies [161, 185–187, 192, 200] and the values presented here can be related to the usage of different formalin concentrations, fixation duration, sample preparation, post-mortem delay and embedding media as well as differences in the acquisition temperature. The dependence on the fixation duration was reported by Dawe et al. [185] and showed a rapid decrease of $T_2$ and a stabilization after 150 days. The decrease in MR diffusion was linked with increased post-mortem delay in a study of D'Arceul et al. [134]. The dependence of MR parameters on the embedding media during MRI acquisition was reported by Hales et al. [192] in the rat heart and by Dusek et al. in the human brain [193]. A recovery of $T_2$ relaxation time was reported in literature by washing free fixative from the tissue [143, 190, 191].

Controversial observations on $T_1$ were observed in bovine serum albumin (BSA) phantoms with different concentration of Glutaraldehyde (GA) to model differences in cross-linking. With increasing GA $T_2$ and $T_1$(rho) was decreased compared to an unchanged $T_1$. With increasing BSA concentration, the $T_1$ relaxation time decreased [201]. This might indicate that the cross-linking process of proteins in the human brain affects the $T_1$ relaxation time in a different way, compared to BSA phantom data. The strength of this study was that the same tissue was used for the comparison between relaxation properties in fixed and unfixed tissue. This enabled a more precise assessment of the formalin induced changes.

The applied method for $T_2$ estimation might have some limitations compared to methods like CPMG-sequences or extended phase graphs (EPG) [202, 203]. Inhomogeneous transmit fields and resulting stimulated echoes could have had influenced the calculation of $T_2$ values with. However, we had to keep the acquisition time below 15 min for each temperature point to minimize autolysis effects and to ensure a stable temperature. Nevertheless, the observation that the in-vivo data were in good agreement with the unfixed postmortem data at 37 °C indicate, that field imperfection did not significantly affect the primary outcome of the study, i.e. the quantification of the temperature and fixation effects.

As there is no standardized procedure for WC measurements, we here applied freeze-drying and oven-drying as two commonly accepted approaches. Our results clearly indicate that freeze-drying alone does not remove all water from fixed tissue samples, which may also explain variations across literature. While several studies suggested longer fixation times, we here opted for a much shorter fixation time for water content and SDS-PAGE measurements. However, when considering a sample size of 1 cm3 and a penetration speed of 0.5-1 mm/h of formalin, a 10 day fixation should not have affected the WC measurements.

In conclusion, formalin fixation and temperature changes cause a strong reduction of the $T_1$, $T_2$, and $T_2^*$ relaxation times in the human brain which hamper a direct comparison with in-vivo MRI. The extent of these changes varies across different brain structures. These seem to be mostly related to crosslinking of proteins while loss of tissue water plays a minor role. The descriptive model provided in this work should allow to better understand the effects of formalin fixation and variations in temperature, and to optimize protocols for post-mortem MRI.

6

# Assessment of ferritin content in multiple sclerosis brain using temperature induced R2* changes

Christoph Birkl[1], Daniele Carassiti[1], Klaus Schmierer[1] and Stefan Ropele[1]

[1] Department of Neurology, Medical University of Graz, Austria
[2] Blizard Institute (Neuroscience), Queen Mary, University of London, UK

## 6.1 Introduction

Iron is the most abundant trace elements in the human brain where it plays an important role for normal development and metabolism. Iron is involved in oxygen transport, myelin production, DNA synthesis, mitochondrial respiration, neurotransmitter synthesis and neurotransmitter metabolism [12, 34, 35]. Iron has the ability to switch the state between ferrous iron ($Fe^{2+}$) and ferric iron ($Fe^{3+}$) via the Fenton reaction. Ferrous iron can be oxidized and then causes free radicals [18]. The oxidative damage resulting from this reaction has been discussed as a trigger or at least as a promoter in many neurodegenerative diseases. To prevent oxidation reactions, almost all non-heme iron in the brain is stored in ferritin in a non-reactive form. Ferritin consists of 24 subunits of heavy chain (H) and light chain (L) proteins with iron mineralized to ferrihydrite inside the core of the protein shell [39]. Ferritin is distributed across the entire brain, but highest concentration can be found in oligodendrocytes, in motor neurons and close to the inner shells of the myelin sheets [47].

In multiple sclerosis (MS), observations of regional iron accumulation come from histologic examinations and increasingly from MRI both visually [92, 204, 205] and in a quantitative manner [17, 23, 29, 71]. The mechanism(s) behind the phenomenon of iron accumulation are not yet fully clear. On the one hand, it has been speculated that iron-mediated oxidative stress is the culprit and by the formation of cytotoxic protein aggregates might trigger or promote neurodegeneration [76]. Unbound iron has unpaired electrons, which renders it chemically unstable and highly reactive with other molecules in the brain. Mitochondrial DNA (mtDNA) is located near the inner mitochondrial membrane, and lacks advanced DNA repair mechanisms, making mtDNA particularly susceptible to damage from iron. Cells respond to oxidative damage by neutralizing free radicals through antioxidant enzymes, such as superoxide dismutase (SOD) and catalase. Eventually, damage accumulates due to the inability of cells to repair damage as quickly as it arises. Such mechanisms might also be a major culprit in the pathophysiology of MS. On the other hand, inflammatory processes such as in MS have been shown to cause local accumulation of iron by disrupting the blood–brain barrier [206] and by attracting iron-rich macrophages [206, 207]. Inflammation may also be responsible for reducing the axonal clearance of iron in MS brains [52, 208].

To further explore the complex role of iron in MS, appropriate imaging techniques are

needed that allow to detect and quantify iron in a non-destructive way. Histology and specific staining techniques are commonly applied on thin sections of fixed or frozen tissue. However, all histochemical and immunohistochemical techniques only allow for a semi-quantitative assessment through optical density measurement or cell counting, and usually provide only little macroscopic information. An attractive tool to assess regional iron levels in the brain is MRI because it can exploit the paramagnetic properties of iron nanocrystals inside a magnetic field [82, 160]. $R_2$ and $R_2^*$ relaxation rates are commonly used as a linear measure of iron concentration in gray matter structures because they have been validated [22, 92, 209]. A more recent approach to assess iron content is quantitative susceptibility mapping (QSM), where the susceptibility induced frequency shifts are derived from phase images [30]. The magnetic susceptibility is also a linear function of iron concentration [32].

While most MRI based measures for iron mapping are reliable in gray matter, they fail to assess iron concentration in WM. It has turned out, that tissue susceptibility is also strongly affected by the diamagnetism of myelin and its orientation with respect to the $B_0$ field [111, 210, 211]. Recently, we proposed a novel technique for iron mapping which is based on Curie's law, i.e. the increase of the paramagnetism with decreasing temperatures. By obtaining $R_2^*$ at different temperatures it is possible to eliminate the diamagnetic background and therefore also to quantify the iron content in WM [33]. The temperature dependent coefficients $R_2^*$ has been shown to linearly scale with iron concentration [33]. In this study we applied this new technique for the first time on formalin fixed MS tissue.

The goal of this work was to study the distribution of ferritin in normal and MS brain and to relate the findings to results from immunochemistry. Moreover, we wanted to compare $R_2^*$ with its temperature coefficient with respect to the sensitivity for iron.

## 6.2 Methods

### 6.2.1 Brain Samples

Hemispheric brain slices, with a thickness of $10\,\mathrm{mm}$, of three subjects with MS and one control subject were included in this study. The brain slices were provided from the UK Multiple Sclerosis Tissue Bank based at Imperial College London (Hammersmith Hospital Campus), London, UK. All Slices were formalin fixed using $4\,\%$ formaldehyde. Prior to

MR imaging, the samples were placed in a plastic container filled with formalin and stored in a refrigerator at 4 °C to decrease the temperature of the sample.

## 6.2.2 Magnetic Resonance Imaging

MRI was performed on a clinical 3 T system (Magnetom Tim Trio, Siemens Medical Systems, Erlangen) with the cooled brain slices centered in a wrist coil for temperature dependent MR acquisition. Imaging was started after taking the brain slices from the refrigerator and continued until the slices reached room temperature. This approach typically allowed for 14 different temperature points between 8 °C and 22 °C. The temperature at the surface of the brain slice was monitored during the whole experiment using a LUXTRON Fluoroptic Thermometer (LumaSense Technologies, SantaClara, CA, USA). For $R_2^*$ mapping a spoiled 2D gradient echo sequence (GRE) with six echoes at TE = 4.22, 10.4, 15.88, 21.36, 26.84 and 32.32 ms, a TR of 340 ms, a flip angle of 15° and five averages was used. For the acquisition of $T_2$ weighted images a turbo spin echo sequence with TE/TR of 78/4000 ms was used. The identification of MS lesions was done with a $T_2$ weighted FLAIR sequence with a TE/TR of 51/10000 ms and an inversion time TI = 1200 ms. All sequences were performed with an in plane resolution of $500 \times 500$ $\mu$m and a slice thickness of 2 mm.

## 6.2.3 Histology

To allow a good match between MRI and histology, the brain samples were cut in half after MRI and one half was embedded in paraffin and then stained for myelin basic protein (MBP) and ferritin light chain. Histology then was performed on the kissing side of the two halves. For ferritin quantification, an overview image of each area was acquired at 4x magnification on MBP and ferritin stained sections. This allowed the precise match of the same area on both sections and the manual outlining of corresponding lesion core, lesion edge and NAWM. The software Stereoinvestigator was then used to randomly acquire within each region 8 images at 40x magnification on which ferritin positive cells were manually counted and the relative density of cells expressed as n cells/image. Linear regression analysis was performed to study the relationship between ferritin counts and the temperature coefficient.

## 6.2.4 Image Analysis

In the first step a $R_2^*$ map was calculated for each temperature point assuming a monoexponential decay of the transversal magnetization. Then, the temperature coefficient (TcR2\*) map was calculated pixel wise by estimating the temperature coefficient with a linear regression model with $R_2^* = R_2^*(0) + TcR2^* \cdot \vartheta$, where $R_2^*(0)$ is the offset, TcR2\* is the temperature coefficient and $\vartheta$ is the temperature in °C. According to Curie's law this temperature coefficient is representing the paramagnetic component of the susceptibility and scaling with the iron concentration [33]. ROIs were outlined based on histological images and corresponding $T_2$ weighted MR images. The regions were categorized as follows: core and edge of white matter lesions, core and edge of gray matter lesions, NAWM, normal appearing gray matter (NAGM) and normal appearing basal ganglia (NABG), normal white matter (NWM,) and normal basal ganglia (NBG). The latter two were taken from the control subject. $R_2^*$ and the temperature coefficient TcR2\* were calculated for each region and related to the corresponding ferritin count using a linear regression analysis.

## 6.3 Results

The clinical data of the MS subjects are summarized in Table 6.1.

Considerable variations in iron content were observed across all brain samples. The iron

Table 6.1: *Clinical data and fixation duration of the three MS subjects and the control subject.*

| Case | Sex | MS type | Time of Onset (years) | Time of Progression (years) | Disease duration (years) | Age at death (years) | Fixation duration (months) |
|------|-----|---------|------------------------|------------------------------|---------------------------|-----------------------|-----------------------------|
| MS 1 | F | secondary progressive | 38 | 50 | 14 | 52 | 31 |
| MS 2 | M | primary progressive | 34 | 34 | 8 | 42 | 84 |
| MS 3 | F | secondary progressive | 42 | 54 | 22 | 64 | 24 |
| Control 1 | | Control | - | - | - | 85 | 103 |

content in the core of white matter lesion was found to be lower than in normal appearing white matter, whereas at the rim of most lesions a high iron content was observed. In the temperature coefficients maps of $R_2^*$, these areas are indicated by a strong negative TcR2\* value as shown in Figure 6.1 (arrow 1). Figure 6.1 shows also other representative iron distribution patterns not seen in the corresponding $R_2^*$ map including a high iron content in subcortical U-fibres and in striatal cell bridges between putamen and caudate nucleus. The frontotemporal cortex yielded a higher iron content than NAWM but in MS cases some cortical areas had almost no iron (Figure 6.1).

The pattern of iron distribution in all tissue samples is summarized in Figure 6.2. Com-
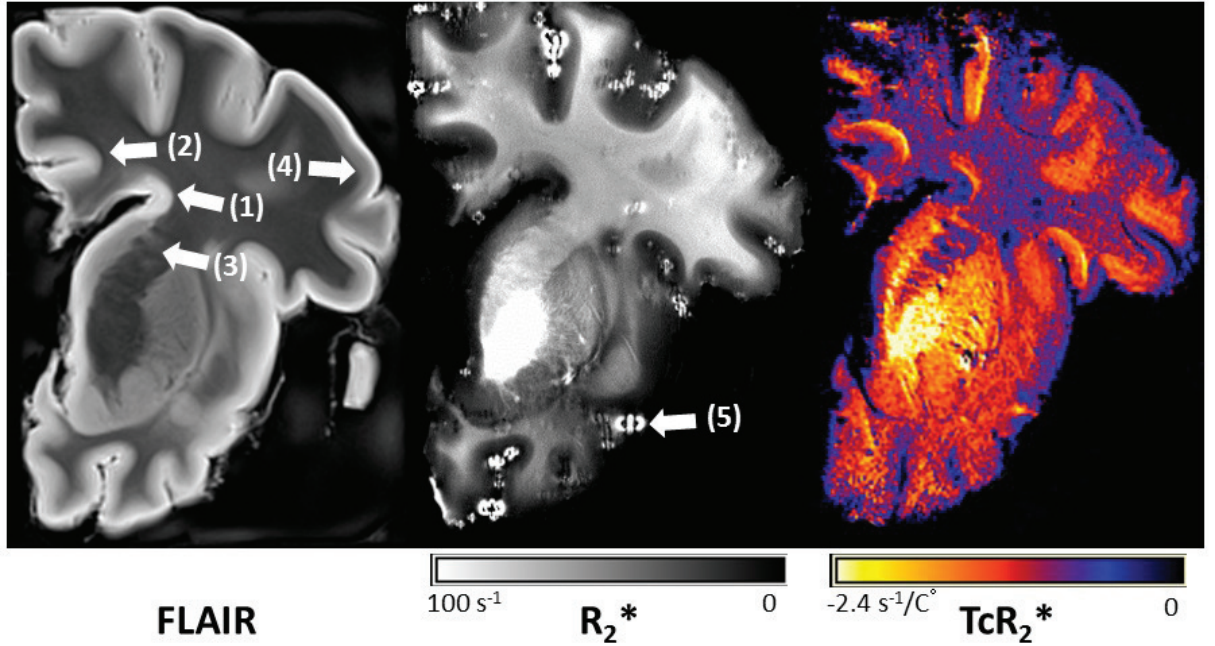
*Figure 6.1: FLAIR image (left panel), $R_2^*$ map (middle panel) and corresponding iron map which represent the temperature coefficient of $R_2^*$ (right panel) showing a formalin fixed MS brain sample. Bright colors in the TcR2\* map (negative temperature coefficient) correspond to a high iron content. The arrows highlight (1) a periventricular lesion with an iron rim, (2) an iron rich subcortical u-fiber, (3) the striatal cell bridges, (4) a section of the cortex with all iron removed and (5) a dipole artefact induced by air bubbles.*

pared to iron levels in NWM from the control subject, iron levels in NAWM and in MS lesions were decreased. In contrast, iron concentration at the edges of lesions and in the basal ganglia was much higher. No differences were found between basal ganglia from MS cases and the control case.

Visual inspections of histology and TcR2\* maps were overall in good agreement. Figure 6.3 shows a large periventricular MS lesions with a demyelinated core. In the non-demyelinated part of the lesion, iron levels were increased in both the ferritin staining and TcR2\* map when compared to NAWM. However, in agreement with histology iron levels were highest at the ventral edges of the lesion which was not visible on the corresponding FLAIR image and $R_2^*$ map. Demyelination of the lesion core is in line with a reduced $R_2^*$ relaxation rate and consistent with the MBP staining.

When considering all analyzed ROIs, the number of ferritin positive cells and TcR2\* showed a significant linear correlation (r = -0.64, p = <0.001) which is shown in Figure 6.4. In contrast, no correlation with ferritin and $R_2^*$ (r = -0.11, p = 0.5) was found.
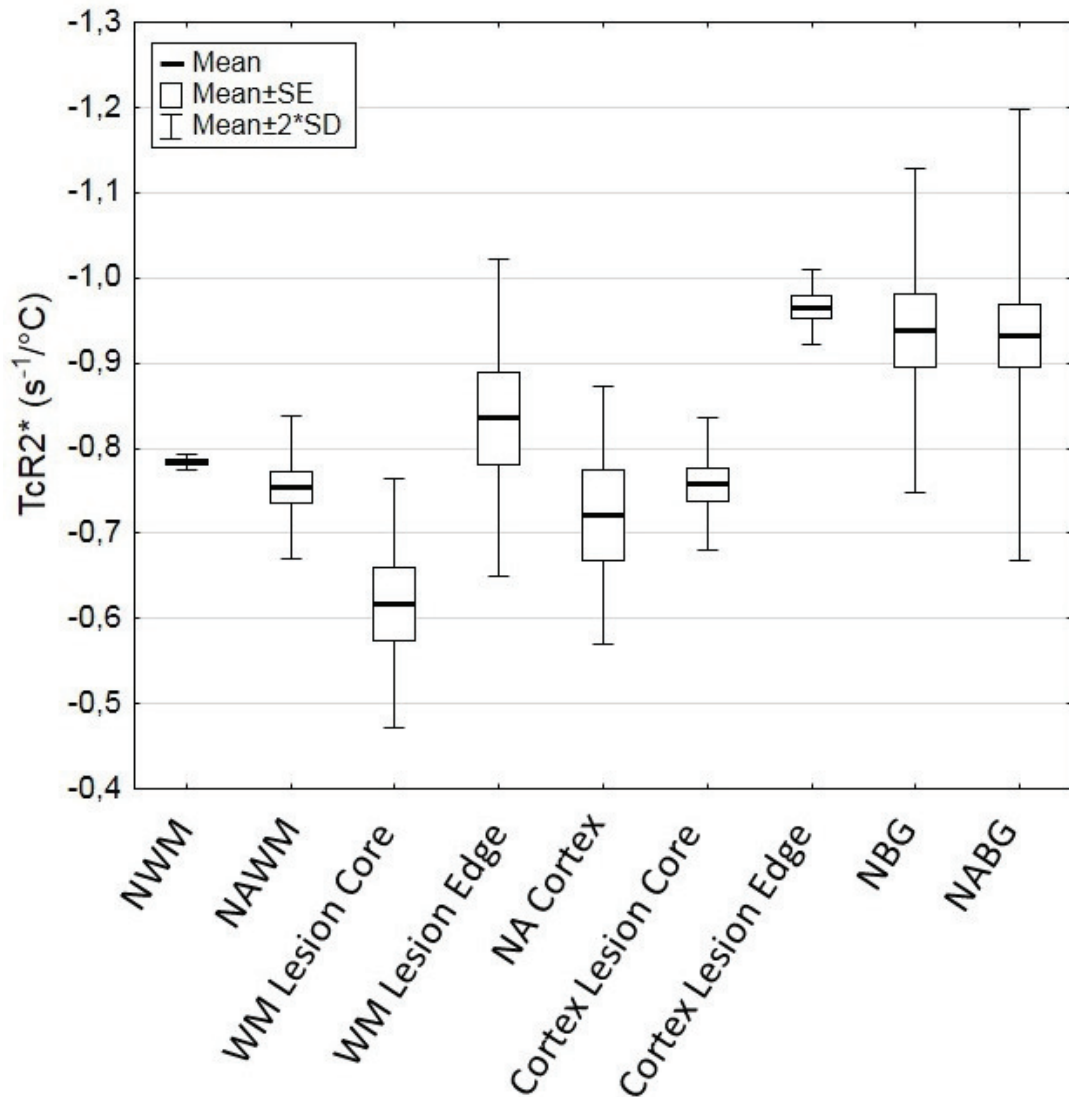
*Figure 6.2: TcR2\* values of normal white matter (NWM), normal appearing white matter (NAWM), white matter lesion core, white matter lesion edge, normal appearing cortex (NA cortex), cortical lesion core, cortical lesion edge, normal basal ganglia (NBG) and normal appearing basal ganglia (NABG). Please note that a more negative TcR2\* indicate a higher iron content and that the scale on the y-axis is reversed.*

## 6.4 Discussion and Conclusion

In this work, we applied for the very first time a novel technique to map the iron concentration in multiple sclerosis brain. The technique is based on the temperature dependency of the magnetic susceptibility and allows to compensate for the myelin related diamagnetism of the tissue. Therefore, susceptibility shifts due to demyelination or changes in water

Table 6.2: Mean and standard deviation of TcR2\*, $R_2^*$ and ferritin count in different regions.

| Tissue | TcR2\* ($\text{s}^{-1}/°\text{C}$) | $R_2^*$ ($\text{s}^{-1}$) | Ferritin Count (a.u.) |
|---|---|---|---|
| Normal white matter (control) | -0.78 ± 0.01 | 47.2 ± 1.8 | 2.1 ± 1.9 |
| Normal appearing white matter | -0.75 ± 0.04 | 46.0 ± 11.9 | 5.2 ± 3.9 |
| White matter lesion Core | -0.62 ± 0.07 | 25.1 ± 10.7 | 4.5 ± 5 |
| White matter lesion edge | -0.84 ± 0.09 | 30.6 ± 4.2 | 16.6 ± 7.2 |
| Normal appearing cortex | -0.72 ± 0.08 | 46.0 ± 8.1 | 1.4 ± 0.4 |
| Cortex lesion core | -0.76 ± 0.04 | 27.9 ± 4.5 | 5.8 ± 1.6 |
| Cortex lesion edge | -0.97 ± 0.02 | 35.1 ± 1.7 | 23.5 ± 5.6 |
| Normal basal ganglia (control) | -0.94 ± 0.10 | 31.4 ± 4.3 | 41.0 ± 22.2 |
| Normal appearing basal ganglia | -0.93 ± 0.13 | 46.5 ± 10.8 | 41.7 ± 37.3 |

content do not affect the iron measurement. MRI acquisition time with the proposed technique is fast, but it can take more than 1 hour until the brain sample has reached room temperature through convection of the surrounding air. Much shorter acquisition times and therefore a higher throughput can be achieved even for whole brains by using a temperature controls system with a heated water bath.

Our results revealed marked variations of the iron content in the MS brains which is in good agreement with recent histological studies. It has been demonstrated that most MS lesions present with decreased iron levels when compared to NAWM [16]. Only approximately 8 % of the lesions show increased iron levels and these lesions are mostly in the late active state. The highest iron content can be found in the rim of the lesion and this rim can also be observed in inactive and slowly expanding lesions [16]. This might also explain why we observed increased iron levels at the rim of most lesions but not in the center of lesions. The iron content of NAWM was lower than in NWM of control tissue which is in line with findings from histopathological studies [16, 92]. Iron levels in the BG were not different between MS cases and the control case although this is a frequently reported finding. However, it has to be considered that the number of ROIs in BG was low and that age related iron accumulation is more prominent than an MS related accumulation [114].

The correlation between TcR2\* and ferritin count qualified TcR2\* as a valid measure for iron content and confirmed that most of the detected iron is stored in ferritin. A higher correlation coefficient could have been prevented by the difficulties to match microscopic
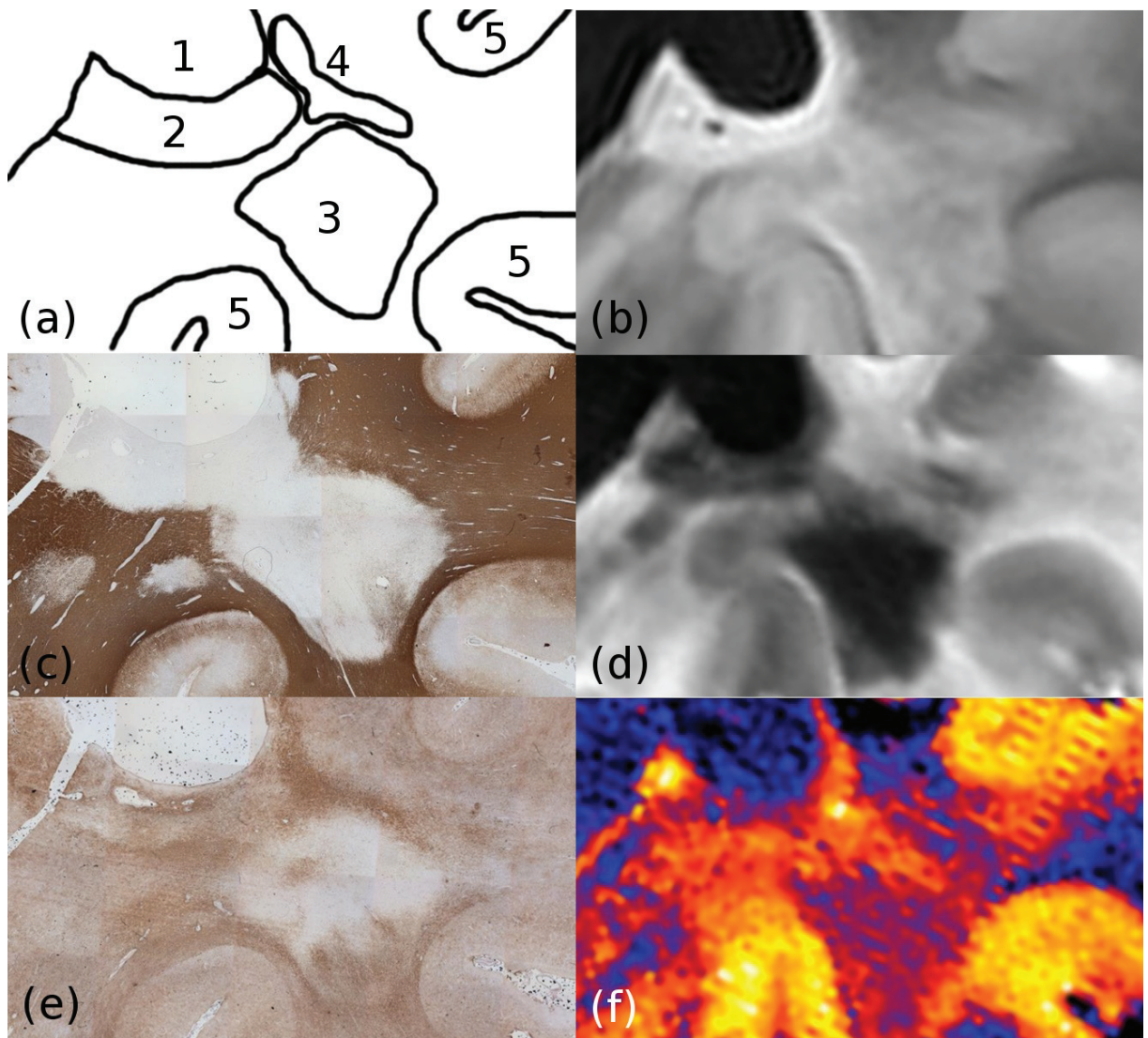
*Figure 6.3: Corresponding histological images and MR images of a periventricular white matter lesion. Panel (a) represents the different brain regions on the histological and MR images, with the ventricel (1), the periventricular lesion (2), the white matter lesion core (3), the lesion edge (4) and the cortex (5). Panel (b) represents the corresponding FLAIR image. Histological images for myelin basic protein (c) and ferritin light chain (e) are compared with the corresponding $R_2^*$ map (d) and Tcr2\* map (f).*

histological images with macroscopic MR images when considering the differences in resolution and slice thickness. Additionally, histology provided only specific information on the ferritin light chain and it is unclear if the ratio of light chain to heavy chain remains constant under pathological conditions. There is some evidence, that this ratio is changed in other neurological diseases with disturbed iron metabolism such as Alzheimer's disease
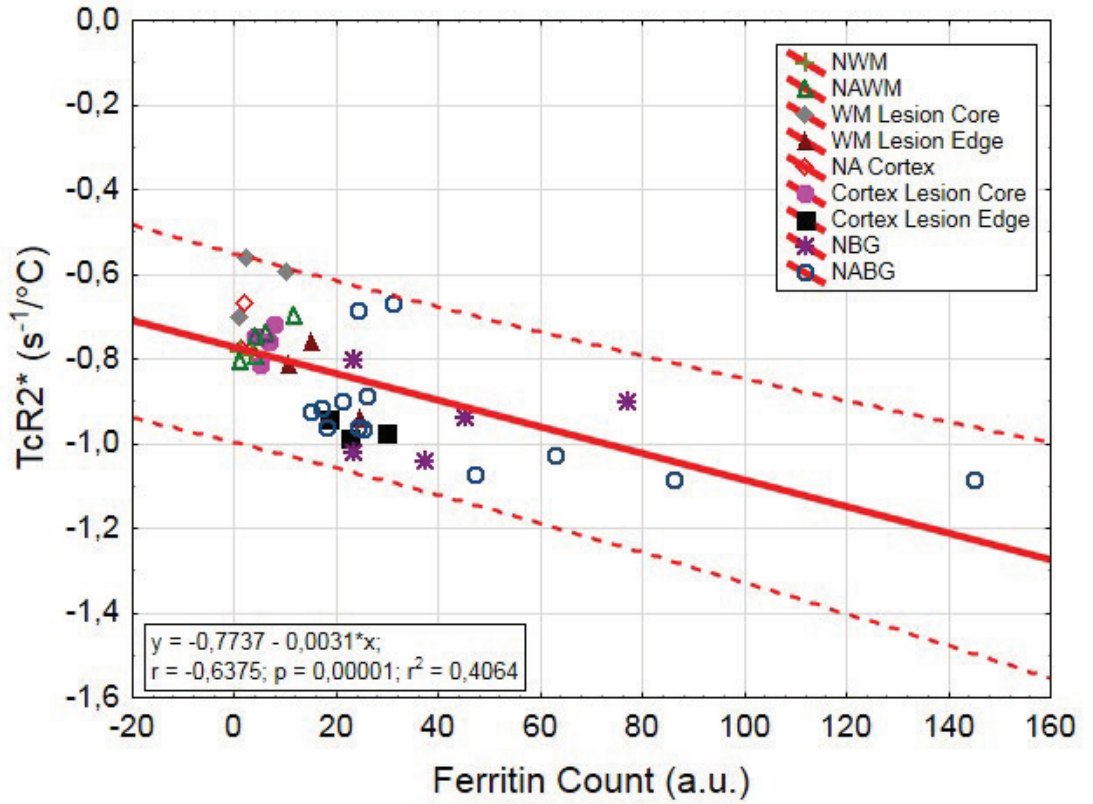
*Figure 6.4: Correlation between TcR2\* and the ferritin count, obtained from histological staining, in normal white matter (NWM), normal appearing white matter (NAWM), white matter lesion core, white matter lesion edge, normal appearing cortex (NA Cortex), cortex lesion core, cortex lesion edge, normal basal ganglia (NBG) and normal appearing basal ganglia (NABG). Note that the temperature coefficient is more negative for higher iron levels.*

or Parkinson disease when compared to healthy individuals [212].

As expected, the $R_2^*$ relaxation rate did not correlate with ferritin counts when taking all regions into account. This has already been observed in previous studies [22] and has been assigned to the counteracting susceptibility effect of the myelins lipids and proteins. $R_2^*$ cannot disentangle demyelination from iron loss since both cause a reduction of $R_2^*$. In addition, when considering inhomogeneous lesions like the one shown in Figure 6.3, it seems that the magnetic contribution of myelin to the bulk susceptibility is much more dominant than the potential contribution of iron in particular since the iron concentration even in normal WM is rather low.

Apart from BG, lesions and perilesional areas, two other structures become apparent

on the iron map, namely the subcortical associations fibers and the striatal cell bridges. Although both structure are known for their increased iron content, they couldn't be specifically depicted by other MRI methods. So far, the depiction of the striatal cell bridges was only possible on high resolution images acquired at $7\,\mathrm{T}$ or higher [213]. The U-fibers are often seen on conventional or DAB-enhanced Perl's stains and their appearance can be explained by the high density of iron-rich oligodendrocytes. From the visual inspection of the iron maps it becomes obvious that the iron homeostasis can also be distorted in U-fibers of MS cases. Data from recent studies suggest, that MS related changes in the U-fibers are linked to cognitive impairment [214, 215].

In this work we focused on the temperature dependency of $R_2^*$ because of the simplicity and robustness of $R_2^*$ mapping. Virtually every other susceptibility related MR parameters can be used for the same purpose including QSM as the latest development in this field. However, due to the required image processing steps QSM does not provide an absolute measure of the susceptibility and needs an internal reference. With increasing temperature, the reference regions (usually CSF or white matter) would change its frequency due to the temperature dependency of the chemical shift which would aggravate a reliable estimation of regional susceptibility changes.

In conclusion, TcR2\* is a valid marker for iron content in brain tissue. While the proposed method is limited to postmortem imaging, it enables iron mapping in entire brain slices at a reasonable resolution. Due to the elimination of myelin induced susceptibility changes, it is well suited for further research into MS and other neurological diseases with regional distortions of the iron homeostasis.

# 7

# Conclusions and Outlook

*"Die Theorie entscheidet über das,*
*was wir beobachten können."*
*– Albert Einstein (1879 - 1955)*

We have argued that iron metabolism in the healthy and diseased human brain is an important research topic. State of the art MR-based techniques for iron mapping are restricted to gray matter structures. A need exists to improve this techniques to increase the sensitivity and enable iron mapping across all brain regions.

We present a novel MRI technique for quantifying iron in the absence of any diamagnetic effect, such as from myelin. The technique is based on the temperature dependency of the paramagnetic susceptibility described by Curie's law. Temperature dependent relaxometry is performed to calculate the temperature coefficient of the effective transverse relaxation rate $R_2^*$. The temperature coefficient, called TcR2*, represents a new MRI iron marker. The possibility to map iron without counteracting myelin is of great importance for diseases, such as MS, which have a disturbed iron metabolism in white matter.

The application of TcR2* in post-mortem MRI of MS brain tissue revealed new insights into the local iron distribution in white and gray matter. Small structures with a high

iron content, such as subcortical u-fibers or striatal cell bridges, were detectable in the TcR2* maps. In conventional $R_2^*$ these substructures were covered by the dominating myelin signal and not visible.

In post-mortem MRI, different processes starting at the time of death influence the images and quantitative MR parameters. Thus, to compare results from post-mortem MRI with *in vivo* MRI, knowledge about the influence of parameters, such as temperature and fixation, on MR images is needed. Therefore in chapter 3 the influence of temperature on the relaxation times of unfixed human brain tissue was investigated. We conclude that the strongest temperature dependency exists in $T_1$ with different rates depending on the brain region. In chapter 5 the influence of fixation on the relaxation times and their temperature coefficients was investigated. All relaxation times were decreased with different rate after formalin fixation. The strongest decrease after fixation was observed in $T_1$ with a reduction of approximately 75%. With additional biomedical analysis the origin of the fixation induced relaxation time decrease was investigated. The results indicate that the change in molecular structure, based on cross-linking of proteins is the reason for the relaxation time decrease.

This project resulted in first time quantitative iron maps of MS white and gray matter. Thus, it was finally possible to acquire information about disease related iron distribution outside the gray matter. The promising results of TcR2* as iron marker, can be used to further examine the role of iron in neurological disorders with disturbed iron metabolism in a post-mortem MRI set-up.

## 7.1 New insights gained in this thesis

The most important and new insights in this project are:

- The strong and different influence of temperature on MR relaxation times, with different rates depending on the brain region.

- The suitability of temperature dependent MRI, based on $R_2^*$ relaxometry, as quantitative iron marker, leading to a novel MRI technique for iron mapping.

- TcR2* as iron marker, independent of any diamagnetic contribution, e.g. caused by myelin.

- The relaxation times of unfixed human brain tissue at 37 ℃ and with a short post-mortem delay, are in line with *in vivo* relaxation time values.

- The origin of the fixation induced relaxation time drop is due to the altered molecular structure and not as assumed a reduced water content.

- The quantitative iron distribution, acquired with TcR2*, of MS brain tissue is in line with findings from histopathology and literature.

## 7.2 Post-mortem effects confounding MRI iron mapping

One of the major goals of this project was to understand different parameters, such as temperature, fixation or autolysis and their effect on post-mortem MRI. Formalin fixation dramatically influences the relaxation times as well as the susceptibility of the tissue. After formalin fixation $R_2^*$ values are increased compared to in vivo. Thus, without the knowledge of fixation induced $R_2^*$ changes the iron content is overestimated. The influence of pure formalin with different concentrations is still an open question and needs further research. Unpublished results of our group suggest a high variance of relaxation times of pure formalin from different vendors. It may be that formalin solutions from different vendors additionally influence the results of $R_2^*$ mapping of fixed tissue samples and hamper the conclusions about the iron content of the tissue based on the relaxation rate. We have not studied the influence of formalin fixation in post-mortem QSM but suggest that this is still an important question and will be investigated in future works.

## 7.3 Final Conclusion and Future Work

The new developed technique, we call it TcR2* mapping, to quantify iron based on the temperature dependent magnetic susceptibility is the most tangible result of this project. It has shown high potential to reveal new insights of the iron distribution in white matter. Thus, already small iron variations which are usually covered by a strong myelin signal become visible.
A possible approach for future research on temperature dependent susceptibility mapping is to investigate the temperature independent part of the susceptibility. This could be a possible marker for diamagnetic contributions, such as myelin. Further, information about white and gray matter microstructure could be obtained by a combined evaluation of the temperaure dependent and temperature independent part of the magnetic susceptibility.

The application of QSM in different post-mortem MRI set-ups remains a challenge. Confounding effects of temperature, fixation and post-mortem interval will alter the phase images and consequently the result of the QSM calculation. Performing post-mortem QSM of fixed tissue will need further investigation of the formalin induced effects on the magnetic susceptibility.

This work showed and quantifies the significant influence of post-mortem effects such as changed temperature and fixation on quantitative MR parameters and image contrast. Thus, to minimize confounding effects on MR parameters, post-mortem MRI should be performed using unfixed biological tissue, with a short post-mortem delay between death and MR acquisition. The image should be acquired at 37 °C to match a "life-like" condition.

The proposed TcR2* mapping is a novel and validated MR-based technique to map iron across all brain regions in post-mortem MRI. The translation of TcR2* mapping from post-mortem MRI to *in vivo* MRI is hampered by the need of a temperature gradient inside the sample during image acquisition. A future project will be to evaluate if external cooling of the brain during *in vivo* MRI is possible and can cause a measurable temperature gradient which is reflected in a changed MR signal.

In conclusion this project verified the potential of temperature dependent MRI as iron marker, independent of diamagnetic effects, to reveal novel insights into the iron distribution in healthy and diseased brain tissue. New post-mortem MRI techniques show a high potential to investigate the microstructure of the biological tissue in remarkable detail. The combination of techniques, such as temperature dependent MRI and SQUID magnetometry will allow a detailed understanding of iron and it's contribution to the magnetic susceptibility in healthy and diseased human brain. Multi-modal approaches to investigate iron in the human brain will increase the knowledge about pathophysiological mechanisms in neurodegenerative diseases. Finally, we were able to show the high potential of new quantitative MR parameters, such as the temperature coefficient, as an image based biomarker for iron.

# References

[1] W. C. Röntgen, "Ueber eine neue Art von Strahlen," *Sonderabbdruck aus den Sitzungsberichten der Würzburg. Phys. Gesellschaft 1895*, 1896.

[2] G. Hounsfield, "Method and apparatus for measuring x-or y-radiation absorption or transmission at plural angles and analyzing the data," 1973.

[3] A. Cormack, "Representation of a function by its line integrals, with some radiological applications," *J. Appl. Phys.*, vol. 34, no. 9, pp. 2722–2727, 1963.

[4] A. Cormack, "Representation of a function by its line integrals, with some radiological applications. II," *J. Appl. Phys.*, vol. 35, no. 10, pp. 2908–2913, 1964.

[5] J. Radon, "On determination of functions by their integral values along certain multiplicities," *Ber Verbhandl Sächs Akad Wiss Liepzig, Math-Phys Kl*, vol. 69, pp. 262–277, 1917.

[6] F. Bloch, W. W. Hansen, and M. Packard, "Nuclear Induction," *Phys. Rev.*, vol. 69, pp. 127–127, feb 1946.

[7] E. Purcell, H. Torrey, and R. Pound, "Resonance Absorption by Nuclear Magnetic Moments in a Solid," *Phys. Rev.*, vol. 69, pp. 37–38, jan 1946.

[8] P. C. LAUTERBUR, "Image Formation by Induced Local Interactions: Examples Employing Nuclear Magnetic Resonance," *Nature*, vol. 242, pp. 190–191, mar 1973.

[9] P. C. Lauterbur, "Magnetic resonance zeugmatography," *Pure Appl. Chem.*, vol. 40, pp. 149–157, jan 1974.

[10] P. Mansfield and A. A. Maudsley, "Planar spin imaging by NMR.," *J Phys C Solid State Phys*, vol. 9, 1976.

[11] P. Mansfield and A. A. Maudsley, "Line scan proton spin imaging in biological structures by NMR," *Phys. Med. Biol.*, vol. 21, pp. 847–852, sep 1976.

[12] D. J. Pinero and J. R. Connor, "Iron in the Brain: An Important Contributor in Normal and Diseased States," *Neurosci.*, vol. 6, pp. 435–453, dec 2000.

[13] R. J. Ward, F. A. Zucca, J. H. Duyn, R. R. Crichton, and L. Zecca, "The role of iron in brain ageing and neurodegenerative disorders," *Lancet Neurol.*, vol. 13, pp. 1045–1060, oct 2014.

[14] A. Compston and A. Coles, "Multiple sclerosis," *Lancet*, vol. 359, no. 9313, pp. 1221–1231, 2002.

[15] A. Compston and A. Coles, "Multiple sclerosis.," *Lancet*, vol. 372, pp. 1502–17, oct 2008.

[16] S. Hametner, I. Wimmer, L. Haider, S. Pfeifenbring, W. Brück, and H. Lassmann, "Iron and neurodegeneration in the multiple sclerosis brain," *Ann. Neurol.*, jul 2013.

[17] M. Khalil, C. Enzinger, C. Langkammer, M. Tscherner, M. Wallner-Blazek, M. Jehna, S. Ropele, S. Fuchs, and F. Fazekas, "Quantitative assessment of brain iron by R(2)* relaxometry in patients with clinically isolated syndrome and relapsing-remitting multiple sclerosis.," *Mult. Scler.*, vol. 15, pp. 1048–54, sep 2009.

[18] E. Stephenson, N. Nathoo, Y. Mahjoub, J. F. Dunn, and V. W. Yong, "Iron in multiple sclerosis: roles in neurodegeneration and repair.," *Nat. Rev. Neurol.*, vol. 10, pp. 459–68, aug 2014.

[19] J. F. Schenck and E. a. Zimmerman, "High-field magnetic resonance imaging of brain iron: birth of a biomarker?," *NMR Biomed.*, vol. 17, pp. 433–45, nov 2004.

[20] E. M. Haacke, N. Y. C. Cheng, M. J. House, Q. Liu, J. Neelavalli, R. J. Ogg, A. Khan, M. Ayaz, W. Kirsch, and A. Obenaus, "Imaging iron stores in the brain using magnetic resonance imaging.," *Magn. Reson. Imaging*, vol. 23, pp. 1–25, jan 2005.

[21] R. J. Ogg and R. G. Steen, "Age-related changes in brain T1 are correlated with iron concentration.," *Magn. Reson. Med.*, vol. 40, pp. 749–53, nov 1998.

[22] C. Langkammer, N. Krebs, W. Goessler, E. Scheurer, F. Ebner, K. Yen, F. Fazekas, and S. Ropele, "Quantitative MR Imaging of Brain Iron : A Postmortem Validation Study," *Radiology*, vol. 257, no. 2, pp. 455–462, 2010.

[23] K. E. Hammond, M. Metcalf, L. Carvajal, D. T. Okuda, R. Srinivasan, D. Vigneron, S. J. Nelson, and D. Pelletier, "Quantitative in vivo magnetic resonance imaging of multiple sclerosis at 7 Tesla with sensitivity to iron.," *Ann. Neurol.*, vol. 64, pp. 707–13, dec 2008.

[24] K. Hopp, B. F. G. Popescu, R. P. E. McCrea, S. L. Harder, C. a. Robinson, M. E. Haacke, A. H. Rajput, A. Rajput, and H. Nichol, "Brain iron detected by SWI high pass filtered phase calibrated with synchrotron X-ray fluorescence," *J. Magn. Reson. Imaging*, vol. 31, no. 6, pp. 1346–1354, 2010.

[25] J. H. Jensen, R. Chandra, A. Ramani, H. Lu, G. Johnson, S.-P. Lee, K. Kaczynski, and J. A. Helpern, "Magnetic field correlation imaging.," *Magn. Reson. Med.*, vol. 55, pp. 1350–61, jun 2006.

[26] J. H. Jensen, K. Szulc, C. Hu, A. Ramani, H. Lu, L. Xuan, M. F. Falangola, R. Chandra, E. A. Knopp, J. Schenck, E. A. Zimmerman, and J. A. Helpern, "Magnetic field correlation as a measure of iron-generated magnetic field inhomogeneities in the brain.," *Magn. Reson. Med.*, vol. 61, pp. 481–5, mar 2009.

[27] S. A. Smith, J. W. M. Bulte, and P. C. M. Van Zijl, "Direct saturation MRI: Theory and application to imaging brain iron," *Magn Reson Med*, vol. 62, pp. 384–393, aug 2009.

[28] C. Langkammer, F. Schweser, N. Krebs, A. Deistung, W. Goessler, E. Scheurer, K. Sommer, G. Reishofer, K. Yen, F. Fazekas, S. Ropele, and J. R. Reichenbach, "Quantitative susceptibility mapping (QSM) as a means to measure brain iron? A post mortem validation study.," *Neuroimage*, may 2012.

[29] C. Langkammer, T. Liu, M. Khalil, C. Enzinger, M. Jehna, S. Fuchs, F. Fazekas, Y. Wang, and S. Ropele, "Quantitative susceptibility mapping in multiple sclerosis.," *Radiology*, vol. 267, pp. 551–9, may 2013.

[30] Y. Wang and T. Liu, "Quantitative susceptibility mapping (QSM): Decoding MRI data for a tissue magnetic biomarker," *Magn. Reson. Med.*, vol. 00, pp. n/a–n/a, jul 2014.

[31] S. Ropele, W. de Graaf, M. Khalil, M. P. Wattjes, C. Langkammer, M. a. Rocca, A. Rovira, J. Palace, F. Barkhof, M. Filippi, and F. Fazekas, "MRI assessment of iron deposition in multiple sclerosis.," *J. Magn. Reson. Imaging*, vol. 34, pp. 13–21, jul 2011.

[32] C. Langkammer, N. Krebs, W. Goessler, E. Scheurer, K. Yen, F. Fazekas, and S. Ropele, "Susceptibility induced gray-white matter MRI contrast in the human brain.," *Neuroimage*, vol. 59, pp. 1413–9, jan 2012.

[33] C. Birkl, C. Langkammer, H. Krenn, W. Goessler, C. Ernst, J. Haybaeck, R. Stollberger, F. Fazekas, and S. Ropele, "Iron mapping using the temperature dependency of the magnetic susceptibility," *Magn. Reson. Med.*, vol. 73, pp. 1282–8, apr 2015.

[34] J. R. Connor, S. L. Menzies, S. M. St Martin, and E. J. Mufson, "Cellular distribution of transferrin, ferritin, and iron in normal and aged human brains.," *J. Neurosci. Res.*, vol. 27, pp. 595–611, dec 1990.

[35] M. E. Badaracco, M. V. R. Siri, and J. M. Pasquini, "Oligodendrogenesis: the role of iron.," *Biofactors*, vol. 36, pp. 98–102, jan.

[36] R. Crichton, *Iron Metabolism.* Chichester, UK: John Wiley & Sons, Ltd, apr 2009.

[37] T. Skjørringe, L. B. Møller, and T. Moos, "Impairment of interrelated ironand copper homeostatic mechanisms in brain contributes to the pathogenesis of neurodegenerative disorders," *Front. Pharmacol.*, vol. 3 SEP, p. 169, jan 2012.

[38] E. E. Benarroch, "Brain iron homeostasis and neurodegenerative disease.," *Neurology*, vol. 72, pp. 1436–40, apr 2009.

[39] F. Brem, A. M. Hirt, M. Winklhofer, K. Frei, Y. Yonekawa, H.-G. Wieser, and J. Dobson, "Magnetic iron compounds in the human brain: a comparison of tumour and hippocampal tissue.," *J. R. Soc. Interface*, vol. 3, pp. 833–41, dec 2006.

[40] H. J. H. Fenton, "LXXIII.?Oxidation of tartaric acid in presence of iron," *J. Chem. Soc. Trans.*, vol. 65, p. 899, jan 1894.

[41] E. C. Theil, "Ferritin: the protein nanocage and iron biomineral in health and in disease.," *Inorg. Chem.*, vol. 52, pp. 12223–33, nov 2013.

[42] J. Dobson, "Nanoscale biogenic iron oxides and neurodegenerative disease.," *FEBS Lett.*, vol. 496, pp. 1–5, may 2001.

[43] P. Brissot, M. Ropert, C. Le Lan, and O. Loréal, "Non-transferrin bound iron: a key role in iron overload and iron toxicity.," *Biochim. Biophys. Acta*, vol. 1820, pp. 403–10, mar 2012.

[44] F. Petrat, H. de Groot, and U. Rauen, "Subcellular distribution of chelatable iron: a laser scanning microscopic study in isolated hepatocytes and liver endothelial cells.," *Biochem. J.*, vol. 356, pp. 61–9, may 2001.

[45] B. P. Esposito, "Labile plasma iron in iron overload: redox activity and susceptibility to chelation," *Blood*, vol. 102, pp. 2670–2677, jun 2003.

[46] F. Bagnato, S. Hametner, B. Yao, P. van Gelderen, H. Merkle, F. K. Cantor, H. Lassmann, and J. H. Duyn, "Tracking iron in multiple sclerosis: a combined imaging and histopathological study at 7 Tesla.," *Brain*, vol. 134, pp. 3602–15, dec 2011.

[47] R. Meguro, Y. Asano, S. Odagiri, C. Li, H. Iwatsuki, and K. Shoumura, "Nonheme-iron histochemistry for light and electron microscopy: a historical, theoretical and technical review.," *Arch. Histol. Cytol.*, vol. 70, pp. 1–19, apr 2007.

[48] B. Hallgren, "Haemoglobin formation and storage iron in protein deficiency.," *Acta Soc. Med. Ups.*, 1954.

[49] B. Todorich, J. M. Pasquini, C. I. Garcia, P. M. Paez, and J. R. Connor, "Oligodendrocytes and myelination: The role of iron," *Glia*, vol. 57, no. 5, pp. 467–478, 2009.

[50] B. Hallgren and P. Sourander, "The effect of age on the non-haemin iron in the human brain.," *J. Neurochem.*, vol. 3, pp. 41–51, oct 1958.

[51] S. L. Hauser and J. R. Oksenberg, "The Neurobiology of Multiple Sclerosis: Genes, Inflammation, and Neurodegeneration," *Neuron*, vol. 52, no. 1, pp. 61–76, 2006.

[52] H. Lassmann, W. Brück, and C. F. Lucchinetti, "The immunopathology of multiple sclerosis: An overview," *Brain Pathol.*, vol. 17, pp. 210–218, apr 2007.

[53] F. D. Lublin and S. C. Reingold, "Defining the clinical course of multiple sclerosis: results of an international survey. National Multiple Sclerosis Society (USA) Advisory Committee on Clinical Trials of New Agents in Multiple Sclerosis.," *Neurology*, vol. 46, pp. 907–11, apr 1996.

[54] M. Simons and J. Trotter, "Wrapping it up: the cell biology of myelination," *Curr. Opin. Neurobiol.*, vol. 17, no. 5, pp. 533–540, 2007.

[55] S. Aggarwal, L. Yurlova, and M. Simons, "Central nervous system myelin: structure, synthesis and assembly," *Trends Cell Biol.*, vol. 21, no. 10, pp. 585–593, 2011.

[56] F. Caramia, E. Tinelli, a. Francia, and C. Pozzilli, "Cognitive deficits in multiple sclerosis: A review of functional MRI studies," *Neurol. Sci.*, vol. 31, no. SUPPL. 2, 2010.

[57] M. Filippi and M. a. Rocca, "MRI and cognition in multiple sclerosis," *Neurol. Sci.*, vol. 31, no. SUPPL. 2, pp. 231–234, 2010.

[58] O. Ghaffar and A. Feinstein, "The neuropsychiatry of multiple sclerosis: a review of recent developments.," *Curr. Opin. Psychiatry*, vol. 20, no. 3, pp. 278–285, 2007.

[59] D. W. Langdon, "Cognition in multiple sclerosis.," *Curr. Opin. Neurol.*, vol. 24, no. 3, pp. 244–249, 2011.

[60] F. Patti, C. Leone, and E. D'Amico, "Treatment options of cognitive impairment in multiple sclerosis," *Neurol. Sci.*, vol. 31, no. SUPPL. 2, pp. 265–269, 2010.

[61] R. Milo and A. Miller, "Revised diagnostic criteria of multiple sclerosis," *Autoimmun. Rev.*, vol. 13, pp. 518–524, apr 2014.

[62] M. Khalil, C. Enzinger, C. Langkammer, S. Ropele, A. Mader, A. Trentini, M. L. G. Vane, M. Wallner-Blazek, G. Bachmaier, J.-J. Archelos, M. J. A. Koel-Simmelink, M. A. Blankenstein, S. Fuchs, F. Fazekas, and C. E. Teunissen, "CSF neurofilament and N-acetylaspartate related brain changes in clinically isolated syndrome.," *Mult. Scler.*, vol. 19, pp. 436–42, apr 2013.

[63] M. Khalil, B. Riedlbauer, C. Langkammer, C. Enzinger, S. Ropele, T. Stojakovic, H. Scharnagl, V. Culea, A. Petzold, C. Teunissen, J.-J. Archelos, S. Fuchs, and F. Fazekas, "Cerebrospinal fluid transferrin levels are reduced in patients with early multiple sclerosis.," *Mult. Scler.*, vol. 20, pp. 1569–77, oct 2014.

[64] D. H. Miller, F. Barkhof, J. A. Frank, G. J. M. Parker, and A. J. Thompson, "Measurement of atrophy in multiple sclerosis: pathological basis, methodological aspects and clinical relevance.," *Brain*, vol. 125, pp. 1676–95, aug 2002.

[65] F. Bagnato, N. Jeffries, N. D. Richert, R. D. Stone, J. M. Ohayon, H. F. McFarland, and J. A. Frank, "Evolution of T1 black holes in patients with multiple sclerosis imaged monthly for 4 years.," *Brain*, vol. 126, pp. 1782–9, aug 2003.

[66] E. Pagani, M. Filippi, M. Rocca, and M. Horsfield, "A method for obtaining tract-specific diffusion tensor MRI measurements in the presence of disease: application to patients with clinically isolated syndromes suggestive of multiple sclerosis," *Neuroimage*, vol. 26, pp. 258–265, may 2005.

[67] D. Kidd, F. Barkhof, R. McConnell, P. R. Algra, I. V. Allen, and T. Revesz, "Cortical lesions in multiple sclerosis.," *Brain*, vol. 122 ( Pt 1, pp. 17–26, jan 1999.

[68] J. W. Peterson, L. Bö, S. Mörk, A. Chang, and B. D. Trapp, "Transected neurites, apoptotic neurons, and reduced inflammation in cortical multiple sclerosis lesions.," *Ann. Neurol.*, vol. 50, pp. 389–400, sep 2001.

[69] L. Haider, C. Simeonidou, G. Steinberger, S. Hametner, N. Grigoriadis, G. Deretzi, G. G. Kovacs, A. Kutzelnigg, H. Lassmann, and J. M. Frischer, "Multiple sclerosis deep grey matter: the relation between demyelination, neurodegeneration, inflammation and iron.," *J. Neurol. Neurosurg. Psychiatry*, jun 2014.

[70] A. J. Walsh, G. Blevins, R. M. Lebel, P. Seres, D. J. Emery, and A. H. Wilman, "Longitudinal MR imaging of iron in multiple sclerosis: an imaging marker of disease.," *Radiology*, vol. 270, pp. 186–96, jan 2014.

[71] M. Khalil, C. Langkammer, S. Ropele, K. Petrovic, M. Loitfelder, M. Jehna, G. Bachmaier, R. Schmidt, C. Enzinger, S. Fuchs, and F. Fazekas, "Determinants of brain iron in multiple sclerosis," *Neurology*, vol. 77, no. 18, pp. 1–8, 2011.

[72] R. M. Lebel, A. Eissa, P. Seres, G. Blevins, and A. H. Wilman, "Quantitative high-field imaging of sub-cortical gray matter in multiple sclerosis.," *Mult. Scler.*, vol. 18, pp. 433–41, may 2012.

[73] B. Yao, F. Bagnato, E. Matsuura, H. Merkle, P. van Gelderen, F. K. Cantor, and J. H. Duyn, "Chronic multiple sclerosis lesions: characterization with high-field-strength MR imaging.," *Radiology*, vol. 262, pp. 206–15, jan 2012.

[74] C. W. Adams, "Perivascular iron deposition and other vascular damage in multiple sclerosis.," *J. Neurol. Neurosurg. Psychiatry*, vol. 51, pp. 260–5, feb 1988.

[75] J. M. Stankiewicz, M. Neema, and A. Ceccarelli, "Iron and multiple sclerosis," *Neurobiol. Aging*, vol. 35, no. SUPPL.2, pp. S51–S58, 2014.

[76] J. Stankiewicz, S. S. Panter, M. Neema, A. Arora, C. E. Batt, and R. Bakshi, "Iron in chronic brain disorders: imaging and neurotherapeutic implications.," *Neurotherapeutics*, vol. 4, pp. 371–86, jul 2007.

[77] H. Langemann, A. Kabiersch, and J. Newcombe, "Measurement of low-molecular-weight antioxidants, uric acid, tyrosine and tryptophan in plaques and white matter from patients with multiple sclerosis.," *Eur. Neurol.*, vol. 32, pp. 248–52, jan 1992.

[78] S. R. Oliveira, A. P. Kallaur, A. N. C. Simão, H. K. Morimoto, J. Lopes, C. Panis, D. L. Petenucci, E. da Silva, R. Cecchini, D. R. Kaimen-Maciel, and E. M. V. Reiche, "Oxidative stress in multiple sclerosis patients in clinical remission: association with the expanded disability status scale.," *J. Neurol. Sci.*, vol. 321, pp. 49–53, oct 2012.

[79] R. P. Feynman, R. B. Leighton, and M. Sands, *The Feynman Lectures on Physics, Volume 3*. Addison-Wesley, 1977.

[80] S. Blundell, *Magnetism in Condensed Matter*. OUP Oxford, 2001.

[81] C. Kittel, *Introduction to Solid State Physics*, vol. 11. Wiley, 2004.

[82] J. Schenck, "The role of magnetic susceptibility in magnetic resonance imaging: MRI magnetic compatibility of the first and second kinds," *Med Phys*, vol. 23, no. 6, pp. 815–850, 1996.

[83] N. Krebs, C. Langkammer, W. Goessler, S. Ropele, F. Fazekas, K. Yen, and E. Scheurer, "Assessment of trace elements in human brain using inductively coupled plasma mass spectrometry," *J. trace Elem. Med. Biol.*, vol. 28, pp. 1–7, jan 2014.

[84] S. H. Koenig and R. D. Brown, "Relaxation of solvent protons by paramagnetic ions and its dependence on magnetic field and chemical environment: implications for NMR imaging.," *Magn. Reson. Med.*, vol. 1, pp. 478–95, dec 1984.

[85] S. H. Koenig and K. E. Kellar, "Theory of 1/T1 and 1/T2 NMRD profiles of solutions of magnetic nanoparticles.," *Magn. Reson. Med.*, vol. 34, pp. 227–33, aug 1995.

[86] D. A. Yablonskiy and E. M. Haacke, "Theory of NMR signal behavior in magnetically inhomogeneous tissues: the static dephasing regime.," *Magn Reson Med*, vol. 32, pp. 749–63, dec 1994.

[87] J. Cohen-Adad, "What can we learn from T2* maps of the cortex?," *Neuroimage*, vol. 93, pp. 189–200, 2014.

[88] P. P. Fatouros, A. Marmarou, K. A. Kraft, S. Inao, and F. P. Schwarz, "In vivo brain water determination by T1 measurements: effect of total water content, hydration fraction, and field strength.," *Magn. Reson. Med.*, vol. 17, pp. 402–13, mar 1991.

[89] I. R. Young, J. W. Hand, A. Oatridge, and M. V. Prior, "Modeling and Observation of Temperature Changes in Vivo Using MRI," *Magn Reson Med*, 1994.

[90] S. Koenig, R. Brown, M. Spiller, and N. Lundbom, "Relaxometry of brain: why white matter appears bright in MRI," *Magn. Reson. . . .*, vol. 14, pp. 482–495, 1990.

[91] J. L. Fernandes and C. E. Rochitte, "T1 mapping: technique and applications.," *Magn. Reson. Imaging Clin. N. Am.*, vol. 23, pp. 25–34, feb 2015.

[92] B. Drayer, P. Burger, R. Darwin, S. Riederer, R. Herfkens, and G. a. Johnson, "MRI of brain iron.," *AJR. Am. J. Roentgenol.*, vol. 147, pp. 103–10, jul 1986.

[93] J. Vymazal, R. A. Brooks, O. Zak, C. McRill, C. Shen, and G. Di Chiro, "T1 and T2 of ferritin at different field strengths: effect on MRI.," *Magn. Reson. Med.*, vol. 27, pp. 368–74, oct 1992.

[94] J. Vymazal, O. Zak, J. W. Bulte, P. Aisen, and R. A. Brooks, "T1 and T2 of ferritin solutions: effect of loading factor.," *Magn. Reson. Med.*, vol. 36, pp. 61–5, jul 1996.

[95] N. J. Schneiders, H. Post, P. Brunner, J. Ford, R. N. Bryan, and M. R. Willcott, "Accurate T2 NMR images.," *Med. Phys.*, vol. 10, pp. 642–5, jan 1983.

[96] K. M. Hasan, I. S. Walimuni, L. a. Kramer, and P. a. Narayana, "Human brain iron mapping using atlas-based T2 relaxometry.," *Magn Reson Med*, vol. 67, pp. 731–9, mar 2012.

[97] C. Laule, I. M. Vavasour, S. H. Kolind, D. K. B. Li, T. L. Traboulsee, G. R. W. Moore, and A. L. MacKay, "Magnetic resonance imaging of myelin.," *Neurotherapeutics*, vol. 4, pp. 460–84, jul 2007.

[98] A. MacKay, C. Laule, I. Vavasour, T. Bjarnason, S. Kolind, and B. Mädler, "Insights into brain microstructure from the T2 distribution," *Magn. Reson. Imaging*, vol. 24, no. 4, pp. 515–525, 2006.

[99] A. MacKay, K. Whittall, J. Adler, D. Li, D. Paty, and D. Graeb, "In vivo visualization of myelin water in brain by magnetic resonance.," *Magn. Reson. Med.*, vol. 31, pp. 673–7, jun 1994.

[100] C. Laule, P. Kozlowski, E. Leung, D. K. B. Li, A. L. Mackay, and G. R. W. Moore, "Myelin water imaging of multiple sclerosis at 7 T: correlations with histopathology.," *Neuroimage*, vol. 40, pp. 1575–80, may 2008.

[101] J. Oh, E. T. Han, D. Pelletier, and S. J. Nelson, "Measurement of in vivo multi-component T2 relaxation times for brain tissue using multi-slice T2 prep at 1.5 and 3 T," *Magn. Reson. Imaging*, vol. 24, pp. 33–43, 2006.

[102] D. A. Yablonskiy, "Quantification of Intrinsic Magnetic Susceptibility-Related Effects in a Tissue Matrix. Phantom Study," *Magn. Reson. Med.*, vol. 39, no. 3, pp. 417–428, 1998.

[103] J. Frahm, K. D. Merboldt, and W. Hänicke, "Direct FLASH MR imaging of magnetic field inhomogeneities by gradient compensation.," *Magn. Reson. Med.*, vol. 6, pp. 474–80, apr 1988.

[104] J. Sedlacik, K. Boelmans, U. Löbel, B. Holst, S. Siemonsen, and J. Fiehler, "Reversible, irreversible and effective transverse relaxation rates in normal aging brain at 3T.," *Neuroimage*, sep 2013.

[105] H. Dahnke and T. Schaeffter, "Limits of detection of SPIO at 3.0 T using T2 relaxometry.," *Magn. Reson. Med.*, vol. 53, pp. 1202–6, may 2005.

[106] M. a. Fernández-Seara and F. W. Wehrli, "Postprocessing technique to correct for background gradients in image-based R*(2) measurements.," *Magn. Reson. Med.*, vol. 44, pp. 358–66, sep 2000.

[107] J. Cohen-Adad, J. Polimeni, K. Helmer, T. Benner, J. McNab, L. Wald, B. Rosen, and C. Mainero, "T2* mapping and B0 orientation-dependence at 7T reveal cyto- and myeloarchitecture organization of the human cortex," *Neuroimage*, vol. 60, pp. 1006–1014, apr 2012.

[108] Y. Du, R. Chu, and D. Hwang, "Fast multislice mapping of the myelin water fraction using multicompartment analysis of T 2* decay at 3T: a preliminary postmortem study," *Magn. . . .*, vol. 58, pp. 865–870, 2007.

[109] X. He and D. A. Yablonskiy, "Biophysical mechanisms of phase contrast in gradient echo MRI.," *Proc. Natl. Acad. Sci. U. S. A.*, vol. 106, pp. 13558–63, aug 2009.

[110] M. Fukunaga, T.-Q. Li, P. van Gelderen, J. a. de Zwart, K. Shmueli, B. Yao, J. Lee, D. Maric, M. a. Aronova, G. Zhang, R. D. Leapman, J. F. Schenck, H. Merkle, and J. H. Duyn, "Layer-specific variation of iron content in cerebral cortex as a source of MRI contrast.," *Proc. Natl. Acad. Sci. U. S. A.*, vol. 107, pp. 3834–9, feb 2010.

[111] J. Lee, K. Shmueli, B.-T. Kang, B. Yao, M. Fukunaga, P. van Gelderen, S. Palumbo, F. Bosetti, A. C. Silva, and J. H. Duyn, "The contribution of myelin to magnetic susceptibility-weighted contrasts in high-field MRI of the brain.," *Neuroimage*, vol. 59, pp. 3967–75, feb 2012.

[112] J. H. Duyn, P. van Gelderen, T. Q. Li, J. A. de Zwart, A. P. Koretsky, and M. Fukunaga, "High-field MRI of brain cortical substructure based on signal phase," *Proc. Natl. Acad. Sci. U. S. A.*, vol. 104, pp. 11796–11801, jul 2007.

[113] T.-Q. Li, P. van Gelderen, H. Merkle, L. Talagala, A. P. Koretsky, and J. Duyn, "Extensive heterogeneity in white matter intensity in high-resolution T2*-weighted MRI of the human brain at 7.0 T.," *Neuroimage*, vol. 32, no. 3, pp. 1032–40, 2006.

[114] S. Ropele, I. D. Kilsdonk, M. P. Wattjes, C. Langkammer, W. L. de Graaf, J. L. Frederiksen, H. B. Larsson, M. Yiannakas, C. A. Wheeler-Kingshott, C. Enzinger, M. Khalil, M. a. Rocca, T. Sprenger, M. Amann, L. Kappos, M. Filippi, A. Rovira, O. Ciccarelli, F. Barkhof, and F. Fazekas, "Determinants of iron accumulation in deep grey matter of multiple sclerosis patients.," *Mult. Scler.*, apr 2014.

[115] C. Langkammer, K. Bredies, B. A. Poser, M. Barth, G. Reishofer, A. P. Fan, B. Bilgic, F. Fazekas, C. Mainero, and S. Ropele, "Fast quantitative susceptibility mapping using 3D EPI and total generalized variation.," *Neuroimage*, vol. 111, pp. 622–30, may 2015.

[116] E. M. Haacke, S. Liu, S. Buch, W. Zheng, D. Wu, and Y. Ye, "Quantitative susceptibility mapping: current status and future directions," *Magn. Reson. Imaging*, vol. 33, no. 1, pp. 1–25, 2015.

[117] R. Salomir, B. D. de Senneville, and C. T. Moonen, "A fast calculation method for magnetic field inhomogeneity due to an arbitrary distribution of bulk susceptibility," *Concepts Magn. Reson.*, vol. 19B, pp. 26–34, oct 2003.

[118] J. Marques and R. Bowtell, "Application of a Fourier-based method for rapid calculation of field inhomogeneity due to spatial variation of magnetic susceptibility," *Concepts Magn. Reson. Part B Magn. Reson. Eng.*, vol. 25B, pp. 65–78, apr 2005.

[119] K. Shmueli, J. A. de Zwart, P. van Gelderen, T. Q. Li, S. J. Dodd, and J. H. Duyn, "Magnetic susceptibility mapping of brain tissue in vivo using MRI phase data," *Magn Reson Med*, oct 2009.

[120] S. Robinson, G. Grabner, S. Witoszynskyj, and S. Trattnig, "Combining phase images from multi-channel RF coils using 3D phase offset maps derived from a dual-echo scan," *Magn. Reson. Med.*, vol. 65, pp. 1638–1648, jun 2011.

[121] P. J. Koopmans, R. Manniesing, W. J. Niessen, M. A. Viergever, and M. Barth, "MR venography of the human brain using susceptibility weighted imaging at very high field strength.," *MAGMA*, vol. 21, pp. 149–58, mar 2008.

[122] M. A. Bernstein, M. Grgic, T. J. Brosnan, and N. J. Pelc, "Reconstructions of phase contrast, phased array multicoil data.," *Magn. Reson. Med.*, vol. 32, pp. 330–4, sep 1994.

[123] D. C. Ghiglia and L. A. Romero, "Robust two-dimensional weighted and unweighted phase unwrapping that uses fast transforms and iterative methods," *J. Opt. Soc. Am. A*, vol. 11, p. 107, jan 1994.

[124] M. A. Schofield and Y. Zhu, "Fast phase unwrapping algorithm for interferometric applications," *Opt. Lett.*, vol. 28, no. 14, pp. 1194–1196, 2003.

[125] F. Schweser, A. Deistung, K. Sommer, and J. R. Reichenbach, "Toward online reconstruction of quantitative susceptibility maps: superfast dipole inversion.," *Magn. Reson. Med.*, vol. 69, pp. 1582–94, jun 2013.

[126] S. M. Smith, "Fast robust automated brain extraction.," *Hum. Brain Mapp.*, vol. 17, pp. 143–55, nov 2002.

[127] E. M. Haacke, Y. Xu, Y.-C. N. Cheng, and J. R. Reichenbach, "Susceptibility weighted imaging (SWI).," *Magn. Reson. Med.*, vol. 52, pp. 612–8, sep 2004.

[128] J. Neelavalli, Y.-C. N. Cheng, J. Jiang, and E. M. Haacke, "Removing background phase variations in susceptibility-weighted imaging using a fast, forward-field calculation.," *J. Magn. Reson. Imaging*, vol. 29, pp. 937–48, apr 2009.

[129] T. Liu, P. Spincemaille, L. de Rochefort, B. Kressler, and Y. Wang, "Calculation of susceptibility through multiple orientation sampling (COSMOS): A method for conditioning the inverse problem from measured magnetic field map to susceptibility source image in MRI," *Magn. Reson. Med.*, vol. 61, pp. 196–204, jan 2009.

[130] F. Schweser, A. Deistung, B. W. Lehr, and J. R. Reichenbach, "Quantitative imaging of intrinsic magnetic tissue properties using MRI signal phase: an approach to in vivo brain iron metabolism?," *Neuroimage*, vol. 54, pp. 2789–807, feb 2011.

[131] T. Liu, P. Spincemaille, L. De Rochefort, B. Kressler, and Y. Wang, "Calculation of susceptibility through multiple orientation sampling (COSMOS): A method for conditioning the inverse problem from measured magnetic field map to susceptibility source image in MRI," *Magn. Reson. Med.*, vol. 61, no. 1, pp. 196–204, 2009.

[132] T. Liu, C. Wisnieff, M. Lou, W. Chen, P. Spincemaille, and Y. Wang, "Nonlinear formulation of the magnetic field to source relationship for robust quantitative susceptibility mapping," *Magn. Reson. Med.*, vol. 000, pp. n/a–n/a, apr 2012.

[133] J. Tang, S. Liu, J. Neelavalli, Y. C. N. Cheng, S. Buch, and E. M. Haacke, "Improving susceptibility mapping using a threshold-based K-space/image domain iterative reconstruction approach," *Magn. Reson. Med.*, vol. 000, pp. n/a–n/a, jun 2012.

[134] H. D'Arceuil and A. de Crespigny, "The effects of brain tissue decomposition on diffusion tensor imaging and tractography.," *Neuroimage*, vol. 36, pp. 64–8, may 2007.

[135] A. Abragam, *The Principles of Nuclear Magnetism.* 1961.

[136] J. C. Hindman, "Proton Resonance Shift of Water in the Gas and Liquid States," *J. Chem. Phys.*, vol. 44, p. 4582, may 1966.

[137] R. Stollberger, P. W. Ascher, D. Huber, W. Renhart, H. Radner, and F. Ebner, "Temperature monitoring of interstitial thermal tissue coagulation using MR phase images.," *J. Magn. Reson. Imaging*, vol. 8, no. 1, pp. 188–96, 1998.

[138] V. Rieke and K. B. Pauly, "MR Thermometry," *J Magn Reson Imaging*, vol. 390, pp. 376–390, 2008.

[139] D. K. Jones, *Diffusion MRI*, vol. 4. Oxford University Press, 2010.

[140] C. Birkl, C. Langkammer, J. Haybaeck, C. Ernst, R. Stollberger, F. Fazekas, and S. Ropele, "Temperature-induced changes of magnetic resonance relaxation times in the human brain: A postmortem study.," *Magn. Reson. Med.*, vol. 71, pp. 1575–1580, may 2014.

[141] P. A. Bottomley, T. H. Foster, R. E. Argersinger, and L. M. Pfeifer, "A Review of normal tissue hydrogen NMR relaxation times and relax mechanisms from 1-100MHZ: Dependence on tissue type, NMR frequency, temperature, species, excision, and age," *Med. Phys.*, 1984.

[142] T. Nelson and S. Tung, "Temperature dependence of proton relaxation times in vitro," *Magn Reson Imaging*, vol. 5, pp. 189–199, 1987.

[143] P. E. Thelwall, T. M. Shepherd, G. J. Stanisz, and S. J. Blackband, "Effects of temperature and aldehyde fixation on tissue water diffusion properties, studied in an erythrocyte ghost tissue model.," *Magn Reson Med*, vol. 56, pp. 282–9, aug 2006.

[144] A. Pfefferbaum, E. V. Sullivan, E. Adalsteinsson, T. Garrick, and C. Harper, "Postmortem MR imaging of formalin-fixed human brain," *Neuroimage*, vol. 21, pp. 1585–1595, 2004.

[145] M. Peller, V. Kurze, R. Loeffler, S. Pahernik, M. Dellian, A. E. Goetz, R. Issels, and M. Reiser, "Hyperthermia induces T1 relaxation and blood flow changes in tumors. A MRI thermometry study in vivo.," *Magn. Reson. Imaging*, vol. 21, pp. 545–51, jun 2003.

[146] L. Lüdemann, W. Wlodarczyk, J. Nadobny, M. Weihrauch, J. Gellermann, and P. Wust, "Non-invasive magnetic resonance thermography during regional hyperthermia.," *Int J Hyperth.*, vol. 26, pp. 273–82, jan 2010.

[147] N. Bloembergen, E. M. Purcell, and R. V. Pound, "Relaxation Effects in Nuclear Magnetic Resonance Absorption *," *Phys. Rev.*, vol. 73, no. 1947, 1948.

[148] R. M. Henkelman, G. J. Stanisz, and S. J. Graham, "Magnetization transfer in MRI: a review.," *NMR Biomed*, vol. 14, pp. 57–64, apr 2001.

[149] R. S. Balaban and T. L. Ceckler, "Magnetization transfer contrast in magnetic resonance imaging.," *Magn. Reson. Q.*, vol. 8, pp. 116–37, jun 1992.

[150] H. Neeb, K. Zilles, and N. Shah, "Fully-automated detection of cerebral water content changes: Study of age-and gender-related H 2 O patterns with quantitative MRI," *Neuroimage*, vol. 29, pp. 910–922, 2006.

[151] H. Neeb, K. Zilles, and N. J. Shah, "A new method for fast quantitative mapping of absolute water content in vivo.," *Neuroimage*, vol. 31, pp. 1156–68, jul 2006.

[152] R. Turner, A.-M. Oros-Peusquens, S. Romanzetti, K. Zilles, and N. J. Shah, "Optimised in vivo visualisation of cortical structures in the human brain at 3 T using IR-TSE.," *Magn Reson Imaging*, vol. 26, pp. 935–42, sep 2008.

[153] P. J. Wright, O. E. Mougin, J. J. Totman, a. M. Peters, M. J. Brookes, R. Coxon, P. E. Morris, M. Clemence, S. T. Francis, R. W. Bowtell, and P. a. Gowland, "Water proton T 1 measurements in brain tissue at 7, 3, and 1.5 T using IR-EPI, IR-TSE, and MPRAGE: results and optimization," *MAGMA*, vol. 21, pp. 121–30, mar 2008.

[154] S. C. L. Deoni, "Transverse relaxation time (T2) mapping in the brain with off-resonance correction using phase-cycled steady-state free precession imaging.," *J Magn Reson Imaging*, vol. 30, pp. 411–7, aug 2009.

[155] A. M. Peters, M. J. Brookes, F. G. Hoogenraad, P. a. Gowland, S. T. Francis, P. G. Morris, and R. Bowtell, "T2* measurements in human brain at 1.5, 3 and 7 T.," *Magn. Reson. Imaging*, vol. 25, pp. 748–53, jul 2007.

[156] K. Schmierer, F. Scaravilli, D. R. Altmann, G. J. Barker, and D. H. Miller, "Magnetization transfer ratio and myelin in postmortem multiple sclerosis brain," *Ann Neurol*, vol. 56, pp. 407–415, sep 2004.

[157] B. Quesson, J. a. de Zwart, and C. T. Moonen, "Magnetic resonance temperature imaging for guidance of thermotherapy.," *J Magn Reson Imaging*, vol. 12, pp. 525–33, oct 2000.

[158] S. C. L. Deoni, T. M. Peters, and B. K. Rutt, "High-resolution T1 and T2 mapping of the brain in a clinically acceptable time with DESPOT1 and DESPOT2.," *Magn Reson Med*, vol. 53, pp. 237–41, jan 2005.

[159] G. Brix, L. R. Schad, M. Deimling, and W. J. Lorenz, "Fast and precise T1 imaging using a TOMROP sequence.," *Magn Reson Imaging*, vol. 8, pp. 351–6, jan 1990.

[160] J. F. Schenck, "Health and physiological effects of human exposure to whole-body four-tesla magnetic fields during MRI.," *Ann N Y Acad Sci*, vol. 649, pp. 285–301, mar 1992.

[161] K. Schmierer, C. A. Wheeler-Kingshott, D. J. Tozer, P. A. Boulby, H. G. Parkes, T. A. Yousry, F. Scaravilli, G. J. Barker, P. S. Tofts, and D. H. Miller, "Quantitative magnetic resonance of postmortem multiple sclerosis brain before and after fixation," *Magn Reson Med*, vol. 59, pp. 268–277, feb 2008.

[162] L. Zecca, M. B. H. Youdim, P. Riederer, J. R. Connor, and R. R. Crichton, "Iron, brain ageing and neurodegenerative disorders.," *Nat. Rev. Neurosci.*, vol. 5, pp. 863–73, nov 2004.

[163] D. B. Kell, "Iron behaving badly: inappropriate iron chelation as a major contributor to the aetiology of vascular and other progressive inflammatory and degenerative diseases.," *BMC Med. Genomics*, vol. 2, p. 2, jan 2009.

[164] G. Bartzokis, M. Aravagiri, W. H. Oldendorf, J. Mintz, and S. R. Marder, "Field dependent transverse relaxation rate increase may be a specific measure of tissue iron stores.," *Magn. Reson. Med.*, vol. 29, pp. 459–64, apr 1993.

[165] E. P. Raven, P. H. Lu, T. A. Tishler, P. Heydari, and G. Bartzokis, "Increased Iron Levels and Decreased Tissue Integrity in Hippocampus of Alzheimer's Disease Detected in vivo with Magnetic Resonance Imaging.," *J. Alzheimers. Dis.*, vol. 37, pp. 127–36, jan 2013.

[166] W. R. W. Martin, M. Wieler, and M. Gee, "Midbrain iron content in early Parkinson disease: a potential biomarker of disease status.," *Neurology*, vol. 70, pp. 1411–7, apr 2008.

[167] J. Y. Kwan, S. Y. Jeong, P. Van Gelderen, H.-X. Deng, M. M. Quezado, L. E. Danielian, J. a. Butman, L. Chen, E. Bayat, J. Russell, T. Siddique, J. H. Duyn, T. a. Rouault, and M. K. Floeter, "Iron accumulation in deep cortical layers accounts for MRI signal abnormalities in ALS: correlating 7 tesla MRI and pathology.," *PLoS One*, vol. 7, p. e35241, jan 2012.

[168] D. Berg and M. B. H. Youdim, "Role of iron in neurodegenerative disorders.," *Top. Magn. Reson. Imaging*, vol. 17, pp. 5–17, feb 2006.

[169] F. Schweser, K. Sommer, A. Deistung, and J. R. Reichenbach, "Quantitative susceptibility mapping for investigating subtle susceptibility variations in the human brain.," *Neuroimage*, vol. 62, pp. 2083–100, sep 2012.

[170] W. Li, B. Wu, A. Batrachenko, V. Bancroft-Wu, R. A. Morey, V. Shashi, C. Langkammer, M. D. De Bellis, S. Ropele, A. W. Song, and C. Liu, "Differential developmental trajectories of magnetic susceptibility in human brain gray and white matter over the lifespan.," *Hum. Brain Mapp.*, sep 2013.

[171] T. Liu, J. Liu, L. de Rochefort, P. Spincemaille, I. Khalidov, J. R. Ledoux, and Y. Wang, "Morphology enabled dipole inversion (MEDI) from a single-angle acquisition: comparison with COSMOS in human brain imaging.," *Magn. Reson. Med.*, vol. 66, pp. 777–83, sep 2011.

[172] C. Denk, E. Hernandez Torres, A. MacKay, and A. Rauscher, "The influence of white matter fibre orientation on MR signal phase and decay.," *NMR Biomed.*, vol. 24, pp. 246–52, apr 2011.

[173] W. Li, B. Wu, A. V. Avram, and C. Liu, "Magnetic susceptibility anisotropy of human brain in vivo and its molecular underpinnings.," *Neuroimage*, vol. 59, pp. 2088–97, feb 2012.

[174] S. Wharton and R. Bowtell, "Fiber orientation-dependent white matter contrast in gradient echo MRI.," *Proc. Natl. Acad. Sci. U. S. A.*, vol. 109, pp. 18559–64, nov 2012.

[175] F. Schweser, A. Deistung, K. Sommer, and J. R. Reichenbach, "Toward online reconstruction of quantitative susceptibility maps: Superfast dipole inversion.," *Magn. Reson. Med.*, vol. 000, jul 2012.

[176] M. K. Peprah, G. W. Astary, T. H. Mareci, and M. W. Meisel, "Absolute magnetic susceptibility of rat brain tissue.," *Magn. Reson. Med.*, vol. 00, pp. 2–5, oct 2013.

[177] J. Lee, P. van Gelderen, L.-W. Kuo, H. Merkle, A. C. Silva, and J. H. Duyn, "T2*-based fiber orientation mapping.," *Neuroimage*, vol. 57, pp. 225–34, jul 2011.

[178] S. a. Makhlouf, F. T. Parker, and a. E. Berkowitz, "Magnetic hysteresis anomalies in ferritin," *Phys. Rev. B*, vol. 55, no. 22, pp. R14717–R14720, 1997.

[179] J. Kolasinski, C. J. Stagg, S. a. Chance, G. C. DeLuca, M. M. Esiri, E.-H. E.-H. Chang, J. a. Palace, J. a. McNab, M. Jenkinson, K. L. Miller, and H. Johansen-Berg, "A combined post-mortem magnetic resonance imaging and quantitative histological study of multiple sclerosis pathology," *Brain*, vol. 135, pp. 2938–2951, oct 2012.

[180] J. De Reuck, F. Auger, C. Cordonnier, V. Deramecourt, N. Durieux, F. Pasquier, R. Bordet, C. a. Maurage, and D. Leys, "Comparison of 7.0-T $T_2$*-magnetic resonance imaging of cerebral bleeds in post-mortem brain sections of Alzheimer patients with their neuropathological correlates.," *Cerebrovasc. Dis.*, vol. 31, pp. 511–7, jan 2011.

[181] V. Antharam, J. F. Collingwood, J.-P. Bullivant, M. R. Davidson, S. Chandra, A. Mikhaylova, M. E. Finnegan, C. Batich, J. R. Forder, and J. Dobson, "High field magnetic resonance microscopy of the human hippocampus in Alzheimer's disease : quantitative imaging and correlation with iron," *Neuroimage*, vol. 59, no. 2, pp. 1249–1260, 2012.

[182] A. Droby, C. Lukas, A. Schänzer, I. Spiwoks-becker, A. Giorgio, R. Gold, N. D. Stefano, H. Kugel, M. Deppe, H. Wiendl, S. G. Meuth, T. Acker, F. Zipp, and R. Deichmann, "A human post-mortem brain model for the standardization of multi-centre MRI studies," *Neuroimage*, 2015.

[183] C. H. Fox, F. B. Johnson, J. Whiting, and P. P. Roller, "Formaldehyde fixation.," *J. Histochem. Cytochem.*, vol. 33, pp. 845–853, aug 1985.

[184] M. Tovi and A. Ericsson, "Measurements of T1 and T2 over time in formalin-fixed human whole-brain specimens," *Acta radiol.*, vol. 33, no. 5, pp. 400–404, 1992.

[185] R. J. Dawe, D. a. Bennett, J. a. Schneider, S. K. Vasireddi, and K. Arfanakis, "Post-mortem MRI of human brain hemispheres: T2 relaxation times during formaldehyde fixation.," *Magn Reson Med*, vol. 61, pp. 810–8, apr 2009.

[186] C. J. Yong-Hing, A. Obenaus, R. Stryker, K. Tong, and G. E. Sarty, "Magnetic resonance imaging and mathematical modeling of progressive formalin fixation of the human brain.," *Magn. Reson. Med.*, vol. 54, pp. 324–32, aug 2005.

[187] T. M. Shepherd, J. J. Flint, P. E. Thelwall, G. J. Stanisz, T. H. Mareci, A. T. Yachnis, and S. J. Blackband, "Postmortem interval alters the water relaxation and diffusion properties of rat nervous tissue–implications for MRI studies of human autopsy samples.," *Neuroimage*, vol. 44, pp. 820–6, feb 2009.

[188] J. A. Kiernan, "Preservation and retrieval of antigens for immunohistochemistry," *Cut. Edge, Natl. Soc. Histotechnol.*, vol. 60, pp. 5–9, 2005.

[189] D. I. Thickman, H. L. Kundel, and G. Wolf, "Nuclear magnetic resonance characteristics of fresh and fixed tissue: the effect of elapsed time.," *Radiology*, vol. 148, pp. 183–5, jul 1983.

[190] K. W. Fishbein, Y. a. Gluzband, M. Kaku, H. Ambia-Sobhan, S. a. Shapses, M. Ya-mauchi, and R. G. Spencer, "Effects of formalin fixation and collagen cross-linking on T2 and magnetization transfer in bovine nasal cartilage.," *Magn. Reson. Med.*, vol. 57, pp. 1000–11, jun 2007.

[191] T. M. Shepherd, P. E. Thelwall, G. J. Stanisz, and S. J. Blackband, "Aldehyde fixative solutions alter the water relaxation and diffusion properties of nervous tissue.," *Magn. Reson. Med.*, vol. 62, pp. 26–34, jul 2009.

[192] P. W. Hales, R. a. B. Burton, C. Bollensdorff, F. Mason, M. Bishop, D. Gavaghan, P. Kohl, and J. E. Schneider, "Progressive changes in T 1, T 2 and left-ventricular histo-architecture in the fixed and embedded rat heart," *NMR Biomed.*, vol. 24, no. 7, pp. 836–843, 2011.

[193] P. Dusek, V. I. Madai, M. Dieringer, F. Hezel, T. Niendorf, J. Sobesky, R. Matej, and J. Wuerfel, "Effect of embedding media on post-mortem MRI of formalin-fixed

brain tissue at 7.0 T," in *Proc. Intl. Soc. Mag. Reson. Med. 22 1418.*, vol. 59, p. 2014, 2014.

[194] P. Medawar, "The rate of penetration of fixatives," *J. R. Microsc. Soc.*, vol. 61, pp. 46–57, 1941.

[195] J. N. CUMINGS, "The copper and iron content of brain and liver in the normal and in hepato-lenticular degeneration.," *Brain*, vol. 71, pp. 410–5, dec 1948.

[196] J. A. E. . Kumar, G. L. & Kiernan, "Fixation in tissue processing," in *Educ. Guid. Spec. Stain. H E*, 2010.

[197] H. Puchtler and S. Meloan, "On the chemistry of formaldehyde fixation and its effects on immunohistochemical reactions," *Histochemistry*, 1985.

[198] Z. Abbas, V. Gras, K. Möllenhoff, F. Keil, A.-M. Oros-Peusquens, and N. J. Shah, "Analysis of proton-density bias corrections based on T1 measurement for robust quantification of water content in the brain at 3 Tesla.," *Magn. Reson. Med.*, vol. 00, jan 2014.

[199] S. Volz, U. Nöth, A. Jurcoane, U. Ziemann, E. Hattingen, and R. Deichmann, "Quantitative proton density mapping: correcting the receiver sensitivity bias via pseudo proton densities.," *Neuroimage*, vol. 63, pp. 540–52, oct 2012.

[200] A. Purea and A. G. Webb, "Reversible and irreversible effects of chemical fixation on the NMR properties of single cells.," *Magn. Reson. Med.*, vol. 56, pp. 927–31, oct 2006.

[201] E.-L. Chen and R. J. Kim, "Magnetic resonance water proton relaxation in protein solutions and tissue: T(1rho) dispersion characterization.," *PLoS One*, vol. 5, p. e8565, jan 2010.

[202] R. M. Lebel and A. H. Wilman, "Transverse relaxometry with stimulated echo compensation.," *Magn. Reson. Med.*, vol. 64, pp. 1005–14, oct 2010.

[203] M. Weigel, "Extended phase graphs: dephasing, RF pulses, and echoes - pure and simple.," *J. Magn. Reson. Imaging*, vol. 41, pp. 266–95, feb 2015.

[204] R. Bakshi, R. H. B. Benedict, R. A. Bermel, S. D. Caruthers, S. R. Puli, C. W. Tjoa, A. J. Fabiano, and L. Jacobs, "T2 hypointensity in the deep gray matter of

patients with multiple sclerosis: a quantitative magnetic resonance imaging study.,” *Arch. Neurol.*, vol. 59, pp. 62–8, jan 2002.

[205] S. D. Brass, R. H. B. Benedict, B. Weinstock-Guttman, F. Munschauer, and R. Bakshi, “Cognitive impairment is associated with subcortical magnetic resonance imaging grey matter T2 hypointensity in multiple sclerosis.,” *Mult. Scler.*, vol. 12, pp. 437–44, aug 2006.

[206] W. Craelius, M. W. Migdal, C. P. Luessenhop, A. Sugar, and I. Mihalakis, “Iron deposits surrounding multiple sclerosis plaques.,” *Arch. Pathol. Lab. Med.*, vol. 106, pp. 397–9, aug 1982.

[207] S. M. LeVine, “Iron deposits in multiple sclerosis and Alzheimer's disease brains.,” *Brain Res.*, vol. 760, pp. 298–303, jun 1997.

[208] C. Lucchinetti, W. Brück, J. Parisi, B. Scheithauer, M. Rodriguez, and H. Lassmann, “Heterogeneity of multiple sclerosis lesions: implications for the pathogenesis of demyelination.,” *Ann. Neurol.*, vol. 47, pp. 707–17, jun 2000.

[209] C. Stüber, M. Morawski, A. Schäfer, C. Labadie, M. Wähnert, C. Leuze, M. Streicher, N. Barapatre, K. Reimann, S. Geyer, D. Spemann, and R. Turner, “Myelin and iron concentration in the human brain: A quantitative study of MRI contrast.,” *Neuroimage*, vol. 93 Pt 1, pp. 95–106, jun 2014.

[210] S.-H. Oh, Y.-B. Kim, Z.-H. Cho, and J. Lee, “Origin of B0 orientation dependent R2(*) (=1/T2(*)) in white matter.,” *Neuroimage*, vol. 73, pp. 71–9, jun 2013.

[211] S. Wharton and R. Bowtell, “Effects of white matter microstructure on phase and susceptibility maps,” *Magn. Reson. Med.*, vol. 00, pp. n/a–n/a, mar 2013.

[212] J. R. Connor, B. S. Snyder, P. Arosio, D. a. Loeffler, and P. LeWitt, “A quantitative analysis of isoferritins in select regions of aged, parkinsonian, and Alzheimer's diseased brains.,” *J. Neurochem.*, vol. 65, no. 2, pp. 717–724, 1995.

[213] A. Deistung, A. Schäfer, F. Schweser, U. Biedermann, R. Turner, and J. R. Reichenbach, “Toward in vivo histology: a comparison of quantitative susceptibility mapping (QSM) with magnitude-, phase-, and R2*-imaging at ultra-high magnetic field strength.,” *Neuroimage*, vol. 65, pp. 299–314, jan 2013.

[214] F. Barkhof and P. Scheltens, "Imaging of white matter lesions.," *Cerebrovasc. Dis.*, vol. 13 Suppl 2, pp. 21–30, jan 2002.

[215] Y. Miki, R. I. Grossman, J. K. Udupa, L. Wei, D. L. Kolson, L. J. Mannon, and M. Grossman, "Isolated U-fiber involvement in MS: preliminary observations.," *Neurology*, vol. 50, pp. 1301–6, may 1998.

# Christoph Birkl

*Curriculum Vitae*

## Private

| | |
|---|---|
| Born: | April $28^{th}$, 1986 in Zams, Tirol, Austria |
| Citizenship: | Austria |
| Privat: | Bischofplatz 1 |
| | 8010 Graz, Austria |
| Mobile: | +43 (0) 664 380 6231 |
| Email: | christoph@birkl.com |
| Office: | Neuroimaging Research Unit |
| | Department of Neurology, Medical University of Graz |
| | Auenbruggerplatz 22, 8036 Graz, Austria |
| Telephone: | +43 (0) 316 385 16438 |
| Web: | www.neuroimaging.at |

## Academia

**2012-2015** **PhD Program in Engineering Science (Dr.techn.)**
GRAZ UNIVERSITY OF TECHNOLOGY, Doctoral School Biomedical Engineering
PhD Thesis: Post-mortem Assessment of Iron in Multiple Sclerosis using Magnetic resonance Imaging

**2010-2012** **Master Program in Biomedical Engineering (Dipl.-Ing.)**
GRAZ UNIVERSITY OF TECHNOLOGY, Specialization Bioimaging and Bioinstrumentation
Master thesis: Verification of Brown Adipose Tissue using MRI

**2006-2010** **Bachelor Program in Biomedical Engineering (BSc)**
GRAZ UNIVERSITY OF TECHNOLOGY, Specialization Health Care Engineering
Bachelor thesis: Analysis of Image Quality Markers at different Computer Tomography Systems

**2000-2005** **Technical High School for Electrical Engineering**
HTL INNSBRUCK ANICHSTRASSE, Specialization Information Technology

## Work Experiences

**2012-today** **Department of Neurology, Medical University of Graz**
Research Assistant at the Neuroimaging Research Unit

**2010** **Graz University of Technology**
Teaching Assistant at the Institute of Medical Engineering

**2010** **Department of Pediatric Radiology, Medical University of Graz**
Research Work: Evidence based development of pediatric CT-protocols balancing dose abd quality

**2010** **AVL List GmbH, Graz**
Internship at the Division Instrumentation and Test Systems

**2009** **Graz University of Technology**
Teaching Assistant at the Institute of Medical Engineering

**2001-2008** **HEITEC AG Regensburg, Germany**
Internship at the Division of Automotion and Image Processing

**2001-2008** **Energie- und Wirtschaftsbetriebe der Gemeinde St. Anton GmbH**
Internship at the Division of Electrical Engineering and IT Systems

## University Committees

**2009-today** **Curricular Committee for Biomedical Engineering**
Member

**2009-2012** **Member of the Student Council for Biomedical Engineering**
2010/2011 Head of the Student Council

## Research Interests

- Magnetic Resonance Imaging (MRI)
- Magnetic properties of biological tissue
- Temperature and fixation effects in post-mortem MRI
- Post-mortem imaging
- MRI of neurodegenerative diseases

## Memberships

**Since 2012** **International Society for Magnetic Resonance in Medicine (ISMRM)**
Trainee Member

**Since 2012** **The European Society for Magnetic Resonance in Medicine and Biology (ESMRMB)**
Student Member

**Since 2012** **Austrian Society for Biomedical Engineering (OEGBMT)**
Member

## Awards

2014 **Best Poster Award**
3rd International Workshop on MRI Phase Contrast & Quantitative Susceptibility Mapping, Duke University, NC, USA

## Publications

### Peer-Reviewed Journal Papers

[3] **Birkl, C**; Langkammer, C; Krenn, H; Goessler, W; Ernst, C; Haybaeck, J; Stollberger, R; Fazekas, F; Ropele, S; Iron mapping using the temperature dependency of the magnetic susceptibility. Magn Reson Med. 2015; 73(3):1282-1288

[2] **Birkl, C**; Langkammer, C; Haybaeck, J; Ernst, C; Stollberger, R; Fazekas, F; Ropele, S; Temperature Dependency of T1 Relaxation Time in Unfixed and Fixed Human Brain Tissue. Biomed Tech (Berl). 2013;

[1] **Birkl, C**; Langkammer, C; Haybaeck, J; Ernst, C; Stollberger, R; Fazekas, F; Ropele, S; Temperature-induced changes of magnetic resonance relaxation times in the human brain: A postmortem study. Magn Reson Med. 2014; 71(4): 1575-1580

### Peer-Reviewed Conference Papers and Proceedings

[10] **Birkl, C**; Carassiti, D; Langkammer, C; Fazekas, F; Schmierer, K; Ropele, S; Iron mapping in post mortem multiple sclerosis brain Proceedings of the 12. Jahrestagung der Österreichischen Gesellschaft für Neurologie. 2015; -12. Jahrestagung der Österreichischen Gesellschaft für Neurologie; MAR 25-27, 2015; Graz, Austria.

[9] **Birkl, C**; Langkammer, C; Golob-Schwarzl, N; Leoni, M; Haybaeck, J; Goessler, W; Fazekas, F; Ropele, S; Effects of formalin fixation on MR relaxation times in the human brain Proceedings of the ISMRM 23rd Annual Meeting. 2015; ISMRM 23rd Annual Meeting; MAY 30 - JUN 5, 2015; Toronto, Canada.

[8] **Birkl, C**; Krenn, H; Langkammer, C; Maderthoner, C; Haybaeck, J; Fazekas, F; Ropele, S Overestimation of iron content in the human postmortem brain Proceedings oft he Workshop; 3rd International Workshop on MRI phase Contrast & Quantitative Susceptibility Mapping; OCT 6-8, 2014; Duke, NC, USA.

[7] **Birkl, C**; Langkammer, C; Haybaeck, J; Ernst, C; Petzold, J; Fazekas, F; Ropele, S; Temperature and fixation correction for postmortem MRI of the brain Proceedings of the ISMRM 22nd Annual Meeting. 2014; ISMRM 22nd Annual Meeting; May 10-16, 2014; Milano, Italy.

[6] Langkammer, C; Krebs, N; **Birkl, C**; Pirpamer, L; Borsodi, F; Haindl, M; Reishofer, G; Porter, DA; Scheurer, E; Fazekas, F; Ropele S; High resolution diffusion MRI of the unfixed post mortem brain. Proceedings; ISMRM 22nd Annual Meeting; May 10-16, 2014; Milano, Italy.

[5] **Birkl, C**; Diwoky, C; Stollberger R; Verification of Brown Adipose Tissue using MRI Abstractbook of the 1st International Student Congress. 2013; 42-43. International Student Congress; Jul 4-6, 2013; Graz, Austria.

[4] **Birkl, C**; Langkammer, C; Haybaeck, J; Ernst, C; Stollberger, R; Fazekas, F; Ropele, S; Temperature induced changes of MRI T1 and T2 relaxation times in the unfixed brain. Proceedings; ISMRM 21st Annual Meeting & Exhibition; Apr 20-26, 2013; Salt Lake City, Utah, USA.

[3] **Birkl, C**; Diwoky, C; Stollberger, R; Nachweis von braunem Fett mittels MR Tagungsband der ÖGBMT Jahrestagung 2012. 2012; Jahrestagung der Österreichische Gesellschaft für Biomedizinische Technik; 20-22. Sept 2012; Hall in Tirol.

[2] **Birkl, C**; Langkammer, C; Haybaeck J; Ernst, C; Stollberger, R; Fazekas, F; Ropele, S; Temperature induced changes of MRI relaxation rates in the brain: An unfixed postmortem study. Book of Abstracts. 2012; 29th Annual Meeting ESMRMB; Oct 4-6, 2012; Lisbon, Portugal.

[1] Sorantin,E; Fotter,R; **Birkl,C**; Digitale Welt und Bildverarbeitung in der Pädiatrischen Radiologie. RoeFo - Fortschritte auf dem Gebiet der Röntgenstrahlen und der bildgebenden Verfahren / Inhaltsverzeichnis. 2011; 183(S01):WS117–92. Deutscher Röntgenkongress und 6. Gemeinsamer Kongress der DRG und ÖRG; Jun 1-4, 2011; Hamburg, Deutschland.

## Invited Presentations

[1] Postmortem MRI of the brain: Biophysical mechanisms of contrast generation. The University of British Columbia, MRI Research Center; May $7^{th}$ 2013